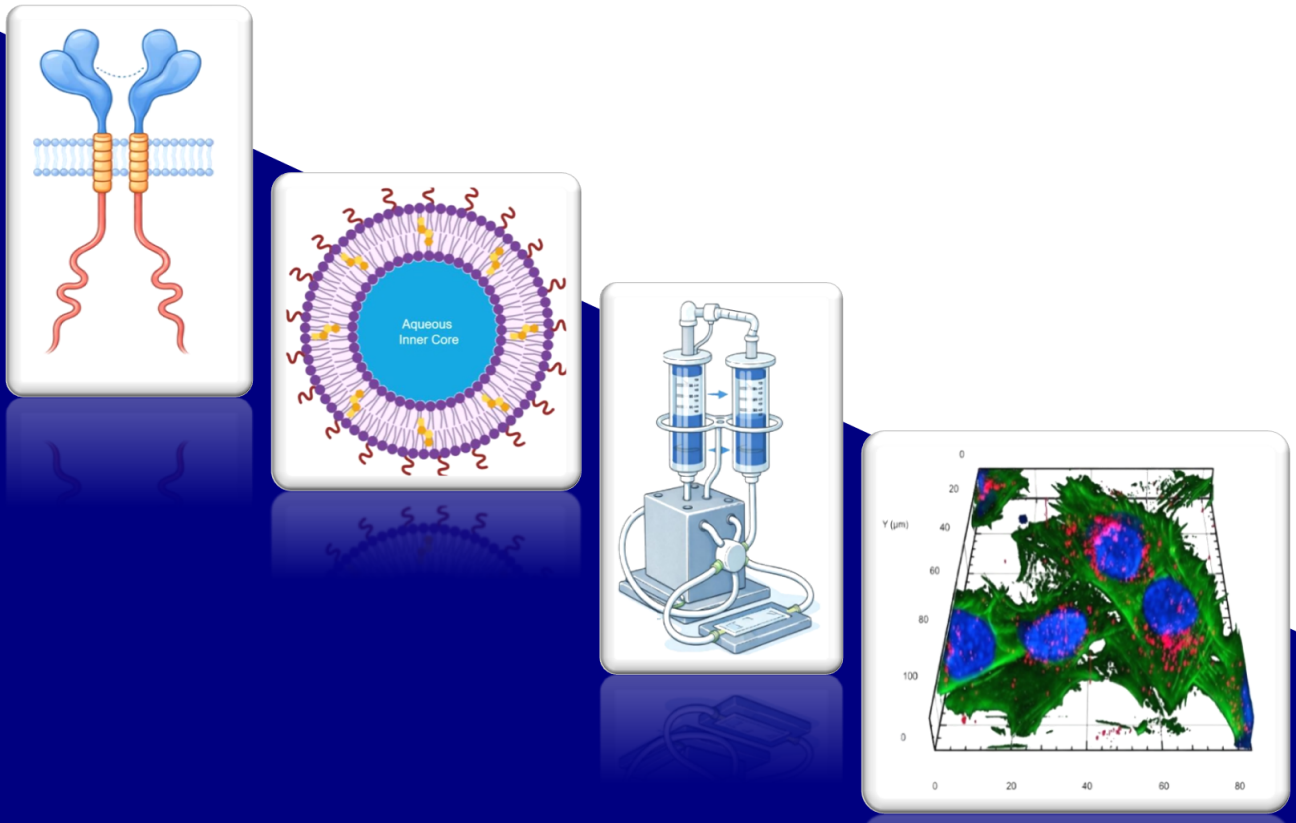
UNIVERSITÀ DEGLI STUDI DI SALERNO

PhD program
in **Drug Discovery and Development**

XXXVIII Cycle – Academic Year 2024/2025

Nanobody-functionalized liposomes for transferrin receptor 1-targeted drug delivery



Melania Scarpa



UNIVERSITÀ DEGLI STUDI DI SALERNO



PhD program
in **Drug Discovery and Development**

Cycle XXXVIII – Academic Year 2024/2025

PhD Thesis

Nanobody-functionalized liposomes for transferrin receptor 1-targeted drug delivery

PhD Candidate
Melania Scarpa

Tutor
Prof. Pietro Campiglia

Co-tutor
Prof.ssa Lucia Baldino

PhD Program Coordinator: Prof.ssa Alessandra Tosco

A voi, che avete camminato con me fino all'alba. A voi dedico la luce di questo nuovo inizio.

Contents

Abstract **1**

1 Introduction **3**

1.1 Targeted drug delivery . . . 3

1.2 The transferrin receptor as a therapeutic target . . . 5

1.3 Liposomes as targeted drug carrier system . . . 6

1.4 Rationale for the development of anti-TfR1 nanobody-functionalized liposomes . . . 7

1.5 Aims and outline of the thesis . . . 8

2 Background and Literature Review **11**

2.1 Transferrin and transferrin receptor 1 . . . 11

2.1.1 Iron regulation and the role of transferrin receptors . . . 11

2.1.2 Transferrin . . . 13

2.1.3 Cellular iron uptake . . . 13

2.1.4 Transferrin receptor 1 . . . 14

2.1.5 Post-transcriptional regulation of TfR1 . . . 16

2.1.6 Expression of TfR1 . . . 17

2.1.7 Expression in healthy tissues . . . 19

2.1.7.1 TfR1 in the brain . . . 19

2.1.7.2 TfR1 in bone marrow and reticulocytes . . . 20

2.1.7.3 TfR1 in the gastrointestinal tract . . . 21

2.1.7.4 TfR1 in other tissues . . . 21

2.1.8 Expression in disease . . . 22

2.1.9 Solid tumors . . . 23

2.1.9.1 Pancreatic cancer . . . 23

2.1.9.2 Brain cancer . . . 24

2.1.9.3 Breast cancer . . . 25

2.1.9.4 Lung cancer . . . 25

2.1.9.5 Colon cancer . . . 26

2.1.9.6 Prostate cancer. . . . 26

2.1.10 Hematological malignancies . . . 28

2.1.10.1 Leukemia 28
2.1.10.2 Lymphoma 28
2.1.11 Other diseases 29
2.1.11.1 Asthma 29
2.1.11.2 Alzheimer 29
2.1.11.3 Depression 30
2.1.11.4 Idiopathic Pulmonary Fibrosis 30
2.1.12 Soluble TfR in health and disease 31
2.1.12.1 Biogenesis and Physiological Role of sTfR 31
2.1.12.2 sTfR in healthy subjects 31
2.1.12.3 sTfR in disease 31
2.1.12.4 sTfR in cancer 32
2.2 Nanoparticle Drug Delivery Systems 33
2.2.1 Lipid-Based Systems 33
2.3 Liposomes 35
2.4 Clinical Applications and Approved Formulations (FDA, EMA) 38
2.5 Liposome Production Methods 39
2.5.1 Conventional methods: thin-film hydration 39
2.5.2 Microfluidic-assisted liposome production 41
2.5.3 Supercritical CO_2-assisted liposome production 41
2.6 Liposome targeting strategies 41
2.6.1 Passive vs Active Targeting 42
2.7 Targeting ligands 43
2.8 Transferrin 44
2.9 Peptides 45
2.10 Antibodies 46
2.11 Nanobodies 47
2.12 Q52c and R2 Nanobodies 48

3 Materials and Methods **51**
3.1 Materials for thin-film hydration liposomes production and nanobody functionalization 51
3.1.1 Lipids 51
3.1.2 Reagents and buffers 51
3.1.3 Solvents 52
3.1.4 Electrophoresis reagents 52

3.1.5 Fluorescent probes . . . 52
3.1.6 Cell culture media and biological reagents . . . 52
3.1.7 Antibodies and nanobodies . . . 53
3.2 Materials for Super Somes liposome production . . . 53
3.2.1 Lipids . . . 53
3.2.2 Solvents . . . 53
3.2.3 Supercritical fluid . . . 53
3.3 Preparation of liposomes by conventional thin-film hydration . . . 54
3.3.1 Preparation of non-targeted liposomes . . . 54
3.3.2 Preparation of Q52c- and R2-conjugated liposomes . . . 55
3.3.3 Nanobody reduction and conjugation to liposomes . . . 56
3.3.4 Purification of nanobody-functionalized liposomes . . . 56
3.4 Physicochemical characterization of thin-film hydration liposomes . . . 57
3.4.1 Dynamic light scattering and Zeta potential analysis . . . 57
3.4.2 Determination of total lipid concentration by inorganic phosphate assay . . . 58
3.5 SDS-PAGE analysis of nanobody-conjugated liposomes . . . 59
3.6 Detection of TfR1 expression levels by flow cytometry . . . 60
3.7 Static cellular uptake study . . . 61
3.8 Dynamic cellular uptake study under perfusion conditions . . . 62
3.9 Preparation and characterization of Super Somes liposomes by supercritical CO_2-assisted technology . . . 66
3.9.1 Supercritical CO_2-assisted production of non-functionalized liposomes . . . 66
3.9.2 Post-insertion PEGylation . . . 67
3.9.3 Dynamic light scattering and Zeta potential analysis . . . 67
3.9.4 Scanning Electron Microscopy (SEM) analysis . . . 68
3.9.5 Stability evaluation over time . . . 68

4 Results **69**
4.1 Characterization of liposomes produced with supercritical CO_2-assisted technology . . . 69
4.2 Characterization of liposomes prepared by the thin-film hydration method . . . 72
4.3 SDS-PAGE analysis of nanobody-conjugated liposomes . . . 74
4.4 Detection of TfR1 expression levels . . . 75

4.5 Static cellular uptake 77
4.6 Cellular uptake of Q52c-liposomes in hCMEC/D3 cells evaluated under dynamic perfusion conditions 79
4.7 Perfusion quantification 81

5 Discussion **83**

6 Conclusions **87**

List of Figures

1.1 Schematic representation of systemic and intracellular drug targeting strategies. Adapted from Bae and Park (2011) and Yameen et al. (2014). 4
1.2 Schematic representation of the TfR1 structure. Adapted from Candelaria et al. (2021). 5
1.3 Different liposome types. Adapted from Fang et al. (2018). 7

2.1 Cellular iron uptake via TfR1/Tf system. Image generated using 2025 Biorender. 14
2.2 Crystallographic structure of TfR1-Tf complex. 16
2.3 High TfR1 expression in healthy tissues. Image generated using 2025 Biorender. 17
2.4 TfR1 protein and mRNA expression in healthy tissues. Figure realized with Prism 10.4. 19
2.5 Schematic representation of major cancer types associated with TfR1 overexpression. Image generated using 2025 Biorender. 23
2.6 Liposomes structure. Image created with Biorender 2025. 35
2.7 Schematic representation of thin film hydration method. Adapted from Lombardo et al., (2022). 40
2.8 Super Somes lab-scale plant. 42

3.1 Main steps of the lipid film hydration method followed by extrusion. . 55
3.2 Main steps of the direct thiol-maleimide conjugation of nanobodies to liposomes. 57
3.3 Gel electrophoresis system (Novex™, Life Technologies) used for protein separation by SDS-PAGE. The image shows the electrophoresis tank containing precast gel cassettes and running buffer, employed for the analysis of protein profiles in the examined samples. 59
3.4 Static cellular uptake performed in 24-well plates. 62
3.5 Schematic of the Ibidi µ-Slide perfusion system is used to expose cells cultured in a slide-like chamber to continuous unidirectional flow generated by a pump system. 63
3.6 Four parallel microfluidic systems used for dynamic uptake experiments under flow conditions, comparing untreated controls with untargeted, Q52c-targeted, and R2-targeted DiD-labeled liposomes. 64
3.7 Zeiss Observer Z1 fluorescence microscope used for image acquisition. 65
3.8 Post-insertion PEGylation of liposomes. 67

4.1 Comparison of liposomes produced with different phosphatidylcholine concentrations. 70
4.2 Size distribution curves of non-PEGylated and PEGylated Super Somes liposomes. 71
4.3 SEM morphology of PEGylated Super Somes liposomes. (1) Representative low-magnification image showing well-dispersed nanosized liposomal structures. (2) Higher-magnification image confirming the predominantly spherical morphology of the vesicles and the absence of evident large aggregates. The morphological observations are consistent with the size distribution obtained by DLS analysis. 72
4.4 Stability over time of PEGylated liposomes during storage at 4 °C. . . 72
4.5 Coomassie-stained SDS-PAGE of Q52c, R2 (pre/post-purification) and untargeted liposomes. 74
4.6 Percentage of TfR1 expressing cells in different cell types. 75
4.7 TfR1 expression levels in different cell types. 76
4.8 Static uptake of liposomes formulations in MCF7, A549 and hCMEC/D3 cells. 77
4.9 Fluorescence microscopy images of Q52c-liposomes in hCMEC/D3 cells compared with control formulations. Green: β-actin; blue: nuclei; red: DiD-labelled Q52c-liposomes. Scale bar: 20. 79
4.10 Magnified view of a single cell. 80
4.11 Widefield, deconvolved, and orthogonal views of fluorescence z-stacks showing the localization of Q52c-liposomes in hCMEC/D3 cells under dynamic flow conditions. (a) Widefield image. (b) Corresponding deconvolved image. (c) Orthogonal projections of the deconvolved z-stack: the central image represents the X–Y view, while the upper and right panels show the corresponding X–Z and Y–Z views, respectively. Green: β-actin; blue: nuclei; red: DiD-labelled Q52c-liposomes. Scale bar: 20. 80
4.12 Three-dimensional reconstruction of deconvolved fluorescence z-stacks showing the localization of Q52c-liposomes in hCMEC/D3 cells under dynamic flow conditions. The reconstructed cellular volume is shown at 0°, 45°, and 90° rotations. Green: β-actin; blue: nuclei; red: DiD-labelled Q52c-liposomes. 81
4.13 Quantification of the total, red-stained area from fluorescence microscopy images. 82
4.14 Cell-normalized quantification of DiD-positive liposome uptake after perfusion. 82

List of Tables

2.1 Comparative overview of TfR1 expression in healthy and tumor cell lines. 27
2.2 Overview of lipid nanoparticles with anti-TfR1 ligands. 34
2.3 TfR1-targeted liposomes for cancer therapy. 36
2.4 TfR1-targeted liposomes for delivery to the brain. 37

3.1 Lipid composition of untargeted liposomes with corresponding percentages and molar ratios. 55
3.2 Lipid composition of targeted liposomes with corresponding percentages and molar ratios. 56
3.3 Instrument settings used for flow cytometry analysis. 60

4.1 Size and PDI of liposomes produced with different phosphatidylcholine concentrations. 70
4.2 Comparison of mean hydrodynamic diameter, PDI, and ζ-potential of Super Somes liposomes before and after PEGylation. 70
4.3 Dynamic light scattering (DLS) characterization of liposome formulations. The Z-average diameter (Z-Ave) and polydispersity index (PDI) are reported for untargeted and targeted liposomes. 73
4.4 Zeta potential values of liposome formulations. Data is reported as mean ± standard deviation for untargeted and targeted liposomes. . . 73
4.5 Quantitative results obtained from flow cytometry. 76
4.6 Quantitative cellular uptake data expressed as mean fluorescence intensity (MFI) following 4 h incubation at 37 °C with untargeted, R2-functionalized, or Q52c-functionalized liposomes. 78
4.7 Fold increase in MFI of Q52c-functionalized liposomes relative to untargeted and R2-functionalized liposomes. 78

Abstract

This thesis “Nanobody-functionalized liposomes for transferrin receptor 1-targeted drug delivery” focuses on the development and validation of a novel targeted liposomal system functionalized with the anti-TfR1 nanobody Q52c. Iron is an essential metal involved in numerous cellular and metabolic processes and must be tightly regulated to prevent the pathological consequences of both deficiency and excess.Transferrin receptor 1 (TfR1; CD71) plays a central role in iron homeostasis by mediating the uptake of transferrin-bound iron. Because TfR1 is frequently overexpressed in highly proliferative and metabolically active cells, including cancer, it represents an attractive and promising target for drug delivery applications.

Building on an extensive review of the literature, this thesis addressed both the therapeutic relevance of TfR1 and the limitations of conventional targeting strategies. The main objective was to investigate the potential of TfR1 as a biological target for nanocarrier-mediated drug delivery. The receptor-specific targeting approach adopted was Q52c, as a novel and previously unexplored ligand for liposome functionalization. Liposomes were selected as nanocarriers because of their biocompatibility, versatility, and ability to interact with biological barriers.The thesis aimed to assess whether Q52c-mediated TfR1 targeting could enhance the selective recognition of TfR1-expressing cells and promote receptor-mediated cellular uptake.

The production and in vitro studies of Q52c-functionalized liposomes were conducted at the Department of Pharmaceutics, Utrecht University. Cellular uptake experiments were performed under both static and dynamic flow conditions, with the latter designed to mimic physiological intravascular shear stress. Static uptake studies were conducted in human cerebral microvascular endothelial cells (hCMEC/D3), human breast cancer cells (MCF-7), and human lung adenocarcinoma cells (A549), allowing liposome uptake to be tested across different TfR1-expressing cellular models and enabling a comparison between tumor and endothelial cell models.

Dynamic perfusion experiments were performed in hCMEC/D3 cells, an established in vitro model of the blood–brain barrier (BBB). Under flow conditions, these cells are exposed to shear stress, providing a more physiologically relevant model for studying the uptake of liposomal nanocarriers. Q52c-functionalized liposomes displayed higher cellular uptake than both R2-functionalized control liposomes and non-targeted liposomes under static and dynamic conditions. These results support the use of Q52c-decorated liposomes as a promising strategy to enhance TfR1-mediated targeting and improve therapeutic precision while reducing off-target effects.

In parallel, non-functionalized liposomes were produced at the Department of Industrial Engineering, University of Salerno, using supercritical CO_2-assisted technology. This activity was not intended as a direct comparison with the nanobody-functionalized formulations developed in Utrecht, but rather as a manufacturing-oriented study aimed at exploring a potentially scalable and reproducible platform for future pharmaceutical translation.

This thesis provides experimental evidence that anti-TfR1 nanobodies can be effectively used to functionalize liposomes and enhance their selective uptake by TfR1-expressing cells. In addition, the preliminary production of non-functionalized liposomes by supercritical CO_2-assisted technology highlights the potential of this approach as a scalable and reproducible manufacturing platform for future liposomal formulations. The integration of receptor-specific nanobody targeting advanced production technologies may contribute to the future translation of TfR1-targeted liposomal systems toward pharmaceutical applications.

1

Introduction

1.1 Targeted drug delivery

Targeted drug delivery aims to enhance the therapeutic efficacy of drug molecules by facilitating their accumulation at the desired site of action while minimizing distribution to healthy tissues. Consequently, targeted delivery can reduce off-target adverse effects and broaden the therapeutic window of the administered drug (Yokoyama, 2005). Targeted drug delivery can be broadly categorized into systemic and intracellular targeting (Figure 1.1). Systemic targeting aims to direct drug carriers toward specific tissues or pathological sites through the bloodstream followed by extravasation. This process may rely on ligand-receptor interactions, in which surface-functionalized carriers recognize specific receptors expressed by target cells, or on locally activated mechanisms. In the latter case, drug release can be triggered either by endogenous stimuli present at the target site, such as specific enzymes or pH variations, or by external stimuli, including light, temperature, magnetic fields, and ultrasound. However, reaching the target tissue is not always sufficient to ensure therapeutic efficacy. In some cases, drug carriers must also be internalized by target cells and release their therapeutic payload within specific intracellular compartments, such as the cytosol, nucleus, or mitochondria. This requirement is particularly critical for advanced therapeutic strategies, including gene therapy and small interfering RNA (siRNA)-based treatments (Bae and Park, 2011).

In 1986, Matsumura and Maeda described the enhanced permeability and retention (EPR) effect, a passive targeting mechanism that enables macromolecules and nanocarriers to preferentially accumulate in solid tumors due to hyperpermeable of tumor vasculature and impaired lymphatic drainage (Matsumura and Maeda, 1986). Conversely, intact endothelial tight junctions of healthy tissues limit macromolecular extravasation, thereby reducing off-target accumulation.

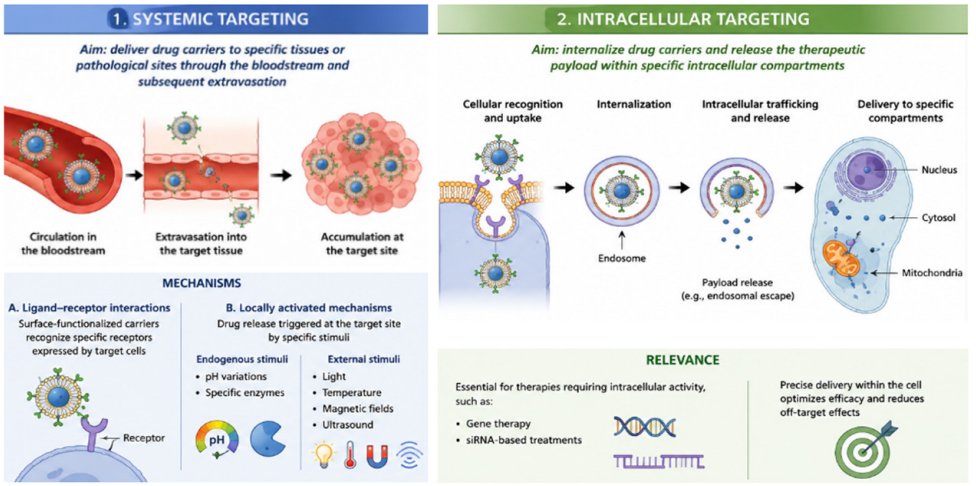


Figure 1.1: Schematic representation of systemic and intracellular drug targeting strategies. Adapted from Bae and Park (2011) and Yameen et al. (2014).

Consequently, the EPR effect has long been considered a cornerstone of passive tumor targeting in nanomedicine. Several nanocarrier formulations have been developed to exploit this phenomenon, notably pegylated liposomal doxorubicin (Doxil®), which received clinical approval for the treatment of Kaposi's sarcoma (Barenholz, 2012). Despite its clinical success, EPR-mediated delivery presents significant limitations. Nanocarrier penetration and distribution within tumor tissue are often hampered by elevated interstitial fluid pressure (IFP) resulting from vascular hyperpermeability and dense extracellular matrix deposition. Furthermore, proliferating tumor cells compress intratumoral lymphatic vessels, which impairs drainage and exacerbates IFP. Tumor heterogeneity also plays a critical role, since poorly vascularized or necrotic regions, often located in the tumor core, show reduced vascular leakage and therefore limited nanocarrier accumulation. These limitations indicate that passive targeting alone cannot ensure efficient drug delivery throughout solid tumors (Kumari et al., 2016).

Active targeting represents an alternative strategy in which in which carrier surfaces are functionalized with affinity ligands designed to bind receptors or epitopes selectively overexpressed on pathological cells, thereby enhancing specificity compared to passive targeting alone (Bertrand et al., 2014). Furthermore, ligand–receptor engagement frequently triggers cellular internalization via receptor-mediated endocytosis (Xu et al., 2013). These ligands encompass monoclonal antibodies, antibody fragments, peptides, nucleic acid aptamers, and small molecules such as vitamins (Yoo et al., 2019).

Among the receptors exploited for active targeting, TfR1 is of particular interest because it is frequently overexpressed in rapidly proliferating cells, including many cancer cells (Daniels et al., 2012).

1.2 The transferrin receptor as a therapeutic target

The transferrin receptor (TfR, CD71), particularly its isoform TfR1 (Figure 1.2), plays a central role in cellular iron homeostasis by mediating iron uptake via binding to iron-loaded transferrin (Tf) (Muckenthaler et al., 2017). Physiologically, TfR1 is highly expressed in proliferating cells and in brain capillary endothelial cells (BCECs) forming the blood–brain barrier (BBB). In pathological contexts, TfR1 is frequently overexpressed, up to 100-fold higher than on non-malignant counterparts, across numerous solid and hematological cancers, as well as in inflammatory and neurodegenerative disorders, making it an attractive therapeutic target (Kukulj et al., 2010; Dufès et al., 2013). This upregulation is mainly related to the increased iron demand required to sustain DNA synthesis, mitochondrial metabolism, and rapid cell proliferation (Shen et al., 2018) and is frequently correlating with disease progression and advanced histological stage (Kondo et al., 1990; Yang et al., 2001). The high expression of TfR1 on BCECs and tumor cells, combined with its ability to undergo ligand-mediated internalization, makes this receptor a highly attractive target for the delivery of therapeutic agents to the brain and tumor tissues. Within this scope, liposomes represent one of the most widely investigated nanocarrier platforms for TfR1-targeted delivery.

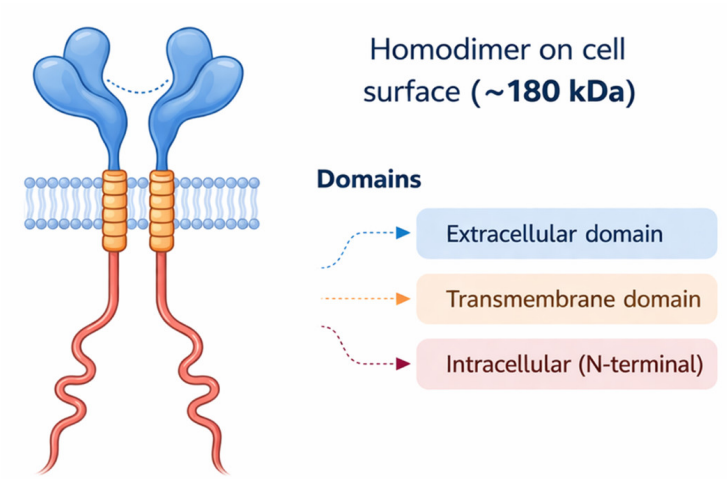


Figure 1.2: Schematic representation of the TfR1 structure. Adapted from Candelaria et al. (2021).

1.3 Liposomes as targeted drug carrier system

Liposomes are nanoscale vesicles composed of one or more phospholipid bilayers enclosing an internal aqueous compartment (Bangham, 1968). Their potential as drug delivery systems was recognized in the early 1970e, when Gregoriadis and co-workers first proposed liposomes as carriers for therapeutic molecules (Gregoriadis, 1973). A defining advantage of liposomes is their structural versality in payload loading: hydrophilic drugs are entrapped within the aqueous core, lipophilic agents are partitioned into the hydrophobic lipid bilayer, and amphiphilic compounds at the bilayer interface. Beyond high biocompatibility, liposomal encapsulation shields payloads from premature enzymatic and chemical degradation in systemic circulation, mitigating off-target toxicity, enabling higher maximum tolerated doses, and thereby improving the overall therapeutic window (Giordani et al., 2023). However, first-generation ("conventional") liposomes exhibited limited in vivo efficacy due to poor colloidal stability in biological fluids and rapid hepatic and splenic clearance. This rapid clearance is mediated by plasma opsonization, followed by phagocytic sequestration via the mononuclear phagocyte system (MPS), historically termed the reticuloendothelial system (RES) (Senior, 1987; Schenkman et al., 1981).

To overcome these pharmacokinetic drawbacks, steric stabilization via surface grafting with hydrophilic polymers, most notably polyethylene glycol (PEG), was implemented. These "stealth" or PEGylated liposomes exhibit reduced protein corona formation, minimized MPS clearance, and significantly extended blood circulation half-lives (Immordino et al., 2006). To further improve target selectivity and promote uptake, liposomal surfaces can be decorated with specific active targeting ligands. This functionalization facilitates ligand-directed binding and subsequent receptor-mediated endocytosis, playing a key role in the development of advanced liposomal drug delivery systems. These formulations are generally referred to as targeted liposomes, or immunoliposomes when antibodies or antibody fragments are used as targeting ligands.

Initially, targeting moieties were directly conjugated to the phospholipid bilayer. However, after the development of stealth liposomes, ligands have often been coupled to the distal ends of PEG chains, improving their accessibility for receptor binding. Moreover, different ligands can be combined on the same carrier to increase targeting specificity and address tumor heterogeneity (Amin et al., 2022). Nevertheless, active targeting requires careful optimization, since ligand density, binding affinity, steric hindrance, receptor expression, and intracellular trafficking can strongly influence the final delivery efficiency (Muro, 2012). The active targeting strategy with liposomes is adequately reviewed in the literature (Mastrobattista et al., 1999; Sapra and Allen, 2005; Belfiore et al., 2018; Abbasi et al., 2022). Different types of liposomes are shown in Figure 1.3.

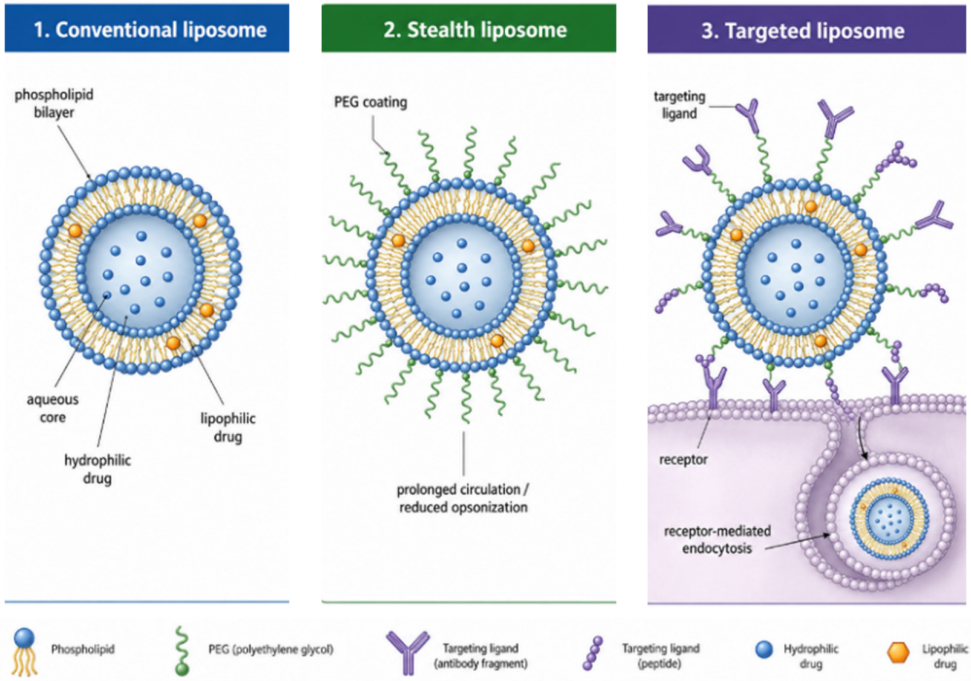


Figure 1.3: Different liposome types. Adapted from Fang et al. (2018).

1.4 Rationale for the development of anti-TfR1 nanobody-functionalized liposomes

In this thesis, liposomes were selected as the delivery platform because of their biocompatibility, formulation versatility, and suitability for surface modification. TfR1 was selected as the biological target because of its increased expression in several pathological conditions and highly proliferative cellular contexts. The combination of these two elements provides the basis for the development of TfR1-targeted liposomal systems.

Instead of using Tf itself as a targeting ligand, this project focuses on the use of anti-TfR1 nanobodies. Tf-based targeting may be limited by competition with endogenous Tf, which can interfere with receptor binding and reduce targeting efficiency. In contrast, anti-TfR1 nanobodies can be selected to recognize specific receptor epitopes, potentially avoiding competition with physiological Tf. Compared with larger targeting ligands, such as full-length antibodies, nanobodies are characterized by small size, high stability, good tissue penetration, and easier engineering. Therefore, anti-TfR1 nanobody-functionalized liposomes may combine the advantages of liposomal drug delivery with the specificity of receptor-mediated targeting, potentially improving selective binding, cellular uptake, and intracellular delivery in TfR1-expressing cells.

1.5 Aims and outline of the thesis

The main aim of this PhD thesis was to produce and evaluate TfR1-targeted liposomes functionalized with the anti-TfR1 nanobody Q52c, to investigate whether TfR1 represents a suitable target for drug delivery. For this purpose, liposomes were prepared by conventional thin-film hydration, which was selected as the main formulation method because of its suitability for small-batch laboratory production, nanobody functionalization, and cost-effective preparation.

Although the literature supports TfR1 as a promising target due to its role in receptor-mediated internalization and its expression in several physiologically and pathologically relevant tissues, a systematic evaluation of receptor expression across different cellular models and their relationship with liposome uptake remains limited. Therefore, TfR1 expression was first analyzed in different cell types by flow cytometry. This step provided a rational basis for selecting the cellular models used in the uptake studies and allowed the relationship between receptor abundance and the cellular accumulation of Q52c-functionalized liposomes to be investigated.

The novelty of this thesis lies in several aspects. First, the cellular uptake of the developed formulations was investigated not only under conventional static conditions, but also under dynamic flow using an Ibidi-based perfusion system.

This represents an innovative aspect of the study, as controlled flow allowed the formulations to be tested in a more physiologically relevant setting, mimicking the vascular shear stress experienced by circulating liposomes in vivo. Second, this is the first study reporting the functionalization of liposomes with the anti-TfR1 nanobody Q52c. Although TfR1-targeted liposomes have been previously explored using transferrin, peptides, antibodies, or antibody fragments, no data is currently available in the literature on Q52c-functionalized liposomes for TfR1-mediated targeting. Therefore, this work introduces Q52c as a novel targeting ligand for the development of TfR1-directed liposomal nanocarriers.

In parallel with the preparation of TfR1-targeted liposomes by thin-film hydration, supercritical CO_2-assisted production was explored as an additional manufacturing-oriented approach. This activity was performed on non-functionalized Super Somes liposomes and was not intended as a direct comparison with the nanobody-functionalized formulations. Rather, it was included as a preliminary study to investigate the potential of supercritical CO_2-assisted technology as a scalable and reproducible platform to produce liposomes intended for future clinical translation. This technique may offer relevant advantages for pharmaceutical manufacturing, including improved process control, scalability, and reduction of organic solvent residues.

However, due to economic constraints and the limited availability of nanobodies, Super Somes liposomes were not further functionalized with Q52c or R2 and were therefore not used for cellular uptake studies. Both thin-film hydration and supercritical CO_2-assisted production will be further discussed in Chapter 2, within the section dedicated to liposomes.

The thesis is organized as follows. Chapter 2 provides the background and literature review, which is divided into three main sections: the first focuses on TfR1, with particular attention to its biology and potential role as a therapeutic target; the second focuses on liposomes as drug delivery systems for TfR1-targeted delivery; and the third reviews the principal targeting ligands, including transferrin, peptides, antibodies, and nanobodies, used to functionalize liposomes for receptor-mediated drug delivery. Chapter 3 describes the materials and methods used for liposome preparation by thin-film hydration, nanobody conjugation, physicochemical characterization, sodium dodecyl sulfate–polyacrylamide gel electrophoresis (SDS-PAGE) analysis, TfR1 expression analysis, and cellular uptake studies under static and dynamic perfusion conditions. This chapter also includes the preparation and characterization of non-functionalized liposomes obtained by supercritical CO_2-assisted technology. Chapter 4 presents the experimental results obtained in this work. Finally, Chapter 5 discusses the main findings, the limitations of the study, and future perspectives for the development of Q52c-functionalized liposomes as TfR1-targeted drug delivery systems.

2

Background and Literature Review

This chapter provides the scientific background and literature review sustaining the present thesis. It begins with a comprehensive overview of Tf and TfR1, covering their structure, the mechanism of cellular iron uptake, post-transcriptional regulation, and expression profiles in both healthy and diseased tissues, with particular emphasis on TfR1 overexpression in solid tumors and hematological malignancies. Subsequently, nanoparticle drug delivery systems are introduced, focusing on lipid-based carriers and, more specifically, on liposomes: their classification, clinically approved formulations, and the main production methods, including thin-film hydration, microfluidic-assisted techniques, and supercritical CO_2-assisted technology. The chapter then discusses liposome targeting strategies, distinguishing between passive and active approaches, and reviews the principal classes of targeting ligands; Tf, peptides, antibodies, and nanobodies, that have been employed to functionalize liposomes for TfR1-directed drug delivery. Together, these sections establish the rationale for the development of anti-TfR1 nanobody-functionalized liposomes investigated in this work.

2.1 Transferrin and transferrin receptor 1

2.1.1 Iron regulation and the role of transferrin receptors

Iron is a metal present in all life on earth and is indispensable for cellular and metabolic processes. It serves as a critical cofactor for numerous proteins involved in DNA synthesis, the maintenance of nucleic acid integrity, xenobiotic metabolism, and cellular respiration (Muckenthaler et al., 2017; Winn et al., 2020). Furthermore, iron regulates cell fate by influencing growth, proliferation, and apoptosis, while also contributing to host defense and intracellular signaling (Sukhbaatar and Weichhart, 2018; Dev and Babitt, 2017).

Beyond these important functions, iron is essential for oxygen transport, primarily due to its incorporation into hemoglobin (Hb) in erythrocytes, ensuring efficient oxygen delivery to tissues (Vogt et al., 2021; Tortorella and Karagiannis, 2014).
Given its critical nature, it requires tight regulation to prevent the pathological consequences of both deficiency and excess. The transferrin receptor (TfR) plays a crucial role in iron homeostasis, facilitating its uptake through binding with transferrin (Tf) (Kukulj et al., 2010). Tf is primarily synthesized in the liver, with lower levels of expression in extrahepatic tissues such as the brain and testis, reflecting tissue-specific regulation and iron requirements (Zakin et al., 1992). There are two different isoforms of TfR: TfR1 and transferrin receptor 2 (TfR2) (gene names Tfrc and Tfr2). Additionally, TfR1 exists in a soluble form (sTfR). This authoritative review focuses specifically on TfR1 given its central role in iron metabolism and widespread expression across human tissues, making it a promising therapeutic target. TfR1 is widely expressed across multiple cell types; however, its expression levels vary considerably depending on cellular iron requirements. Cells with elevated iron demand, such as reticulocytes, intestinal epithelial cells, placental syncytiotrophoblasts, and neoplastic cells exhibit the highest levels of TfR1 expression (Gkouvatsos et al., 2012) Notably, TfR1 is (over)expressed in many tumors, reflecting the increased iron demand associated with rapid cellular proliferation (Shen et al., 2018). This differential expression pattern, together with its marked upregulation in cancer cells compared to most normal tissues, highlights TfR1 as a particularly attractive target for selective drug delivery strategies. In this context, nanoparticles (NPs), particularly lipid-based nanoparticles such as liposomes and lipid nanoparticles (LNPs), have emerged as versatile tools for targeted drug delivery. By functionalizing their surface with molecules that specifically target TfR1, such as antibodies (Abs), nanobodies (Nbs), and peptides, it is possible to design smart nanocarriers capable of selectively recognizing and binding to TfRs (over)expressed on target cells, thereby increasing the specificity and efficiency of the treatment. Finally, this authoritative review addresses an important gap in the literature by providing a comprehensive and comparative analysis of TfR1 expression in health and disease, with the aim of enhancing therapeutic precision, minimizing side effects, and validating it as a viable target for drug delivery.

2.1.2 Transferrin

Transferrin (Tf) is an ∼80 kDa glycoprotein primarily synthesized in the liver, but its expression and secretion are also observed in other cell types, including Sertoli cells, oligodendroglia cells, endothelial cells of brain capillaries, macrophages, lymphocytes, and fibroblasts (Huebers and Finch, 1987; de Jong et al., 1990; Strickland et al., 2024. In plasma of healthy individuals, Tf is typically present at concentrations of approximately 2.5 g/L (equivalent to ∼31–38 µM), with an iron saturation level of around 30% and a half-life of roughly 8 days. Structurally, Tf consists of two homologous lobes located at its N- and C-terminal domains (MacGillivray et al., 1983; Gomme et al., 2005).

Each lobe can bind one ferric ion (Fe3+), enabling a single Tf molecule to carry up to two iron atoms (Messori and Kratz, 1994). Depending on its iron-loading status, Tf exists in four distinct forms in the circulation: iron-free (apo-Tf, ∼40%), monoferric N-lobe bound (FeNTf, ∼23%), monoferric C-lobe bound (FeCTf, ∼11%), and diferric (Fe2Tf, ∼27%). Specifically, the diferric form (holo-Tf), with both binding sites occupied by Fe3+, exhibits a strong affinity for TfRs present on the cell surface, ensuring efficient iron delivery. In contrast, the iron-free form (apo-Tf) shows markedly reduced receptor binding (Dautry-Varsat, 1986; Gabold et al., 2023). This high-affinity interaction between diferric Tf and TfR triggers receptor-mediated endocytosis, allowing the Tf-TfR1 complex to be internalized into endosomes. The binding of iron to Tf is highly pH dependent. At physiological pH (∼7.4), Tf binds Fe3+ tightly; however, under the acidic conditions of the late endosome (pH ∼ 5.5–6.0), Fe3+ dissociates from Tf (Princiotto and Zapolski, 1976; Steere et al., 2012).

2.1.3 Cellular iron uptake

Iron enters peripheral tissue cells through the binding of Tf to its receptor, TfR1, on the plasma membrane. This interaction triggers receptor-mediated endocytosis, allowing the holo-Tf to be internalized within endosomes. Inside these compartments, the acidic environment of more mature endosomes facilitates the release of ferric iron (Fe3+) from Tf. The proteins of the STEAP family (Six-Transmembrane Epithelial Antigen of Prostate) act as ferrireductases, enzymatically converting Fe3+ into ferrous iron (Fe2+). Once reduced, Fe2+ is transported into the cytosol via the divalent metal transporter 1 (DMT1), where it integrates into the metabolically active cytoplasmic labile iron pool (Figure 2.1). After iron release, apo-Tf (iron-free Tf) remains associated with TfR1 within the endosomal compartment and the complex is subsequently sorted into recycling pathways that return the receptor to the plasma membrane. This rapid recycling process enables TfR1 to undergo multiple cycles of iron uptake and contributes to efficient cellular iron homeostasis (Sheff et al., 2002; Mayle et al., 2012).

This tightly regulated iron transport mechanism ensures efficient cellular iron uptake while preventing toxicity associated with excess intracellular iron (Cheng et al., 2004; Lawrence et al., 1999; Torti and Torti, 2013). Moreover, the rapid recycling and high turnover of TfR1 make this receptor particularly attractive for receptor-mediated drug delivery strategies, as nanoparticles bound to TfR1 can be efficiently internalized and repeatedly transported across the cell membrane.

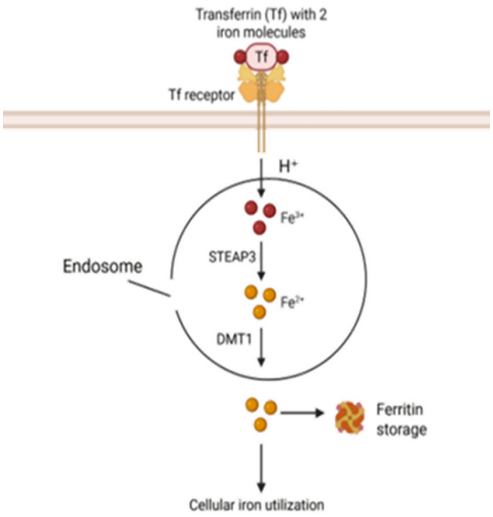


Figure 2.1: Cellular iron uptake via TfR1/Tf system. Image generated using 2025 Biorender.

The cellular iron uptake mechanism mediated by Tf and its receptor. Tf binds two Fe3+ ions and interacts with the TfR1 at the cell surface. The complex is internalized via endocytosis, forming an endosome. Acidification of the endosome triggers iron release, and the Fe3+ is reduced to Fe2+ by the enzyme STEAP3.
Reduced iron is transported into the cytoplasm through DMT1, where it can be utilized or stored in ferritin. The Tf–TfR1 complex is then recycled back to plasma membrane.

2.1.4 Transferrin receptor 1

TfR1, commonly referred to as CD71 (Figure 2.2), is important for cellular iron uptake and plays a key role in systemic iron homeostasis. It is a type II transmembrane glycoprotein with a molecular weight of approximately 90 kDa, forming a disulfide-linked 180 kDa dimer on the cell surface (Li et al., 2023). Each 760-amino acid monomer consists of three domains: a large C-terminal extracellular domain (671 amino acids) responsible for Tf binding, a transmembrane domain (28 amino acids) and an intracellular N-terminal domain (61 amino acids). The extracellular domain contains multiple N-linked and O-linked glycosylation sites, essential for proper receptor folding and stability.

A key functional feature is its strong affinity for holo-Tf, which is crucial for efficient iron delivery. This high binding affinity suggests that it is primarily involved in high-capacity cellular iron uptake. TfR1 expression is post-transcriptionally regulated by intracellular iron levels through the iron regulatory protein–iron responsive element (IRP–IRE) system. Iron deficiency triggers an increase in its expression to enhance iron acquisition whereas iron overload suppresses its synthesis to prevent toxicity. This adaptive mechanism ensures that cells maintain iron balance, minimizing both deficiency and toxicity risks. In fact, studies on HepG2 cells, and other cell models have demonstrated that TfR1 expression is downregulated in a dose-dependent manner following iron exposure, confirming this regulatory pattern (Hubert et al., 1993).
It is present at low levels in most cell types (Kawabata, 2019; Shen et al., 2018) but is highly expressed in cells with elevated iron requirements, such as rapidly proliferating cells, immature erythroid cells, and placental tissue. Interestingly, several non-proliferating cells, including reticulocytes, hepatocytes, and endothelial cells of the BBB, also display high levels (Testi et al., 2019). The essential function of this receptor is further highlighted by the severe consequences of its deficiency, which leads to marked disturbances in iron homeostasis and compromises key biological processes. In homozygous Tfrc knockout mice ($Tfrc^{-/-}$), iron deficiency is observed in both hematopoietic and non-hematopoietic tissues, demonstrating its fundamental role in systemic iron regulation (Levy et al., 1999). The knockout of the Tfrc gene results in embryonic lethality, primarily due to defects in erythropoiesis and neurological abnormalities. Additionally, muscle-specific TfR1 deficiency causes iron depletion not only in muscle tissue but also in adipose tissue and the liver, reinforcing its systemic impact (Barrientos et al., 2015). Moreover, its inactivation in the intestinal epithelium triggers pleiotropic alterations, including loss of epithelial proliferation, disruption of homeostasis, and activation of genes involved in the epithelial-mesenchymal transition, effects that are not directly related to iron uptake but still underscore the broad physiological significance of this receptor (Kawabata, 2019). It plays a pivotal role in erythropoiesis, the process responsible for consuming most of the body's iron supply. Mice with pathologically reduced erythroid TfR1 expression develop microcytic anemia. Homozygous Tfrc knockout mice (Tfrc–/–) experience early embryonic lethality due to defective erythroid and neuronal development. Furthermore, cell-specific inactivation of TfR1 in dopaminergic neurons, lymphocytes, enterocytes, skeletal muscle cells, and cardiomyocytes results in severe pathological outcomes (Fillebeen et al., 2019). Together, these findings demonstrate that this receptor is indispensable for maintaining iron balance, supporting cellular metabolism, and ensuring normal development and tissue integrity.

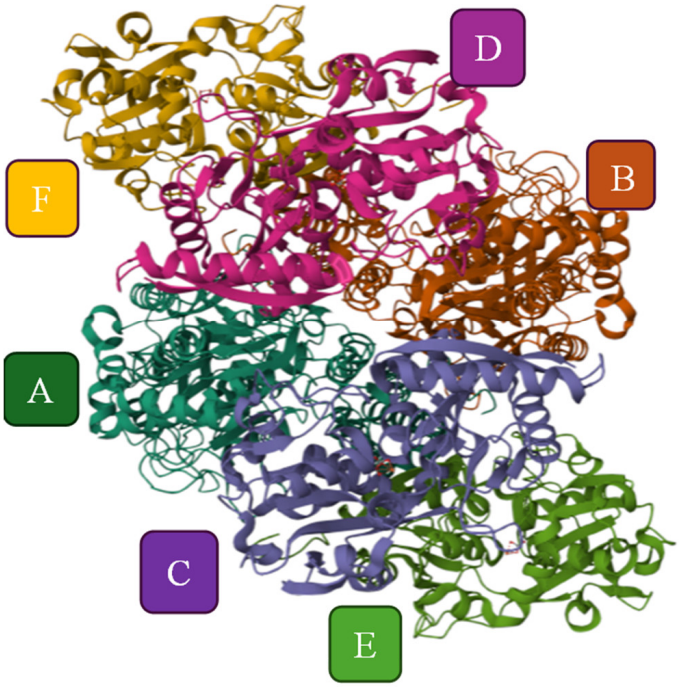


Figure 2.2: Crystallographic structure of TfR1-Tf complex. Figure obtained and adapted from the RCSB Protein Data Bank (RCSB PDB) (https://doi.org/10.2210/pdb1SUV/pdb)

This structure was obtained by fitting the crystal structures of holo-Tf and the extracellular domain of the TfR1. Chains A and B represent the TfR1 dimer. Two Tf molecules are bound to this receptor: the first, composed of chains C and E, corresponds to the N- and C-terminal lobes of one Tf molecule; the second, composed of chains D and F, represents the two lobes of the second Tf. The N-terminal lobe of Tf is positioned between the cell membrane and the extracellular domain of TfR1, while the C-terminal lobe interacts with the receptor's helical domain. Upon binding to the receptor, the N-lobe undergoes a conformational shift of approximately 9 Å relative to the C-lobe.

2.1.5 Post-transcriptional regulation of TfR1

The expression of TfR1 is not constant but is finely tuned in response to intracellular iron levels. Its production increases under iron deficiency to enhance uptake and decreases when iron is abundant to limit intake. This regulation occurs at both the transcriptional and, more critically for TfR1, post-transcriptional levels (Robb and Wessling-Resnick, 2004). The IRP-IRE system plays a key role in post-transcriptional iron regulation. Specifically, IRP1 and IRP2 function as intracellular iron sensors that bind to hairpin-shaped iron-responsive elements (IREs) on mRNA molecules.

Tfrc mRNA contains IREs in its 3' untranslated region (3' UTR). During iron deficiency, IRPs remain active and bind to the IREs in the 3' UTR of Tfrc mRNA, stabilizing the transcript and preventing rapid degradation by nucleases. As a result, Tfrc mRNA remains available for translation, increasing receptor synthesis and enhancing iron uptake from circulating Tf. At the same time, active IRPs bind to IREs in the 5' UTR of ferritin mRNA, blocking its translation and thereby preventing ferritin synthesis, thus limiting iron storage. During iron excess, IRPs become inactive, either by binding iron directly or through oxidative modifications, and lose their ability to bind IREs. Without IRP binding, Tfrc mRNA in the 3' UTR becomes unstable and undergoes rapid degradation by nucleases (Crichton, 2001; Eisenstein, 2000; Aisen et al., 2001; Ru et al., 2024; Galy et al., 2024), reducing receptor synthesis and limiting iron uptake. Conversely, in ferritin mRNA, the absence of IRP binding at the 5' UTR allows translation to proceed, leading to increased ferritin synthesis, ensuring excess iron is stored in a non-toxic form. Through this finely tuned mechanism, the IRP-IRE system ensures a precise balance between iron absorption (via TfR1) and iron storage (via ferritin), adjusting iron availability according to cellular needs and maintaining iron homeostasis.

2.1.6 Expression of TfR1

In this overview, the distribution of TfR1 in healthy tissues will be examined, emphasizing the differences in expression levels. Its expression varies among tissues, adapting to specific metabolic requirements and cellular iron demand (Figure 2.3).

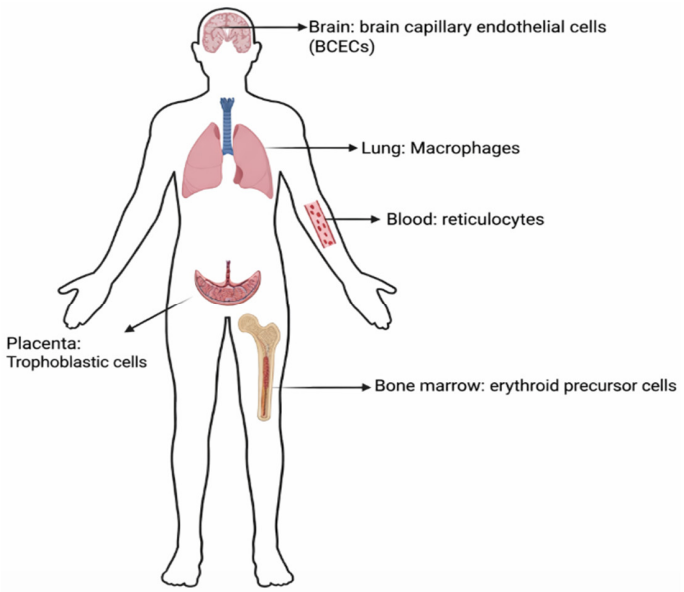


Figure 2.3: High TfR1 expression in healthy tissues. Image generated using 2025 Biorender.

This image (Figure 2.3) highlights the tissue-specific expression of TfR1 in healthy organs characterized by high iron demand. Elevated TfR1 expression is observed in the brain, particularly in brain capillary endothelial cells (BCECs), as well as in alveolar macrophages in the lung, reticulocytes in the blood, erythroid precursor cells in the bone marrow and in trophoblastic cells of the placenta. These cell populations are characterized by intense metabolic activity, active iron recycling, or a key role in maternal-fetal iron transfer, highlighting the essential function of TfR1 in maintaining iron homeostasis and supporting cellular proliferation.

As shown in Figure 2.4, TfRc mRNA is expressed in several tissues where the corresponding protein is either barely detectable or absent. For instance, the pancreas, liver, endometrium, and gallbladder exhibit measurable mRNA levels but show very low or undetectable protein expression. Similarly, the prostate, breast, and kidney display moderate mRNA levels despite minimal protein detection. This divergence between transcript and protein levels highlights the post-transcriptional control of TfR1, mediated by the IRP/IRE regulatory system, which modulates mRNA stability and translation efficiency according to intracellular iron availability. When iron is abundant, IRPs lose their binding affinity for IREs, resulting in mRNA degradation or translational inhibition and, consequently, low protein levels despite high mRNA expression. Conversely, under iron-depleted conditions, IRPs bind to IREs, stabilizing Tfrc mRNA and promoting protein synthesis.

This regulatory mechanism maintains tissue-specific iron homeostasis and explains the lack of a direct correlation between transcript and protein expression observed in Figure 2.4.

The graph illustrates the mRNA expression levels of the Tfrc gene, encoding TfR1, across 55 healthy human tissues. Transcriptomic data, expressed as nTPM (normalized transcripts per million), are derived from the Consensus dataset of the Human Protein Atlas. On the x-axis, mRNA expression values are shown, while the y-axis lists the tissues analyzed.

Protein expression was assessed by immunohistochemistry and is presented using a qualitative scale (high, medium, low, not detected, or not available). TfR1 protein levels are represented by a color code: red = high, orange = medium, yellow = low, green = not detected, grey = not available (N/A). This integrated visualization allows direct comparison of transcriptomic (mRNA) and proteomic (protein) data, providing a comprehensive overview of TfR1 expression across healthy human tissues under physiological conditions.

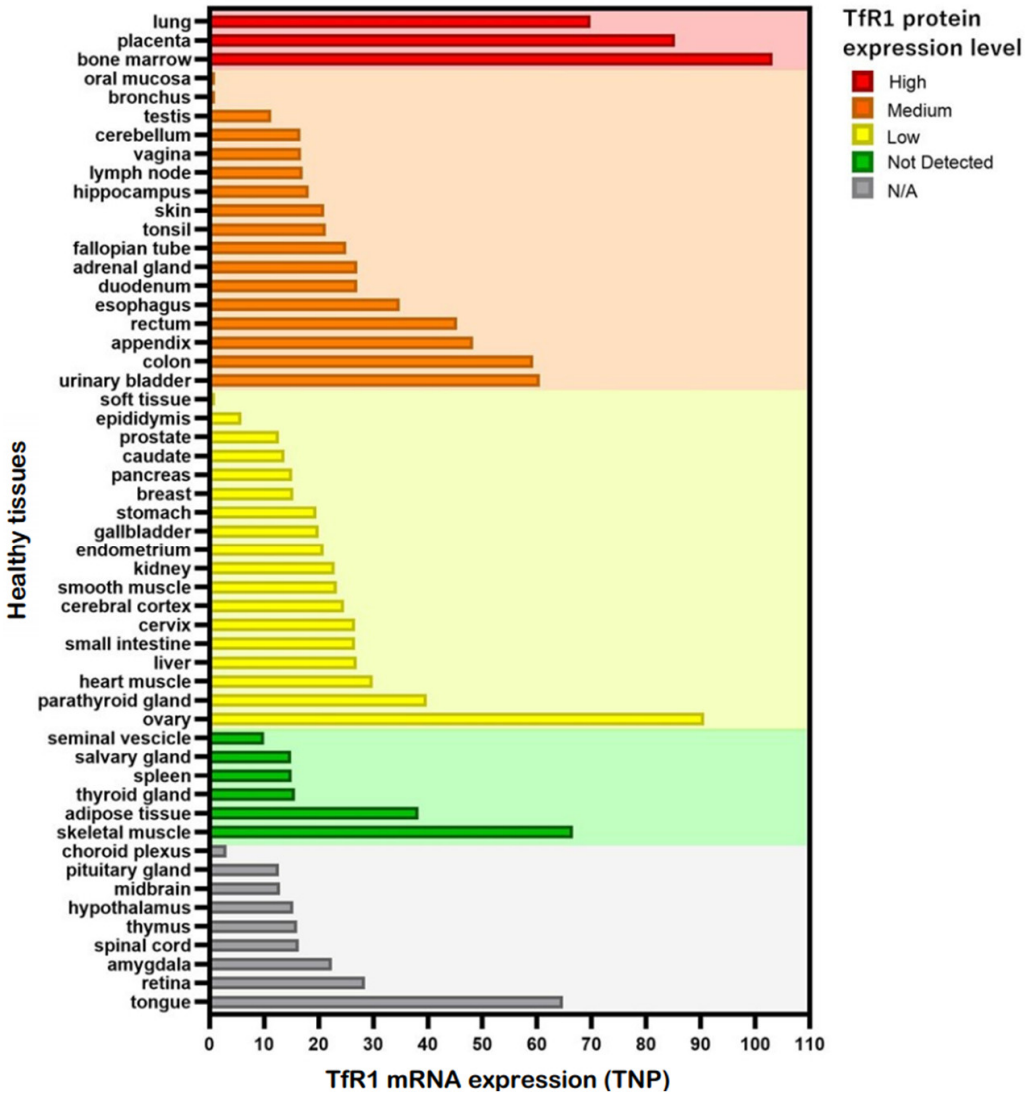


Figure 2.4: TfR1 protein and mRNA expression in healthy tissues. Figure realized with Prism 10.4.

2.1.7 Expression in healthy tissues

2.1.7.1 TfR1 in the brain

TfR1 plays an essential role in iron transport across the BBB, ensuring a continuous supply of iron to the brain. It is highly expressed on brain capillary endothelial cells (BCECs) (Faresjö et al., 2022), where its expression is reported to be at least 100 times greater than in most other tissues (Mojarad-Jabali et al., 2022). This elevated expression reflects the brain's constant demand for iron, which is essential for neuronal function and metabolic processes.

TfR1 distribution extends beyond BCECs, as it is also found in the choroid plexus epithelium and in neurons, where its expression persists throughout life (Moos et al., 2022). This suggests that it is not only involved in iron uptake but also plays a central role in maintaining iron homeostasis within the central nervous system (CNS). Interestingly, the levels of TfR1 protein in BCECs vary across species, with concentrations of 5.2 pmol/mg protein in mice, 7.8 pmol/mg in rats, and 2.3 pmol/mg in humans (Pardridge, 2020). These differences indicate species-specific adaptations in iron transport mechanisms and metabolic demands. In bovine brain capillary endothelial cells (BBCECs), TfR1 is present in high density, with an estimated 35,000 receptors per cell (Table 2.1). The dissociation constant (Kd) of 11.3 ± 2.1 nM further confirms the strong interaction between TfR1 and Tf, reinforcing its essential role in iron uptake. Importantly, however, high receptor expression and binding affinity do not necessarily translate into efficient drug delivery across the BBB. As highlighted by Pardridge (2020), brain-to-plasma ratios for antibodies are extremely low (∼0.01%), and measured brain concentrations may largely reflect retention within the vascular or endothelial compartment rather than true parenchymal distribution. Moreover, cerebrospinal fluid (CSF) levels (∼0.1–0.2% of plasma) can substantially overestimate brain penetration and should not be used as a surrogate for delivery across the BBB. These observations underscore the importance of distinguishing between endothelial uptake, transcytosis, and effective parenchymal accumulation when evaluating TfR1-targeted strategies.

2.1.7.2 TfR1 in bone marrow and reticulocytes

TfR1 is expressed on the surface of most nucleated cells in the body, except for mature erythrocytes, which lose the receptor during terminal differentiation. In the bone marrow, its expression is particularly high in erythroid precursors cells, reflecting their substantial iron requirement for hemoglobin synthesis (Berthou et al., 2021). During erythroid maturation, TfR1 levels progressively increase, reaching approximately 300,000 receptors per cell in early normoblasts and peaking at about 800,000 receptors per cell in intermediate normoblasts (Iacopetta et al., 1982). As differentiation proceeds, receptor expression gradually declines, dropping to around 100,000 receptors in reticulocytes and eventually disappearing in fully mature erythrocytes (Table 2.1) (van Bockxmeer and Morgan, 1979). In erythroid cells, particularly in reticulocytes, the regulation of TfR1 expression depends primarily on intracellular iron demand for hemoglobin synthesis rather than on systemic iron levels. An in vivo study in rats, (R'zik et al., 2001) quantified approximately 50,000 receptors per cell in young rats and about 100,000 in adults, observing that these values remained essentially unchanged under various physiological and experimental conditions, including iron supplementation and iron overload.

These findings indicate that systemic iron excess does not reduce receptor density in reticulocytes, most likely because iron accumulation occurs predominantly in non-erythroid compartments such as hepatocytes and cells of the reticuloendothelial system. Conversely, under conditions of functional iron deficiency, the same authors reported a marked increase in TfR1 expression in reticulocytes.

2.1.7.3 TfR1 in the gastrointestinal tract

Several studies have investigated the distribution of TfR1 in healthy gastrointestinal tissues. Immunohistochemical analyses of healthy individuals demonstrated that it is physiologically expressed in the duodenal epithelium. In normal mucosa, villus epithelial cells showed TfR1 staining predominantly along the basolateral and subnuclear regions, consistent with their role in iron uptake. Additionally, cells within the duodenal crypts exhibited strong TfR1 immunoreactivity, reflecting the high iron demand of proliferating epithelial cells (Lombard et al., 1990). This confirms that this receptor is actively expressed in healthy gastrointestinal tissue and contributes to basal iron homeostasis under physiological conditions. Early histological investigations on biopsies from different regions of the gastrointestinal tract demonstrated that it is expressed in the mucosa of the small and large intestine, particularly in the duodenum, ileum, and colon. Immunohistochemical analyses revealed that the receptor is predominantly localized on the basolateral membrane of villous epithelial cells as well as within the crypts, suggesting a key role in iron absorption and epithelial turnover (Banerjee et al., 1986).

2.1.7.4 TfR1 in other tissues

In the pancreas, TfR1 is absent in healthy exocrine tissue but is detectable within the endocrine compartment. (Ryschich et al., 2004) reported no measurable expression in normal pancreatic tissue, which is predominantly exocrine, while (Gatter et al., 1983) described its selective localization in the endocrine portion of the gland, particularly within the islets of Langerhans. This compartmentalized distribution suggests a specialized role of TfR1 in regulating iron uptake and homeostasis within pancreatic endocrine cells. In the liver, its basal expression is physiologically low and further decreases under iron overload conditions (Herbison et al., 2009). Placental tissue also exhibits dynamic regulation of TfR1 expression. Moreover, its concentrations in placentas demonstrated an inverse correlation with non-heme iron content (Bergamaschi et al., 1990). Complementary findings by Bierings et al. localized TfR1 to the apical membrane of the syncytiotrophoblasts, identifying it as a key mediator of maternal–fetal iron transport (Bierings et al., 1991). Its expression varies according to iron status, underscoring its essential role in maintaining adequate fetal iron supply.

In the endometrium, Mizuuchi et al. used immunohistochemistry to assess TfR1 distribution and found strong expression in the parabasal layer of the squamous epithelium, whereas the basal, intermediate, and superficial layers showed no detectable signal (Mizuuchi et al., 1988). This expression pattern suggests that this receptor may contribute to the proliferative activity of specific epithelial cell populations within the endometrial tissue.

2.1.8 Expression in disease

TfR1 expression is elevated in rapidly dividing cells (Zhang et al., 2025) and is upregulated as an adaptive response to cellular iron deficiency (Meyron-Holtz et al., 2004). Since cancer cells require large amounts of iron to sustain their rapid growth, it is markedly overexpressed in tumors (Mojarad-Jabali et al., 2022; Candelaria et al., 2021). Notably, metastatic cancers can exhibit TfR1 levels up to one hundred times higher than those observed in healthy tissues (Therapeutics, 2017; Horniblow et al., 2017; Kindrat et al., 2016; Wang et al., 2016; Singh et al., 2011; Rosager et al., 2017), with receptor densities ranging from approximately 10,000 to 100,000 molecules per cell. This overexpression is driven by cell growth-related factors, which actively stimulate TfR1 expression in proliferating cells by interacting with the 5' flanking region of the TfR1 gene (Recalcati et al., 2017). Increased TfR1 expression has been detected across multiple cancer types (Figure 2.5), including breast cancer (Miller, 2011; Pizzamiglio et al., 2017), lung cancer (Villalobos-Manzo et al., 2022), pancreatic cancer (Guo et al., 2025; Rychtarcikova et al., 2016), brain cancer (Koneru et al., 2021), colon cancer (Cui et al., 2019), prostate cancer (Li et al., 2023) as well as in hematological cancers such as leukemias (Smilevska et al., 2006) and lymphomas (Shimosaki et al., 2017).

Beyond oncology, abnormal TfR1 upregulation has also been implicated in other diseases, such as Alzheimer's disease (Petralla et al., 2024), asthma (Wang et al., 2022b), depression (Chang et al., 2022), and idiopathic pulmonary fibrosis (Boyle et al., 2025). Overall, several studies indicate that TfR1 expression frequently correlates with tumor aggressiveness and proliferative activity. In hepatocellular carcinoma, TfR1 levels increase with disease progression, suggesting a role in tumor growth and development. Similarly, in breast cancer, elevated TfR1 expressions have been associated with poor prognosis and higher tumor grade. Histopathological analyses further demonstrate that TfR1 expression is low in benign breast lesions but progressively increases in precancerous and invasive tumors, reaching the highest levels in high-grade cancers (Cao et al., 2022). Importantly, TfR1 expression is not homogeneous within tumors; significant variability has been observed both between patients and among individual cells within the same tumor, highlighting the presence of intratumoral heterogeneity (Fontana et al., 2023).

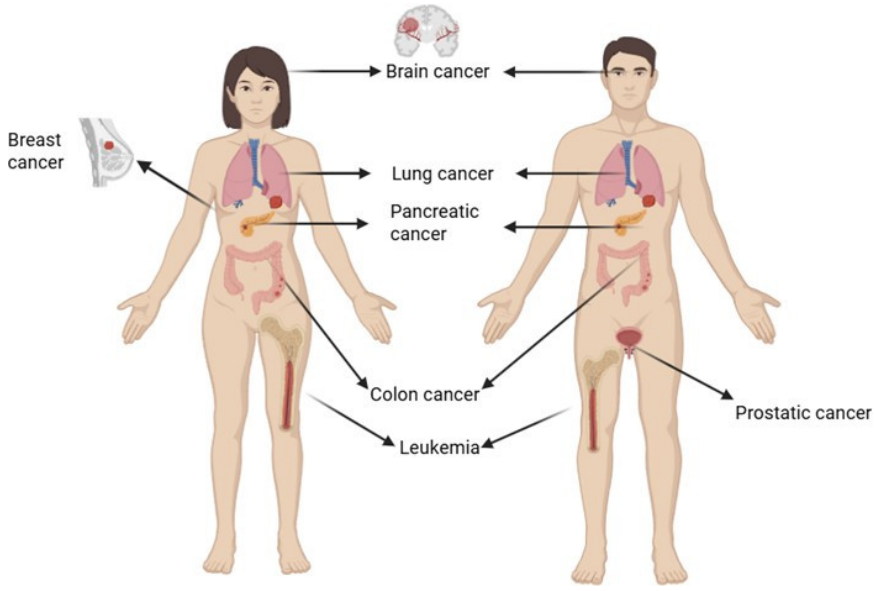


Figure 2.5: Schematic representation of major cancer types associated with TfR1 overexpression. Image generated using 2025 Biorender.

The illustration (Figure 2.5) depicts the principal malignancies in which TfR1 is highly expressed, highlighting its broad relevance as a therapeutic target. In females, its overexpression is reported in breast, lung, pancreatic, colon cancers, brain tumors, and hematological malignancies such as leukemia. In males, elevated TfR1 levels are similarly observed in lung, pancreatic, colon, and brain cancers, as well as in prostate cancer and leukemia. This emphasizes the widespread involvement of TfR1 in both solid tumors and hematological malignancies, underscoring its potential as a versatile target for TfR1-mediated drug delivery strategies.

2.1.9 Solid tumors

2.1.9.1 Pancreatic cancer

TfR1 expression is absent in healthy pancreatic tissue and in most benign neuroendocrine tumors of the pancreas. Conversely, Ryschich et al. reported that immunohistochemical analysis detected TfR1 protein expression in 93% of malignant pancreatic epithelial tumors, showing either diffuse positive staining (82%) or heterogeneous staining confined to subsets of tumor cells (11%) (Ryschich et al., 2004). Notably, Osmola et al. analyzed the GEPIA dataset and reported significantly elevated Tfrc mRNA levels in pancreatic ductal adenocarcinoma (PDAC) tissues relative to normal pancreas (Osmola et al., 2023).

Consistent with this date, (Yang et al., 2022) performed an integrated bioinformatic and experimental study combining TCGA and GEPIA datasets with validation in different PDAC cell lines (PANC-1, MIA PaCa-2, SW1990, Capan-2, BxPC-3, PaTu8988T, HPAF-II, Capan-1). Their results demonstrated that Tfrc mRNA expression is significantly upregulated in PDAC tissues, and Western blot and immunofluorescence analyses confirmed markedly higher TfR1 protein levels in PDAC cell lines compared with non-transformed pancreatic ductal cells (HPDE6-C7). In PDAC cells, TfR1 facilitates mitochondrial respiration and ROS production, thereby supporting tumorigenic growth. Its overexpression enhances oxidative phosphorylation and promotes mitochondrial ROS generation (Jeong et al., 2016). In their study, the authors further demonstrated that PDAC cell proliferation critically depends on TfR1 expression. Using lentiviral short hairpin RNAs (shRNAs) to stably knock down TfR1 in 8988T cells, they observed a marked reduction in cell proliferation. Moreover, TfR1 silencing significantly impaired clonogenic capacity, reducing the ability of PDAC cells to form colonies.

2.1.9.2 Brain cancer

In brain tumors, particularly astrocytomas, TfR1 expression is markedly elevated, with glioblastoma multiforme (GBM) exhibiting the highest levels (Recht et al., 1990; Bataille Backer and Adesina, 2025; Zhao et al., 2025). (Chirasani et al., 2009) confirmed through Western blot analysis that it is strongly overexpressed in human U373 glioma cells compared with low-grade 1321N1 astrocytoma cells and primary astrocytes. In gliomas, TfR1 enhances intracellular iron accumulation, which contributes to tumor progression through two main processes: increasing the rate of cell proliferation, driving aggressive tumor growth, and stimulating glutamate production, facilitating the expansion of the tumor mass (Hall et al., 1992; Richardson, 2002).

Moreover, in gliomas, its expression has also been found to be strongly associated with several unfavorable prognostic factors, including tumor immune microenvironment alterations, high tumor mutational burden (TMB), m6A RNA modifications, and ferroptosis, particularly in lower-grade gliomas (LGG) (Wu et al., 2017). The identification and validation of this receptor assist in predicting prognosis and immune infiltration in lower grade glioma. This suggests that TfR1 could serve as a key molecular marker for assessing glioma aggressiveness and guiding targeted therapeutic strategies.

2.1.9.3 Breast cancer

In breast cancer, TfR1 expression is upregulated (Faulk et al., 1980), with levels reaching up to fivefold higher in malignant tissues compared with healthy tissues (Habashy et al., 2010). This overexpression emerges early during tumorigenesis, as TfR1 is strongly expressed in preneoplastic ductal carcinoma in situ (DCIS), suggesting that its upregulation begins at the initial stages of malignant transformation (Wang et al., 2022a). As the tumor progresses, elevated TfR1 levels have been correlated with increased tumor aggressiveness, accelerated proliferation, and poorer clinical outcomes, particularly in estrogen receptor-negative (ER-) and triple-negative breast cancer (TNBC) subtypes, reinforcing its role in tumor progression and severity (Imam et al., 2025; Zhao and Richardson, 2023). According to a study by Corte-Rodríguez et al. (2019), MDA-MB-231 breast cancer cells, which exhibit a more aggressive and proliferative phenotype, show significantly higher TfR1 expression compared to MCF7 cells, which are less malignant (Table 2.1) (Corte-Rodríguez et al., 2019). Furthermore, a comprehensive histopathological analysis of TfR1 expression across different breast lesions has demonstrated a progressive increase, with low expression in benign lesions, moderate expression (>50% of cells) in DCIS, and high expression (>80% of cells) in invasive breast carcinoma. In contrast, normal breast epithelium exhibited only minimal TfR1 expression, reinforcing the concept that its overexpression closely correlates with malignancy and disease progression (Singh et al., 2011).

2.1.9.4 Lung cancer

TfR1 is markedly overexpressed in lung cancer and is found at elevated levels in approximately 88% of non-small cell lung carcinoma (NSCLC) cases (Sabir et al., 2021). In particular, the NSCLC cell lines A549 (EGFR wild type, KRAS mutant) and PC9 (EGFR mutant, KRAS wild type) exhibit a 3- to 11-fold increase in TfR1 expression compared with normal bronchial epithelial cells (Zhang et al., 2025). Its presence in NSCLC has also been associated with poorer prognosis in certain patient subgroups (Wu et al., 2017). Whitney and colleagues conducted a study to evaluate TfR1 expression and its prognostic relevance in NSCLC (Whitney et al., 1995).
Their analysis included 32 patients with an average follow-up of 27 months. The cohort consisted of 17 patients with adenocarcinoma, 14 with squamous cell carcinoma, and 1 with large cell carcinoma. Immunostaining analysis revealed that healthy lung tissue showed no detectable TfR1 expression, whereas 76% of adenocarcinomas, 93% of squamous cell carcinomas, and the single large cell carcinoma case exhibited positive staining. Although its expression did not show a significant correlation with overall survival in the entire cohort, patients with larger tumors (T2–T3) and high TfR1 expression had significantly shorter survival.

Moreover, subsequent studies demonstrated that blocking it with specific anti-TfR1 Abs markedly reduced the proliferation of lung adenocarcinoma cells, indicating that TfR1 plays a critical role in sustaining the growth and survival of lung cancer cells (Wu et al., 2018).

2.1.9.5 Colon cancer

Research has shown that TfR1 is physiologically expressed in colonocytes but is overexpressed in colon cancer (Voth et al., 2015). Prutki et al. (2006), reported that 95% of normal colonic mucosa samples exhibited weak membranous TfR1 staining, whereas 48% of colorectal carcinoma specimens displayed its strong expression. In colon tumor tissues, TfR1 was localized both in the cytoplasm and along the basolateral membrane of epithelial cells (Kim et al., 2023). Moreover, in colorectal cancer, upregulated TfR1 expression activates the IL-6/IL-11–STAT3 signaling cascade, which promotes cellular proliferation and inhibits apoptosis, thereby contributing to tumor progression (Ding et al., 2025). Conversely, reducing Tfrc expression in colon cancer has been correlated with shorter overall survival compared with cases exhibiting high Tfrc levels (Guo et al., 2021).

2.1.9.6 Prostate cancer.

TfR1 is also commonly overexpressed in prostate cancer cells, playing an essential role in fulfilling the increased iron demands required for their accelerated proliferation (Khan et al., 2020; Johnson et al., 2014). In line with this, Deng and coworkers reported significantly increased TfR1 expression across various prostate cancer cell lines, including LNCaP, VCaP, PC3, and DU145 (Deng et al., 2017). Earlier studies by Keer et al. demonstrated that receptor levels in malignant prostatic epithelial cells were nearly tenfold higher than those observed in benign prostatic hyperplasia (BPH), with expression confined to the epithelial compartment (Keer et al., 1990). Consistently, Kuvibidilaet et al., found that both TfR1 mRNA and protein levels are markedly elevated in prostate cancer tissues compared with normal prostate, underscoring its potential as a diagnostic biomarker (Kuvibidila et al., 2018).
More recently, a study confirmed that prostate tumors display a substantial increase in iron uptake accompanied by TfR1 upregulation, suggesting that enhanced TfR1 expression represents an early event in malignant transformation (Zapala et al., 2021). Nevertheless, its overexpression persists and often intensifies in advanced stages, as tumors maintain an iron-dependent metabolism to sustain uncontrolled proliferation.

Origin	Cell line/model	TfR1 Expression (no. per cell)	Culturing media	Analysis method	Reference
human blood	CCRF-CEM	1.9×10^5	RPMI-1640 + glutamine + 10% FCS	flow cytometry	Musgrove et al., 1984
human skin	PMC-22B	6.9×10^4	RPMI-1640 + glutamine + 10% FCS	flow cytometry	Musgrove et al., 1984
human breast	MCF7	2.3×10^5	DMEM + 10% FBS	ICP-MS and SC- ICP-MS	Rodríguez et al, 2019
human breast	MDA-MB-231	1.3×10^6	DMEM + 10% FBS	ICP-MS and SC- ICP-MS	Rodríguez et al, 2019
human placenta	BeWo cells	3.7×10^5	DMEM/F-12 + 10% FBS	radioisotope labeling + scatchard analysis	Hamilton et. al, 1979
bovine brain/rat brain	primary BBCECs / primary rat astrocyte coculture	3.5×10^4	DMEM + serum + bFGF	radioisotope labeling	Descamp s et al., 1996
rat reticulocytes	primary rat reticulocytes	5×10^4 (young) – 1×10^5 (old)	N/A (*ex vivo* isolated cells)	radioisotope labeling	R'zik et al., 2001
rat foetal liver	primary rat foetal liver erythroid cells	3×10^5 (early) – 8×10^5 (intermed iate)	Hams F-12 + 10% FCS.	radioisotope labeling	Jacopetta et al., 1982
rat liver	rat hepatocytes and non-parenchymal liver cells	2.09×10^4	HBSS + 1% BSA	radioisotope labeling	Vogel et al., 1987

Table 2.1: Comparative overview of TfR1 expression in healthy and tumor cell lines.
n.a: not applicable
ICP-MS: inductively coupled plasma mass spectrometry
SC-ICP-MS: single-cell inductively coupled plasma mass spectrometry

The analysis of TfR1 expression reveals significant differences among various cell lines, suggesting that iron metabolism may vary depending on the tissue of origin and experimental conditions. Brain capillary endothelial cells, such as the bovine model listed in the table, exhibit a moderate expression of TfR1, likely to reflect their regulatory function at the BBB and consistent with observations in humans and in rodents (Pardridge, 2020). In contrast, tumor-derived cells such as human melanoma (PMC-22B) and breast cancer lines (MCF7, MDA-MB-231) display markedly elevated TfR1 expression, consistent with their increased iron requirements to sustain rapid proliferation. Human placental choriocarcinoma cells (BeWo) also show high receptor levels, in line with the critical role of the placenta in mediating maternal–fetal iron transfer. Similarly, erythroid precursors from rat fetal liver express particularly high amounts of TfR1, underscoring the centrality of this receptor in hemoglobin synthesis during erythropoiesis (van Bockxmeer and Morgan, 1979).

Variability in reported TfR1 expression levels may arise from the different techniques employed, since each method has its own sensitivity and limitations. Factors such as detection protocols, Ab specificity, and quantification strategies can significantly affect the consistency and comparability of results across studies.

2.1.10 Hematological malignancies

2.1.10.1 Leukemia

TfR1 expression is notably higher in several malignant immune cells, including adult T-cell leukemia/lymphoma (ATLL), and often correlates with poor prognosis (Moura et al., 2004; Habashy et al., 2010; Ryschich et al., 2004; Płoszynska et al., 2012; Wu et al., 2006). Zhang and colleagues analyzed TfR1 expression levels in various cell lines, comparing 11 non-tumorigenic cell lines to 10 cancerous ones (Zhang et al., 2025). Among the cell types analyzed, leukemic cells exhibited the highest TfR1 levels, with more than a 20-fold increase relative to normal cells. Another study demonstrated that poorly differentiated acute myeloid leukemias (AMLs), including minimally differentiated AML, AML without maturation, AML with maturation, and acute myelomonocytic leukemia, frequently expressed high levels of TfR1 on leukemic blasts (Liu et al., 2013). In contrast, partially differentiated AMLs, such as acute promyelocytic leukemia and acute monocytic leukemia, were associated with lower receptor expression. Moreover, B-cell acute lymphoblastic leukemia (B-ALL) displayed significantly reduced levels compared to AML, mixed phenotype acute leukemia (MPAL), and normal bone marrow precursors. In seven cases of acute erythroid leukemia (AEL), leukemic cells exhibited minimal expression, which was markedly lower than that observed in acute megakaryocytic leukemia and in poorly differentiated AML or normal blasts (Liu et al., 2014).

2.1.10.2 Lymphoma

TfR1 is widely expressed across various subtypes of B- and T-cell non-Hodgkin lymphomas (NHL). Two early independent studies examined its distribution using the monoclonal Ab OKT9 (Medeiros et al., 1988) (Habeshaw et al., 1983). In the study by Medeiros et al., involving 267 cases of NHL and related neoplasms, TfR1 was found to be broadly detectable in both low- and high-grade lymphomas, with a general trend toward higher expression in more aggressive subtypes. However, some histological variants diverged from this pattern. For instance, low-grade follicular lymphomas expressed the receptor more frequently than diffuse low-grade lymphomas, while immunoblastic high-grade lymphomas showed lower expression compared to other high-grade variants. Intermediate lymphocytic lymphomas displayed weak and sporadic TfR1 expressions.

In the study by Habeshaw et al. (1983) lymph node biopsy samples from NHL patients were analyzed to quantify the proportion of TfR1-positive lymphocytes using the same OKT9 Ab. Their results revealed a strong correlation between TfR1 expression and histological grade: high-grade lymphomas exhibited a mean of 22.5% OKT9-positive lymphocytes (range 3–57%), whereas low-grade lymphomas showed a mean of 2.5% (range <1–22%). These findings support the hypothesis that TfR1 expression mirrors the tumor's proliferative activity and, consequently, its biological aggressiveness.

2.1.11 Other diseases

2.1.11.1 Asthma

Wang et al. reported that TfR1 expression in sputum-derived airway cells from asthmatic patients is significantly associated with disease severity (Wang et al., 2022b). Elevated TfR1 levels correlate with reduced lung function and increased pro-inflammatory activity, suggesting that it may contribute to disease progression and could serve as a potential biomarker for asthma monitoring. Consistently, in patients with asthma, its expression is markedly upregulated in airway cells, particularly in macrophages and bronchial epithelial cells. This increased expression is linked to impaired lung function and enhanced Type-2 (T2) inflammatory responses, characterized by increased ILC2 activity and elevated production of IL-4, IL-5, and IL-13. Experimental evidence further demonstrates that TfR1 overexpression is accompanied by pulmonary iron accumulation, which promotes the release of pro-inflammatory mediators and extracellular matrix components by airway smooth muscle cells and fibroblasts, thereby contributing to airway hyperresponsiveness and fibrosis, which are hallmark features of asthma (Ali et al., 2020).

2.1.11.2 Alzheimer

Growing evidence indicates that alterations in iron metabolism contribute to the pathogenesis of Alzheimer's disease (AD), with particular emphasis on the role of TfR1. Preclinical studies have shown significantly elevated TfR1 mRNA and protein levels in the cerebral cortex of AD mouse models compared to wild-type controls (Tian et al., 2024). Consistent observations have been reported in cellular models that more closely mimic the human condition, such as neural cells differentiated from induced pluripotent stem cells (iPSCs) derived from AD patients. In these systems, TfR1 expression was found to be upregulated during neuronal differentiation, suggesting a potential functional involvement (Kang et al., 2024). In contrast, Bourassa et al. demonstrated that receptor levels are not elevated in human AD brains (Bourassa et al., 2019).

Analyses of post-mortem tissue from the parietal cortex and hippocampus revealed no significant differences in TfR1 expression between individuals with or without AD. Similarly, its concentration in brain microvessels did not differ between AD patients and healthy controls. Taken together, these findings reveal a clear discrepancy between human and animal data. While murine and iPSC-based models suggest an upregulation of this receptor, human post-mortem studies indicate that TfR1-mediated iron transport remains largely preserved in AD. Notably, this preservation supports the continued exploration of TfR1 as a viable target for brain drug delivery. Importantly, in neurodegenerative diseases increased TfR1 expression does not necessarily reflect systemic iron deficiency, but rather alterations in local iron homeostasis. Aging and neuroinflammatory processes can profoundly reshape iron handling in the brain, leading to iron redistribution and cell-specific imbalances in iron availability. Under these conditions, iron may accumulate in specific regions or cell types while remaining poorly accessible for metabolic use, resulting in a functional iron-deficient state at the cellular level. Inflammatory signaling further contributes to this dysregulation: pro-inflammatory cytokines can enhance neuronal iron uptake and promote intracellular iron accumulation, whereas anti-inflammatory signals such as IL-4 have been shown to upregulate TfR1 expression to facilitate Tf-mediated iron uptake and support repair processes. Together, these mechanisms indicate that TfR1 upregulation in neurological disorders is likely to represent a compensatory response to disrupted iron homeostasis rather than a simple consequence of systemic iron deficiency (Levi et al., 2024).

2.1.11.3 Depression

Using quantitative proteomic analyses, Chang and coworkers investigated the expression profiles of Tf and its receptor TfR1 in healthy mice and those subjected to chronic social defeat stress (CSDS), a well-established murine model of depression (Chang et al., 2022). Their results showed a marked upregulation of both not only in the liver but also in the peripheral blood and several brain regions of CSDS-exposed mice compared to controls.

2.1.11.4 Idiopathic Pulmonary Fibrosis

In idiopathic pulmonary fibrosis (IPF), TfR1 expression is downregulated, contributing to significant dysregulation of iron metabolism. Under physiological conditions, it is abundantly expressed on alveolar macrophages, where it facilitates cellular iron uptake. In contrast, IPF is characterized by a marked increase in CD71-negative macrophages, cells lacking the TfR1. This phenotypic shift correlates with poorer clinical outcomes and represents an independent predictor of mortality (Boyle et al., 2025).

2.1.12 Soluble TfR in health and disease

2.1.12.1 Biogenesis and Physiological Role of sTfR

A soluble, circulating form of transferrin receptor (sTfR) has been identified in both human and animal serum. This truncated monomeric variant lacks the N-terminal 100 amino acids and circulations as part of a complex with Tf (Beguin, 2003). sTfR is generated through proteolytic cleavage, primarily mediated by a membrane-associated serine protease acting on exosomal surfaces within multivesicular bodies prior to exocytosis (Baynes et al., 1994). Its Serum levels of sTfR closely reflect cellular iron requirements and the rate of erythroid proliferation (Speeckaert et al., 2010).

2.1.12.2 sTfR in healthy subjects

Allen et al. measured the concentrations of sTfR in 225 healthy adults (Allen et al., 1998). The study did not show any differences in reference values between men and women, nor any correlation between sTfR levels and age. However, black subjects had significantly higher concentrations compared to non-black subjects, and individuals living at high altitude showed higher levels than those living closer to sea level. Moreover, values tend to be modestly elevated in fetuses and newborns compared to adults. During the early postnatal phase, sTfR concentrations resemble those seen in adults experiencing bone marrow suppression but soon begin to rise again. As a result, infants (Virtanen et al., 1999) and adolescents (Anttila et al., 1997) typically exhibit slightly higher levels than the adult population.

2.1.12.3 sTfR in disease

Erythropoietic activity is recognized as the most influential factor in determining sTfR concentrations (Kohgo et al., 1986; Flowers et al., 1989). Several studies have also reported significant associations between sTfR levels and chronic diseases. For instance, a longitudinal study demonstrated that elevated sTfR concentrations are associated with an increased risk of diabetes mellitus in overweight and obese individuals, while a cross-sectional study reported a positive correlation between sTfR levels and the prevalence of chronic kidney disease (Kang et al., 2022). Low sTfR levels are typically observed when bone marrow erythroid activity is suppressed or absent, such as in hypertransfusion, chronic renal failure, severe aplastic anemia, or post-intensive chemotherapy (Beguin et al., 1993). Conversely, elevated sTfR levels reflect increased erythroid proliferation, as seen in congenital dyserythropoietic anemia, hemolytic anemia, hereditary spherocytosis, sickle cell disease, thalassemia (major and intermedia), megaloblastic anemia, and secondary polycythemia. The values of sTfR vary widely: in individuals with no erythropoietic activity, levels drop to approximately 0.5 mg/l, reflecting minimal production from non-erythroid tissues.

This value is markedly lower than that observed in healthy adults, showing a mean sTfR concentration of around 5 ± 1 mg/L. In contrast, patients suffering from severe anemia due to thalassemia may present levels reaching up to 100 mg/L (Huebers et al., 1990). A recent discovery by (Kang et al., 2024) revealed that elevated levels of sTfR are significantly associated with increased all-cause mortality and a greater risk of developing chronic kidney disease (CKD). This relationship persists regardless of the presence of anemia or iron storage status, positioning sTfR as an independent prognostic marker in the general population. Moreover, a study conducted by Zhu et al. demonstrated that elevated sTfR levels are associated with a higher prevalence of cardiovascular diseases (Zhu et al., 2022). Finally, patients with systemic lupus erythematosus (SLE) exhibited significantly higher median serum concentrations of sTfR compared to healthy controls (Winikajtis-Burzyńska et al., 2023).

2.1.12.4 sTfR in cancer

Zhang and colleagues demonstrated that elevated serum levels of sTfR are associated with a higher prevalence of cancer, particularly in sex-specific malignancies (Zhang et al., 2022). Consistently, a different study investigated its role in patients with hepatocellular carcinoma (HCC) and underlying liver cirrhosis and reported significantly higher serum levels in HCC patients compared to cirrhotic controls, suggesting that increased sTfR expression may reflect enhanced iron demand and tumor proliferative activity (Mehta et al., 2005). Furthermore, analysis of sTfR concentrations in 82 patients with malignant lymphomas showed elevated levels unrelated to iron deficiency anemia (Bjerner et al., 2002).
The authors proposed that increased its expression reflects tumor burden and disease severity rather than alterations in iron stores, thereby supporting its potential utility as a biomarker of tumor progression in hematological malignancies. Moreover, Metzgeroth et al. demonstrated that serum sTfR levels correlate directly with tumor burden in patients with chronic lymphocytic leukemia (CLL) (Metzgeroth et al., 2007). In their study involving 61 previously untreated CLL patients, both hemolysis and iron deficiency were excluded as potential confounders. The authors measured sTfR concentrations and found that patients in early-stage disease (Binet A) showed normal levels (1.36 ± 0.22 mg/L), whereas those in intermediate-stage disease (Binet B) exhibited significantly elevated concentrations (3.08 ± 1.70 mg/L; $p < 0.0001$). Although levels increased further in advanced-stage disease (Binet C) (3.75 ± 2.32 mg/L), this difference was not statistically significant compared with Binet B. Importantly, sTfR values decreased or normalized following successful therapy, while disease relapse or progression was accompanied by a renewed increase. These findings indicate that sTfR serves as a reliable indicator of tumor mass and disease activity in CLL, independent of iron status.

Therefore, sTfR may represent a potential biomarker for patient stratification in TfR1-targeted therapies. However, the interpretation of sTfR concentrations in cancer patients may be complicated by potentially confounding clinical factors, including iron deficiency, increased erythropoietic activity, and diseases discussed in the previous paragraph, such as chronic kidney disease.

2.2 Nanoparticle Drug Delivery Systems

The preceding overview establishes the biological rationale for TfR1-directed drug delivery by examining receptor expression, cellular iron uptake, and the significance of circulating sTfR in health and disease. Building on this background, the discussion now shifts from the biological target to the delivery platform. Whereas sTfR has been considered primarily as a circulating biomarker, membrane-associated TfR1 provides the target for carrier recognition and receptor-mediated uptake. Translating this targeting rationale into a delivery strategy requires consideration of both the carrier and its surface functionalization. The following section therefore introduces nanoparticle drug delivery systems, focusing on lipid-based carriers, with particular emphasis on liposomes as the platform selected for nanobody functionalization in this thesis.

2.2.1 Lipid-Based Systems

Nanotechnology-based drug delivery systems (NDDSs) offer an innovative approach to achieve controlled and site-specific drug release (Chen et al., 2023). Numerous advantages have been attributed to NP-mediated drug delivery, including enhanced solubility of poorly water-soluble drugs, prolonged systemic circulation, and the ability to provide sustained and controlled release. Moreover, NPs enable selective accumulation of therapeutics within target tissues or cells and can simultaneously deliver multiple pharmacological agents to the same site, thereby facilitating combination therapy (Zhang et al., 2008; Davis et al., 2008). The term NPs encompass a diverse range of delivery platforms, such as micelles, dendrimers, polymeric NPs, magnetic NPs and LNPs. In this thesis, lipid-based NPs are discussed in detail, with particular focus on liposomes as key representatives of this class for TfR1–targeted drug delivery.

Nano-particles	**Targeting ligand**	**Drug**	**Indication**	***In vitro***	***In vivo***	**Reference**
SLNs and NLCs	transferrin	curcumin	neuro-degenerative, brain tumors	hCMEC/D3 cells	n.d	Neves et al., 2021
liposomes	transferrin	G3139	leukemia	K562 cells	n.d	Chiu et al., 2006
liposomes	DT7 peptide (D-HAIYPRH)	docetaxel	hepatocellular carcinoma	human carcinoma cells	n.d	Tang et al., 2019
liposomes	transferrin	caffeic acid	Alzheimer	n.d	n.d	Andrade et al., 2023
liposomes	transferrin	doxorubicin	lung cancer	haEPC, A549, Calu3 cells	n.d	Anabousi et al., 2006
LNPs	transferrin	siRNA	asthma	Jurkat cells	n.d	Jürgens et al., 2024
LNPs	RI7-217 monoclonal antibody	luciferase	glioblastoma	U-87 MG cells	n.d	Kato et al., 2024
SLNs and NLCs	transferrin	quercetin	Alzheimer	hCMEC/D3	n.d	Pinheiro et al., 2020
liposomes	transferrin	n.r.	n.r.	BAOEC	n.d	Voinea et al., 2002
liposomes	OX26	n.r.	n.r.	n.d	18-day-old rats	Gosk et al„ 2004
LNPs	transferrin	siRNA	cancer	HepG2 cells	n.d	Li et al., 2017
liposomes	transferrin	sirolimus	breast cancer	BT-474 cells	n.d	Nandi et al., 2021
liposomes	transferrin	docetaxel	cancer	K562 cells	n.d	Zai et al., 2010
liposomes	transferrin	doxorubicin	hepatocellular carcinoma	HepG2 cells	HepG2 xenograft in ICR mice; PK in rats	Li et al., 2009
liposomes	transferrin	resveratrol	glioblastoma	U-87 MG GBS cells	U-87 xenograft in nude mice	Jhaveri et al., 2018
liposomes	transferrin	artemisinin	colorectal cancer	HCT-8 cells	n.d	Leto et al., 2016
LNPs	T7 peptide (L-HAIYPRH)	ASOs (anti-Bcl-2 + anti-Akt-1)	lung cancer and cervical carcinoma	KB and A549 cells	A549 xenograft in nude mice	Cheng et al., 2018
liposomes	transferrin	doxorubicin	cancer	MDR cancer cells	n.d	Kobayashi et al., 2007
liposomes	transferrin	anti-BCR-ABL siRNA or asODN	leukemia	leukemia cell lines	n.d	Mendonça et al., 2010

Table 2.2: Overview of lipid nanoparticles with anti-TfR1 ligands.
n.d.: not done; n.r.: not reported; MDR: multidrug resistance.

Table 2.2 provides a comparative overview of TfR1-targeted lipid-based nanocarrier systems reported in the literature, employing a wide range of ligands, including native Tf, peptides (e.g., T7, D7), Abs (e.g., OX26, RI7-217), and small ligand analogues, to enhance selective uptake into cancer and disease-relevant cells. The therapeutic cargos delivered by these systems span from classical chemotherapeutics such as doxorubicin, docetaxel, and artemisinin, to natural compounds including curcumin, quercetin, and resveratrol, as well as modern nucleic acid–based approaches such as siRNA and antisense oligonucleotides. Applications extend across multiple pathological contexts, including leukemia, glioblastoma, hepatocellular carcinoma, breast, lung, and colon cancers, as well as Alzheimer's disease and asthma. Reported studies range from in vitro evaluations in diverse human cell lines to in vivo validation in rodent xenograft models. Collectively, this compilation illustrates both the versatility of lipid-based nanocarriers and the strategic importance of ligand selection in shaping therapeutic outcomes, while highlighting that, although these systems show substantial preclinical promise, clinical translation has yet to be firmly established.

2.3 Liposomes

Liposomes represent one of the most extensively investigated nanocarrier platforms for drug delivery. Structurally, they are spherical vesicles composed of one or more phospholipid bilayers enclosing an aqueous core, closely resembling the architecture of biological membranes (Figure 2.6) (Chelliah et al., 2025). Phospholipid molecules are amphiphilic, consisting of a hydrophilic head group and a hydrophobic tail. When dispersed in an aqueous medium, they spontaneously self-assemble, orienting their hydrophilic heads toward the aqueous environment and their hydrophobic tails inward, away from the surrounding water (Kawak et al., 2023).

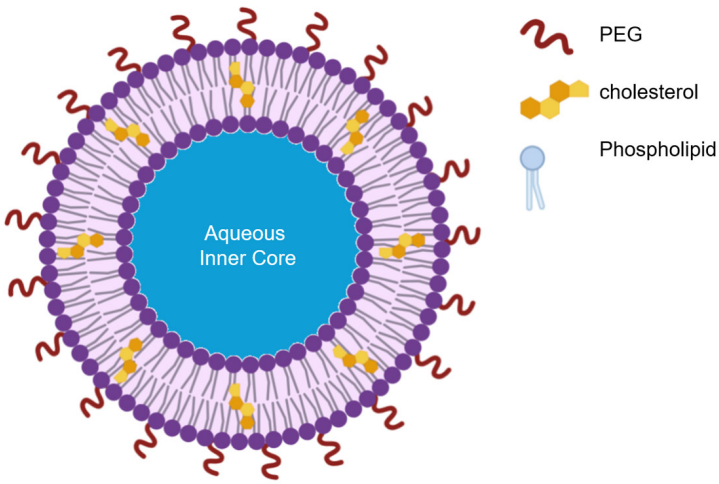


Figure 2.6: Liposomes structure. Image created with Biorender 2025.

Liposomes are versatile nanocarriers with excellent biocompatibility, biodegradability, and structural adaptability. By encapsulating hydrophilic and hydrophobic compounds, they can improve drug solubility and reduce adverse effects. PEGylation prolongs systemic circulation and improves pharmacokinetics, while straightforward preparation facilitates large-scale manufacturing (Yan et al., 2020; Karim et al., 2016). Numerous liposomal formulations have been engineered to target TfR1 and improve the specificity and efficiency of anticancer drug delivery to tumor cells (Kang et al., 2020; Tang et al., 2019; AlSawaftah et al., 2021; Lam et al., 2018; Li et al., 2023) (Table 2.3). TfR1-targeted liposomes have also been widely investigated for drug delivery to the brain (Table 2.4).

Nano-particle	**Size (nm)**	**Ligand**	**Drug**	**Target**	**Admin route**	**Animals**	**Injection dose**	**Reference**
liposome	70 ± 19	transferri	doxorubicin	hepatocellular carcinoma	i.v.	ICR tumor-bearing mice; rats (PK study)	1.5–3 mg/kg (antitumor) 5 mg/kg (PK study)	Li et al., 2009
liposome	164 ± 43	transferri	doxorubicin	cervical carcinoma	i.v.	athymic nude mice	4 mg/kg	Sriraman et al., 2016
liposome	88.63 ± 4.21	transferri	erianin	liver cancer	i.v.	BALB/c nude mice	2 mg/kg	Yang et al., 2021
liposome	113 ± 2	transferri	plumbagin	melanoma	i.v.	BALB/c mice	2 mg/kg	Sakpakdeejaroen et al., 2019
liposome	210	transferri	resveratrol	glioblastoma	i.v.	athymic nude mice	10 mg/kg	Jhaveri et al., 2018
liposome	130.33± 1.89	transferri	triptolide	hepatocellular carcinoma	i.v	BALB/c nude mice	0.2 mg/kg	Zhao et al., 2023
liposome	153 ± 3.4	transferri + glioma cell membrane proteins	elemene + cabazitaxel	glioma	i.v.	BALB/c nude mice	2.5 mg/kg (loading dose), then 0.625 mg/kg ×5	Zeng et al., 2021
liposome	∼190	transferri	sirolimus	breast cancer	i.v.	nude mice	20 mg/kg	Nandi et al., 2021
liposome	97.06 ± 3.38 9	transferri	carnosic acid	liver cancer	i.v.	BALB/c nude mice	2 mg/kg	Liu et al., 2021

Table 2.3: TfR1-targeted liposomes for cancer therapy.

Table 2.3 provides an overview of in vivo studies assessing the therapeutic performance of (TfR1)–targeted liposomes in tumor-bearing animal models. A substantial body of work has focused on TfR1-functionalized liposomes encapsulating doxorubicin, demonstrating enhanced antitumor efficacy in hepatocellular carcinoma and cervical cancer xenografts (Li et al., 2009; Sriraman et al., 2016). Beyond classical chemotherapeutics, TfR1-targeted liposomes have been employed to deliver natural compounds and small-molecule agents such as resveratrol, plumbagin, erianin, triptolide, carnosic acid, and sirolimus, showing improved tumor growth inhibition across glioblastoma, melanoma, breast, and liver cancer models (Jhaveri et al., 2018; Sakpakdeejaroen et al., 2019; Yang et al., 2021; Liu et al., 2021; Nandi et al., 2021; Zhao and Richardson, 2023). More complex formulations incorporating combination therapies or biomimetic components, such as glioma cell membrane proteins, further illustrate the versatility of this targeting strategy in enhancing tumor-selective drug accumulation and therapeutic outcomes (Zeng et al., 2021).

Nano-particle	**Size (nm)**	**Ligand**	**Drug**	**Admin route**	**Animals**	**Injection dose**	**Reference**
liposome	139.3 ± 1.5	OX26	oxaliplati n	i.v.	Sprague-Dawley rats	186 µg/animal	Johnsen et al., 2017
liposome	180 ± 2	OX26	cisplatin	i.v.	Sprague-Dawley rats	154 µg/kg	Olsman et al., 2021
liposome	181± 0.7	OX26	cisplatin	i.v.	Sprague-Dawley rats	340 µg/kg	Olsman et al., 2021
liposome	92.12 ± 0.95	transfer rin	rapamyci n / borneol	i.v.	C57BL/6 J mice	3 mg/kg	Cai et al., 2025
liposome	130.6 ± 3.08	transfer rin / RVG peptide	plasmid DNA (pGFP)	i.v.	C57BL/6 mice	15.2 µmol/kg	Dos Santos Rodrigues et al., 2020
liposome	196.3 ± 7.09	transfer rin	α- man-gosti n	i.v.	Sprague –Dawley rats	5 mg/kg	Chen et al., 2016
liposome	60 ± 5	transfer rin and T7 pep-tide	fluvoxami ne	i.v.	C57BL/6 mice	2 mg/kg	Mi et al., 2025

Table 2.4: TfR1-targeted liposomes for delivery to the brain.

Table 2.4 summarizes in vivo studies investigating (TfR1)–targeted liposomal formulations designed for delivery to the brain in animal models relevant to the BBB. Early work using OX26-functionalized liposomes demonstrated the feasibility of Abs-mediated transport across the BBB and its impact on brain biodistribution of platinum-based chemotherapeutics (Johnsen et al., 2017; Olsman et al., 2021).

Subsequent studies expanded this approach to alternative cargos and ligand configurations, including Tf-modified liposomes delivering rapamycin or plasmid DNA, highlighting the role of formulation parameters and ligand density in modulating brain uptake (Dos Santos Rodrigues et al., 2020; Chen et al., 2016; Cai et al., 2025). More recent investigations have explored dual-targeting strategies combining Tf with peptide ligands to further enhance BBB transcytosis efficiency (Mi et al., 2025).

2.4 Clinical Applications and Approved Formulations (FDA, EMA)

Liposomal drug delivery has become a well-established strategy in clinical therapeutics and is widely regarded as a key milestone in the evolution of nanomedicine. These properties have enabled the widespread application of liposomes across multiple areas of nanomedicine. To date, approximately twenty liposome-based formulations have received regulatory approval from agencies such as the U.S. Food and Drug Administration (FDA) and the European Medicines Agency (EMA) (Yuba, 2020). A landmark achievement in this field was the regulatory approval of the liposomal doxorubicin formulations Caelyx/Doxil in the late 1990s, which enabled improved treatment options for ovarian and breast cancers, as well as Kaposi's sarcoma.
Building on this success, a growing number of small-molecule chemotherapeutic agents have been developed and approved as liposomal formulations. These systems have demonstrated enhanced pharmacokinetic profiles, including prolonged circulation time and improved bioavailability, while significantly reducing off-target toxicity and associated adverse effects (Eugster et al., 2024). During the same period, liposomal technologies were extended beyond oncology to address other therapeutic areas. Notably, virosome-based vaccines such as Epaxal and Inflexal V were developed for infectious disease prevention. Approximately a decade later, liposomal depot formulations designed for pain management, including DepoDur and Exparel, received regulatory approval, offering sustained drug release and improved patient compliance. More recently, the scope of liposomal applications has further expanded to incorporate protein-based therapeutics used as vaccines, as exemplified by Mosquirix and Shingrix. These advancements highlight the continuous evolution and growing versatility of liposomal systems within the field of nanomedicine (Crommelin et al., 2020). In addition to these applications, liposomal formulations have shown significant potential in the treatment of infectious diseases. The increasing prevalence of bacterial resistance, particularly due to biofilm formation, represents a major challenge for conventional therapies. In this context, liposomal drug delivery enhances the effectiveness of antibacterial agents by improving drug penetration and stability, enabling activity even against highly resistant microbial communities.

A representative example is Arikayce, a liposomal amikacin formulation introduced in 2018 (Ponkshe et al., 2021). Liposomal systems have also demonstrated significant clinical success in the field of anesthesia and pain management. To date, two formulations, DepoDur and Exparel, have received regulatory approval. These products are based on multivesicular liposomal technology (DepoFoam), which enables sustained release of the active compound, maintaining therapeutic drug concentrations over extended periods. This prolonged release profile reduces the need for frequent dosing, representing a major advantage in long-term postoperative pain control.
Beyond anesthetic applications, DepoFoam technology has also been employed in other therapeutic areas. For example, DepoCyt, a liposomal cytarabine formulation approved by both the FDA and EMA, was developed for the treatment of lymphomatous meningitis rather than pain management. Furthermore, several DepoFoam-based candidates are currently under development, including DepoTXA (liposomal tranexamic acid) for surgical bleeding control and DepoMLX (liposomal meloxicam) for postoperative analgesia (Salahi et al., 2020).

2.5 Liposome Production Methods

The preparation of liposomes has been extensively investigated over the past decades, leading to the development of a wide range of production techniques. These methods can be broadly classified into conventional approaches, traditionally used at the laboratory scale, and more advanced or innovative technologies, which have been developed primarily to enable large-scale industrial production while improving reproducibility, scalability, and process control. In particular, the following sections will focus on three representative techniques: thin film hydration, as a conventional method, and microfluidics and supercritical CO_2-based technologies, as innovative approaches. In this thesis, thin-film hydration was used as the main method for the preparation of nanobody-functionalized liposomes, whereas supercritical CO_2-assisted production was explored as a preliminary scalable approach for non-functionalized liposomes. Therefore, the following sections focus on thin-film hydration as the conventional method used for the biological part of this work, and on microfluidics and supercritical CO_2-based technologies as representative innovative approaches for liposome manufacturing.

2.5.1 Conventional methods: thin-film hydration

The thin-film hydration technique (Figure 2.7) is one of the simplest and most widely used methods for liposome preparation, particularly to produce multilamellar vesicles (MLVs) (Lombardo and Kiselev, 2022).

In this method, phospholipids are first dissolved in an organic solvent, such as dichloromethane, chloroform, ethanol, or a chloroform–methanol mixture, to obtain a homogeneous solution. The organic solvent is then removed by evaporation under reduced pressure, typically using a rotary evaporator at temperatures between 45 and 60 °C. As a result of solvent removal, a thin, dry lipid film composed of stacked bilayers forms on the inner wall of the flask. This film is subsequently hydrated with an appropriate aqueous medium, such as distilled water or a buffered solution (e.g., phosphate buffer at pH 7.4). The hydration step is usually carried out at a temperature above the phase transition temperature of the lipids. The final stages of the process involve liposome downsizing, purification, and characterization, which are essential to obtain a formulation with the desired size distribution, purity, and physicochemical properties. (Andra et al., 2022). Following thin-film hydration, two widely used techniques to obtain liposomes with controlled size and low polydispersity are sonication and extrusion. Sonication, performed with either probe- or bath-type devices, reduces vesicle size through cavitation effects.

In contrast, extrusion involves forcing the liposomal suspension through a high-pressure filtration system equipped with a track-etched polycarbonate membrane, typically operated above the lipid phase transition temperature. These membranes possess uniform, well-defined pore sizes and, when properly supported, can withstand pressures up to 3000 psi. As a result, liposomes processed by extrusion exhibit a more homogeneous and narrowly distributed particle size (Xiang and Cao, 2021).

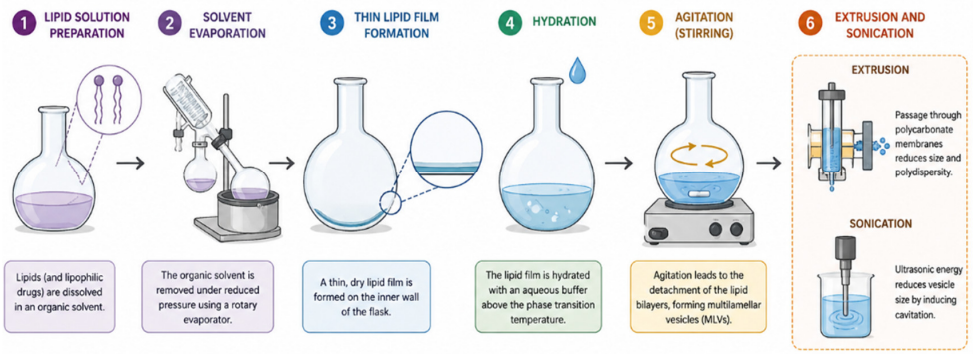


Figure 2.7: Schematic representation of thin film hydration method. Adapted from Lombardo et al., (2022).

2.5.2 Microfluidic-assisted liposome production

In this approach, lipids are dissolved in isopropyl alcohol and injected through the central channel, while aqueous phases flow through adjacent channels. The controlled mixing of these streams leads to the spontaneous formation of liposomes. Liposome size and size distribution are regulated by laminar flow conditions and lipid concentration within the microfluidic device. This technique is highly effective for direct drug encapsulation, enabling the formation of self-assembled liposomes (Yu et al., 2009).

2.5.3 Supercritical CO_2-assisted liposome production

Among the innovative techniques developed for liposome production, supercritical CO_2-assisted processes have attracted increasing interest as promising alternatives to conventional methods. In particular, the Supercritical Assisted Liposome formation process, commonly known as Super Somes (Figure 2.8), is based on three separate feeding lines for carbon dioxide, an aqueous phase, and an ethanol–phospholipid solution. The ethanol–phospholipid solution and CO_2 are continuously mixed in a homogenizer, leading to the formation of an expanded liquid phase, which is subsequently introduced into a precipitation vessel. In the same vessel, the aqueous phase is atomized into fine droplets. During this step, phospholipid molecules organize around the aqueous droplets, forming liposomal vesicles characterized by a lipid bilayer surrounding an aqueous core. Compared with conventional methods, this approach enables the production of liposomes with nanometric dimensions, improved control of particle size distribution, reduced solvent residues, and limited need for post-processing steps such as sonication or extrusion. Moreover, its continuous or semi-continuous configuration makes the process more reproducible and potentially suitable for industrial scale-up. For these reasons, supercritical CO_2-assisted liposome production represents an innovative and industrially relevant strategy for the preparation of liposomal formulations (Trucillo et al., 2020; Santo et al., 2014).

2.6 Liposome targeting strategies

The therapeutic performance of liposomes can be improved through targeting strategies aimed at increasing drug accumulation at the pathological site while reducing systemic toxicity. Liposomal targeting is generally classified into two main approaches: passive targeting and active targeting. Passive targeting mainly relies on the physicochemical properties of the nanocarrier and on the anatomical and pathophysiological features of diseased tissues, whereas active targeting involves the functionalization of the liposomal surface with specific ligands able to recognize receptors or biomarkers expressed by target cells (Attia et al., 2019).

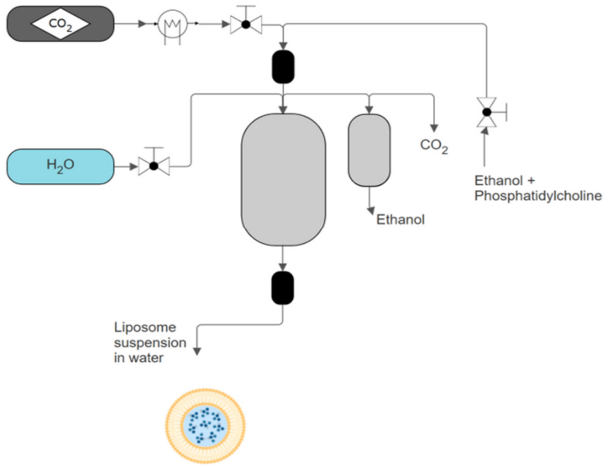


Figure 2.8: Super Somes lab-scale plant.

2.6.1 Passive vs Active Targeting

Passive targeting refers to the preferential accumulation of liposomes in pathological tissues without the use of specific recognition ligands. This process mainly depends on liposome-related features, such as nanoscale size, surface charge, lipid composition, and prolonged circulation time, as well as on the structural abnormalities of diseased tissues. In solid tumors, passive targeting is commonly associated with the enhanced permeability and retention effect, also known as the EPR effect. Tumor blood vessels are often highly permeable and poorly organized, while lymphatic drainage is inefficient. These features allow nanosized carriers, including liposomes, to extravasate and accumulate within the tumor microenvironment. The passive accumulation of liposomes can be further improved by surface modification with polyethylene glycol, a process known as PEGylation. PEGylated liposomes show reduced opsonization and decreased recognition by the mononuclear phagocyte system, resulting in prolonged blood circulation and increased probability of accumulation at the pathological site. However, passive targeting has several limitations. The EPR effect is highly heterogeneous and can vary depending on tumor type, vascularization, disease stage, and interpatient variability. Moreover, passive accumulation does not necessarily ensure efficient cellular uptake, since liposomes may remain in the extracellular matrix without being internalized by target cells (Gatto et al., 2024; Danhier et al., 2010). Active targeting was developed to enhance the interaction between liposomes and specific target cells. In this strategy, liposomes are functionalized on their surface with ligands able to recognize receptors or biomarkers overexpressed on target cells. After accumulation within the pathological tissue, ligand–receptor interactions can increase liposome affinity for the target cell surface and, in many cases, promote receptor-mediated internalization.

This may enhance intracellular drug delivery compared with free drugs or non-functionalized nano systems, while reducing nonspecific distribution and systemic side effects. The active targeting concept was first demonstrated in 1980 through the conjugation of antibodies onto the liposomal surface, paving the way for the development of ligand-functionalized nanocarriers (Leserman et al., 1980).
An important advantage of active targeting is the possibility of displaying multiple ligand molecules on the liposomal surface. This multivalent presentation can increase the overall binding avidity, even when each individual ligand has only moderate affinity for its receptor (Vu et al., 2023). Moreover, different ligands can be combined on the same carrier to improve targeting specificity and address tumor heterogeneity (Amin et al., 2022). Nevertheless, active targeting requires careful optimization, since ligand density, binding affinity, steric hindrance, receptor expression, and intracellular trafficking can strongly influence the final delivery efficiency (Muro, 2012).

2.7 Targeting ligands

Targeting ligands are molecules that can specifically recognize and bind to receptors or biomarkers overexpressed on the surface of target cells. They are commonly employed to functionalize NPs or other drug carriers, enabling selective delivery to target tissues while minimizing off-target effects. Depending on their origin and structure, targeting ligands include proteins, peptides, aptamers, carbohydrates, vitamins, and small molecules (Anarjan, 2019; Yan et al., 2024). NPs designed for TfR1-mediated targeting, through surface functionalization with Tf, Tf-mimicking peptides, or anti-TfR1 monoclonal antibodies (Abs) and nanobodies (Nbs), exhibit remarkable receptor specificity and efficient uptake via receptor-mediated endocytosis. This strategy has been shown to markedly enhance intracellular drug delivery and improve therapeutic efficacy (Kaur et al., 2022; Niewoehner et al., 2014).
However, their targeting efficiency critically depends on the precise tuning of key parameters in relation to receptor biology, including receptor density, recycling kinetics, endosomal routing, and lysosomal degradation pathways. Ligand density represents a critical design parameter for targeted NPs. Increasing the number of ligands on the NP surface can promote multivalent interactions with cell-surface receptors, thereby enhancing binding avidity and facilitating receptor-mediated uptake, which may ultimately improve therapeutic or diagnostic outcomes (Elias et al., 2012). Notably, multivalent interactions can increase binding avidity by several orders of magnitude primarily through a reduction in dissociation rate, rather than by accelerating endocytosis (Hong et al., 2006). While this enhanced binding stability can improve receptor engagement, it does not necessarily translate into more efficient internalization.

Excessively high ligand densities may also introduce several drawbacks, including reduced stealth properties due to decreased PEG coverage, increased steric hindrance, and receptor saturation, which may ultimately limit cellular uptake and reduce targeting specificity (Mesquita et al., 2022). These design considerations are particularly relevant for receptors such as TfR1, where ligand density and binding avidity can influence receptor trafficking and intracellular routing. In addition to ligand density, the affinity of targeting ligands toward their receptor represents another critical factor influencing NP uptake and intracellular trafficking. While high-affinity interactions promote strong receptor binding, excessively stable interactions may alter receptor trafficking pathways. In vitro imaging and colocalization analyses demonstrated that high-affinity Abs promote TfR1 trafficking toward lysosomal compartments, leading to receptor degradation, an effect also confirmed in vivo. Importantly, administration of high-affinity anti-TfR1 Abs reduced receptor availability in the brain, thereby compromising the efficacy of subsequent dosing with lower-affinity Abs (Bien-Ly et al., 2014). Overall, these findings indicate that high-affinity binding to TfR1 alters its intracellular fate, ultimately limiting its ability to mediate transcytosis across the BBB. Consistently, high-affinity anti-TfR Abs have been shown to bind efficiently to brain endothelial cells but tend to remain trapped in the CNS vasculature, limiting their release and accumulation in the brain parenchyma (Yu et al., 2011). These findings highlight the need to carefully optimize ligand density and affinity to align nanocarrier design with receptor trafficking dynamics, thereby maximizing transcytosis efficiency and effective delivery.

2.8 Transferrin

Tf, the endogenous iron-transporting glycoprotein, has been one of the most widely employed ligands for NPs functionalization to achieve receptor-mediated targeting through TfR1. Tf-conjugated NPs have been explored for both oncological and central nervous system applications (Qian et al., 2002; Yu et al., 2013). Early studies demonstrated that Tf-modified liposomes improved the uptake of anticancer drugs such as doxorubicin and docetaxel in tumor cell lines and enhanced therapeutic efficacy in xenograft models (Gupta et al., 2007; Li et al., 2011). Additionally, Tf-functionalized systems have been employed to facilitate BBB crossing. For instance, Tf-decorated liposomes and solid LNPs have shown increased delivery of neuroprotective agents, including curcumin and quercetin, to the brain in models of Alzheimer's disease (Meng et al., 2011; Zhao et al., 2011). Despite these advantages, the application of Tf itself as a targeting ligand is not without limitations.

Competition with endogenous Tf, steric hindrance, and potential saturation of TfR1 can reduce delivery efficiency, which has motivated the development of alternative ligands such as peptides and monoclonal Abs that retain receptor affinity but minimize interference with physiological Tf binding (Liang et al., 2018; Oh et al., 2009). Nevertheless, Tf remains a valuable proof-of-concept ligand that has paved the way for receptor-mediated NP targeting strategies.

2.9 Peptides

The peptides HAIYPRH (T7) and THRPPMWSPVWP (Tfr-T12), originally described by Lee et al. (2001) and Li et al. (2015), respectively, have been identified as potential ligands for TfR1–targeted drug delivery systems. Compared to native Tf, these peptides offer several advantages: i) they present limited interference with the physiological functions of the endogenous protein, ii) they reduce steric hindrance issues related to transferrin's large molecular size, and iii) they exhibit greater chemical and biological stability (Vikas et al., 2022).

Both peptides display high binding affinity toward TfR1, with dissociation constants (Kd) in the nanomolar range: approximately 10 nM for T7 (Oh et al., 2009; Aronson et al., 2021) and 15 nM for T12 (Lee et al., 2001). A crucial aspect for brain-targeted drug delivery is the ability to cross the BBB, which represents the main obstacle to drug distribution in the CNS. In this regard, Piantino et al evaluated the trans endothelial permeability of T7 and T12 using an in vitro model of human induced pluripotent stem cell-derived brain microvascular endothelial cells (hiPSC-BMECs) (Piantino et al., 2022).

Their findings showed that the T7 peptide exhibits significantly higher permeability across the in vitro BBB model compared to T12, suggesting greater efficiency in TfR1-mediated binding and intracellular transport leading to transcytosis. These results support the use of T7 as a promising targeting ligand for brain-directed drug delivery strategies, potentially enhancing the selectivity and efficacy of treatments for neurodegenerative diseases and brain tumors. Additional studies have confirmed that T7 binds to a specific site of the TfR1 that does not compete with endogenous Tf (Han et al., 2010; Wang et al., 2015). T7 has been employed to functionalize a variety of nanocarriers for oncological applications. Wang and Sun developed sorafenib-loaded nanoliposomes functionalized with T7 (T7-SNF-NLPs) and demonstrated their superior performance over untargeted formulations (Wang and Sun, 2020).

In vitro, T7-SNF-NLPs showed significantly improved uptake, apoptosis induction, and cytotoxicity in RKO colorectal cancer cells. In vivo, in xenografted mice, treatment with T7-SNF-NLPs led to marked tumor growth suppression and a significant reduction in Ki-67 expression, confirming their enhanced antiproliferative activity.

In ovarian cancer, paclitaxel-loaded T7-liposomes displayed enhanced cytotoxicity compared with non-targeted formulations (Wang and Sun, 2020). In glioma models, doxorubicin liposomes co-modified with TAT and T7 exhibited improved therapeutic efficacy and tumor inhibition (Zong et al., 2014). Furthermore, T7-conjugated low-density lipoprotein particles facilitated improved BBB penetration and significantly potentiated glioma therapy (Liang et al., 2018).

2.10 Antibodies

Monoclonal antibodies (mAbs) have been extensively investigated as targeting ligands in nanomedicine owing to their high specificity, strong binding affinity, and well-characterized pharmacology. By recognizing receptors selectively overexpressed in specific tissues or pathological conditions, mAbs can direct nanocarriers and Ab–drug conjugates to defined targets, thereby enhancing therapeutic efficacy while minimizing off-target toxicity (Scott et al., 2012). Among the most widely studied receptors for antibody-mediated drug targeting is TfR1. The rat monoclonal Ab OX26 was one of the first to be applied in TfR-mediated brain delivery by demonstrating that OX26-functionalized immunoliposomes strongly bound and were internalized into brain endothelial cells in vitro and accumulated along cerebral microvessels in vivo (Johnsen et al., 2018).

However, this association did not translate into efficient transcytosis across the BBB. Instead, OX26 primarily enhanced drug exposure through localized cargo release within endothelial cells. The 8D3 Ab, a mouse-specific anti-TfR1 IgG2a, has also been widely used in preclinical CNS delivery. In this context, 8D3 has been used both as a targeting ligand for NPs-based systems and as a binding domain within engineered antibody constructs to facilitate transport across the BBB, resulting in robust brain uptake in mouse models. Interestingly, optimization of affinity proved crucial: lowering 8D3 binding strength increased transcytosis efficiency, whereas very tight binding caused endothelial retention (Yu et al., 2011; Niewoehner et al., 2014). These findings are consistent with the broader concept that efficient TfR-mediated transcytosis requires a balance between affinity and valency. Excessively high-affinity or bivalent interactions tend to promote receptor clustering and lysosomal routing, whereas intermediate affinity and monovalent binding favor more efficient transcytosis (Bonvicini et al., 2025). Studies using monovalent anti-TfR1 antibodies with reduced affinity have demonstrated improved BBB transcytosis and increased brain accumulation (Bien-Ly et al., 2014; Weber et al., 2018). A possible explanation lies in altered intracellular trafficking: lower-affinity anti-TfR1 antibodies are less prone to lysosomal sorting and degradation, whereas high-affinity antibodies tend to accumulate in lysosomes, promoting receptor degradation and endothelial retention (Arguello et al., 2022).

These studies highlight 8D3 as a valuable tool to dissect how Ab affinity shapes TfR1-mediated transport. Another well-characterized clone is RI7217, which significantly enhanced liposomal uptake in brain endothelium. In comparative experiments, RI7217-conjugated liposomes showed nearly double the uptake compared with Tf-conjugated as observed in brain capillaries isolated 12 hours post-injection (Van Rooy et al., 2011). Consistent results were reported in both rats (Gosk et al., 2004; Johnsen et al., 2019) and mice (Johnsen and Moos, 2016; Paris-Robidas et al., 2016), confirming the strong tendency of high-affinity anti-TfR1 Abs to drive preferential accumulation in brain endothelial cells. While Abs such as OX26, 8D3, and RI7217 achieve strong endothelial binding and uptake, delivery mechanisms often rely on endothelial accumulation and localized release rather than efficient transcytosis. Nonetheless, the extensive body of work clearly establishes anti-TfR1 mAbs as valuable ligands that have paved the way for the development of smaller alternatives, including Ab fragments and peptides, with the aim of improving BBB penetration and therapeutic delivery. In addition to full-length Ab, Ab fragments have been engineered to target TfR1. De la Rosa et al. demonstrated that monovalent, low-affinity anti-TfR1 scFv variants achieve significantly improved brain delivery compared with high-affinity counterparts (De la Rosa et al., 2024). By reducing binding strength, these engineered fragments avoid excessive TfR1 clustering and lysosomal routing, limitations commonly observed with full-length antibodies, thereby promoting more efficient transcytosis. This highlights how affinity-tuned antibody fragments can outperform conventional mAbs in exploiting TfR1-mediated transport pathways.

2.11 Nanobodies

mAbs are among the most extensively studied targeting ligands in nanomedicine, and several Ab-targeted nanoparticles have advanced to clinical trials (Pearce and O'Reilly, 2019). However, full-length mAbs are limited by high production costs (Goswami et al., 2013) and potential immunological risks, even when fully humanized (Vaisman-Mentesh et al., 2020), while Ab fragments often exhibit reduced affinity and stability (Bates and Power, 2019). The discovery of camelid heavy-chain-only Abs (Hamers-Casterman et al., 1993) led to the development of single-domain Abs, known as variable heavy domain of heavy chain (VHH) antibodies or nanobodies (Nbs). These Nbs, at a size of only ∼15 kDa, combine high stability, low immunogenicity, higher tissue penetration and resistance to pH and temperature fluctuations, making them highly attractive for precision targeting (Muyldermans, 2013). In vitro studies have consistently demonstrated that Nb functionalization enhances NP uptake and therapeutic efficacy compared with non-targeted systems (Altintas et al., 2013; Broekgaarden et al., 2016; Liu et al., 2020; Martínez-Jothar et al., 2019; Van der Meel et al., 2012).

The Dewilde group (Wouters et al., 2020; Wouters et al., 2022) identified two anti-TfR1 Nbs, Nb62, specific for the murine receptor, and Nb188, specific for the human receptor, both capable of crossing the BBB via receptor-mediated transcytosis and delivering biologically active therapeutic cargo to the brain. Using this system, the authors observed that Nbs with higher binding affinity exhibited reduced brain penetration, consistent with previous findings showing that high-affinity TfR-targeting antibodies are preferentially trafficked to lysosomes for degradation. A study by Rué and colleagues described two cross-reactive Nbs recognizing both human and cynomolgus TfR, enhancing brain delivery of an anti-BACE1 Ab and reducing cerebral Aβ1-40 levels by 40% in mice (Rué et al., 2023). Similarly, another group engineered a pH-sensitive murine anti-TfR Nb (M1, carrying R56H, P96H, Y102H mutations) that achieved >3.5% brain accumulation of the injected dose per gram of brain within 30 minutes, demonstrating rapid and efficient BBB transcytosis (Esparza et al., 2023). For comparison, full-length anti-TfR Abs typically reach only ∼0.01–0.1% ID/g, as reported in several studies using high-affinity or bivalent anti-TfR clones (Yu et al., 2011; Bien-Ly et al., 2014; Niewoehner et al., 2014). This puts the engineered nanobody over one to two orders of magnitude higher in brain delivery efficiency than conventional mAbs, highlighting the substantial advantage of small, monovalent TfR-targeting formats. Several reviews further highlight the versatility of Nb-based delivery systems for their use in cancer therapy (Hu et al., 2017) (Maksymova et al., 2025). See the summary in Table 2.4. Notably, in addition to camelid-derived VHHs, single-domain antibodies can also be obtained from cartilaginous fish such as sharks, where they are referred to as variable new antigen receptors (VNARs), representing an alternative class of nanobody-like molecules. They are smaller than VHHs, with a molecular weight of approximately 12 kDa. Due to their small size, VHHs and VNARs are promising for therapeutic, diagnostic, and delivery applications. Their compact nature also enables them to target hidden epitopes and supports the development of cross-species reactive single-domain Abs, unlike conventional IgGs (Pothin et al., 2020).

2.12 Q52c and R2 Nanobodies

In this thesis, liposomes were functionalized with the anti-TfR nanobody Q52c as the targeting ligand. In parallel, liposomes functionalized with the R2 nanobody were used as a negative-control formulation to distinguish TfR-specific interactions from non-specific effects associated with nanobody functionalization or liposome uptake. Q52c, also referred to as clone QTF-3B2, is a recombinant monoclonal VHH derived from Llama glama and directed against the human transferrin receptor/CD71. According to the supplier's product information, Q52c specifically recognizes human TfR/CD71 and does not compete with transferrin binding.

This feature is relevant for TfR-targeted delivery systems, as it may allow receptor recognition without directly interfering with the physiological transferrin–TfR interaction. Q52c has a molecular weight of approximately 15.5 kDa and is equipped with a C-terminal C-Direct tag containing an unpaired cysteine, which enables directional conjugation to carrier surfaces. This characteristic is particularly advantageous for liposome functionalization, since site-specific coupling may help preserve ligand accessibility and orientation on the nanocarrier surface. Although detailed structural, affinity, and epitope-mapping data for Q52c are not extensively available in public literature, the available product specifications support its use as a small, human TfR-specific, and site-specifically conjugable targeting ligand. Based on these characteristics, Q52c was used in this project to functionalize the surface of liposomes with the aim of promoting selective interaction with TfR-expressing cells. The R2 nanobody, raised against the azo dye Reactive Red 6 (RR6), is commonly used as an irrelevant negative control nanobody in targeting and imaging studies. In CAIX-targeted optical imaging, R2 was used to assess background uptake and non-specific signal (van Brussel et al., 2016). Likewise, in extracellular-vesicle targeting experiments, R2 served as a negative control because of its negligible affinity for EGFR (Kooijmans et al., 2018). It was also used as an irrelevant control in HER2 tyrosine-kinase binding and inhibition assays (Lamtha et al., 2021).

3

Materials and Methods

3.1 Materials for thin-film hydration liposomes production and nanobody functionalization

3.1.1 Lipids

- Dipalmitoyl-sn-glycero-3-phosphocholine (DPPC), Avanti Polar Lipids (Alabaster, AL, USA)
- 1,2-distearoyl-sn-glycero-3-phosphoethanolamine-N-[methoxy(polyethylene glycol)2000] (PEG-DSPE), Avanti Polar Lipids (Alabaster, AL, USA)
- Maleimide-PEG-DSPE, Avanti Polar Lipids (Alabaster, AL, USA)
- Cholesterol, Sigma-Aldrich (St. Louis, MO, USA)

3.1.2 Reagents and buffers

- 1,4-dithiothreitol (DTT), Sigma-Aldrich (St. Louis, MO, USA)
- Sodium chloride (NaCl), Sigma-Aldrich (St. Louis, MO, USA)
- Sodium phosphate monobasic dihydrate, Sigma-Aldrich (St. Louis, MO, USA)
- Ammonium molybdate tetrahydrate, Sigma-Aldrich (St. Louis, MO, USA)
- L-ascorbic acid, Sigma-Aldrich (St. Louis, MO, USA)
- Perchloric acid, Sigma-Aldrich (St. Louis, MO, USA)
- HEPES ($\geq$99.5%, buffer grade), Carl Roth GmbH + Co. KG (Karlsruhe, Germany)
- Tris(2-carboxyethyl) phosphine hydrochloride (TCEP), Thermo Fisher Scientific (Waltham, MA, USA)

3.1.3 Solvents

- Methanol, Sigma-Aldrich (Darmstadt, Germany)
- Ethanol, Sigma-Aldrich (Darmstadt, Germany)
- Milli-Q water, Millipore (Burlington, MA, USA)

3.1.4 Electrophoresis reagents

- Bolt 4–12% Bis-Tris gels (1.0 mm), Thermo Fisher Scientific (Waltham, MA, USA)
- Bolt MES SDS running buffer (20×), Thermo Fisher Scientific (Carlsbad, CA, USA)
- Coomassie Blue PageBlue protein staining solution, Thermo Fisher Scientific (Waltham, MA, USA)
- PageRuler prestained protein ladder, Thermo Fisher Scientific (Waltham, MA, USA)

3.1.5 Fluorescent probes

- DiD, Thermo Fisher Scientific (Burlington, ON, Canada)

3.1.6 Cell culture media and biological reagents

- Dulbecco's modified Eagle's medium (DMEM), Sigma-Aldrich (St. Louis, MO, USA)
- SupplementMix Endothelial Cell Growth Medium 2, PromoCell GmbH (Heidelberg, Germany)
- Fetal bovine serum (FBS; sterile filtered), Thermo Fisher Scientific (Waltham, MA, USA)
- Dulbecco's phosphate-buffered saline (PBS), Thermo Fisher Scientific (Waltham, MA, USA)
- Trypsin, Thermo Fisher Scientific (Waltham, MA, USA)

3.1.7 Antibodies and nanobodies

- APC mouse IgG1κ isotype control antibody, BD Biosciences ((San Jose, CA, USA)
- APC-conjugated anti-human CD71 monoclonal antibody (IgGκ, clone OKT9), eBioscience (Waltham, MA, USA)
- + Recombinant monoclonal VHH anti-human transferrin receptor (CD71, clone QTF-3B2, catalogue no. Q52c), QVQ (Utrecht, The Netherlands)

+ Recombinant monoclonal VHH nanobody R2, in-house produced according to a method published by Thomassen et al., 2002.

3.2 Materials for Super Somes liposome production

3.2.1 Lipids

- Phosphatidylcholine, Sigma-Aldrich, Merck Life Science S.r.l. (Milan, Italy)
- 1,2-distearoyl-sn-glycero-3-phosphoethanolamine-N-[methoxy (polyethylene glycol)-2000] (DSPE-PEG2000), Sigma-Aldrich, Merck Life Science S.r.l. (Milan, Italy)

3.2.2 Solvents

- Ethanol, Sigma-Aldrich, Carlo Erba Reagents (Milan, Italy)

3.2.3 Supercritical fluid

- CO_2, >99.4% purity) was purchased from Morlando Group Srl (Naples, Italy)

3.3 Preparation of liposomes by conventional thin-film hydration

Liposomes used for nanobody functionalization and in vitro uptake studies were prepared by the conventional thin-film hydration method. Two main types of formulations were produced: non-targeted liposomes, used as control formulations, and maleimide-containing liposomes, subsequently functionalized with Q52c or R2 nanobodies.

3.3.1 Preparation of non-targeted liposomes

Non-targeted liposomes (NTLs) were prepared using dipalmitoyl-sn-glycero-3 phosphocholine (DPPC), cholesterol, and PEG-(2000)-DSPE at a molar ratio of 1.85:1:0.15. A detailed overview of the lipid composition is provided in Table 3.1. PEG-(2000)-DSPE was included at 0.15 molar equivalents, and no MAL-PEG-(2000)-DSPE was added to the formulation. Liposomes were prepared using the conventional lipid film hydration method (Figure 3.1). Briefly, individual lipids were accurately weighed according to the predefined molar ratios and transferred to a 100 mL round-bottom flask. Lipids were subsequently dissolved in a chloroform: methanol mixture (2:1, v/v) and DiD was added to the organic phase at 0.2 mol% relative to the total lipid content. The resulting lipid solution was gently mixed to ensure homogeneous distribution of all components. Organic solvents were evaporated using a rotary evaporator at 40°C, followed by drying under a nitrogen stream for 45 minutes, leading to the formation of a thin lipid film on the inner surface of the flask. Complete removal of residual solvents was ensured prior to hydration. The dried lipid film was hydrated with 6 mL of physiological buffer (0.8% (w/v) NaCl, 10 mM HEPES, pH 7.4), resulting in a final lipid concentration of 10 mM. Hydration was performed under gentle agitation at 40°C. To reduce vesicle size and obtain a controlled size distribution, liposomes were sequentially extruded through polycarbonate membranes of decreasing pore size using a thermobarrel Lipex extruder (Northern Lipids, Burnaby, BC, Canada). The extrusion steps were performed as follows:

1. 400/100 nm membranes (3 passes)
2. 200/200 nm membranes (5 passes)
3. 200/100 nm membranes (10 passes)
4. 100/100 nm membranes (10 passes)
5. 50/100 nm membranes (5 passes)

Multiple extrusion cycles were performed at each pore size to ensure uniform vesicle formation. The final liposome suspension was collected and stored at 4°C until further characterization and use.

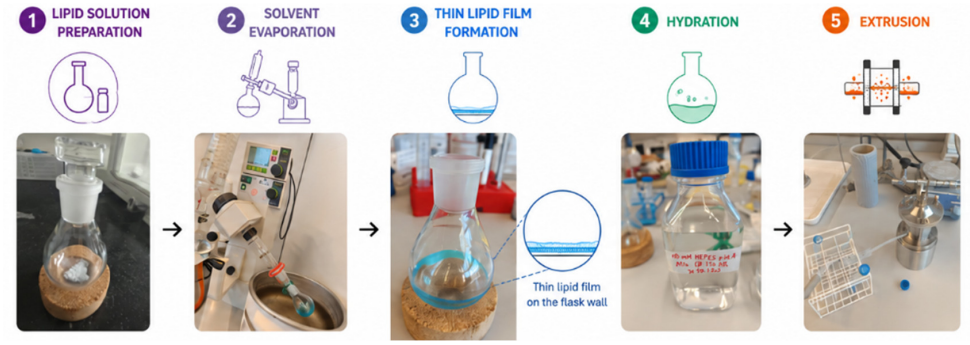


Figure 3.1: Main steps of the lipid film hydration method followed by extrusion.

Untargeted liposomes		
Lipids	**%**	**Molar ratio**
DPPC	58	1.85
PEG (2000)-DSPE	5	0.15
Cholesterol	31	1
DiD labeling (stock:200µg/ml)	6	0.2
BUFFER: 0.8% (w/v) NaCl. 10mM HEPES (pH 7.4)		

Table 3.1: Lipid composition of untargeted liposomes with corresponding percentages and molar ratios.

3.3.2 Preparation of Q52c- and R2-conjugated liposomes

Targeted liposomes were prepared by the lipid film hydration method as described below. Briefly, a single lipid batch (6 mL, total lipid concentration 10 mM) was prepared and subsequently divided into two aliquots for nanobody conjugation. One aliquot was functionalized with Q52c (TfR1-targeting nanobody), while the other was functionalized with R2, used as a non-targeting control.

For targeted formulations, the lipid composition consisted of DPPC, cholesterol, PEG-(2000)-DSPE, and MAL-PEG-(2000)-DSPE at a molar ratio of 1.85:1:0.075:0.075. PEG-(2000)-DSPE and MAL-PEG-(2000)-DSPE were included at 0.075 molar equivalents each to enable subsequent surface conjugation via maleimide chemistry. Fluorescently labeled liposomes were obtained by incorporating 0.2 mol% of 18:0 DiD at the expense of DPPC. A detailed overview of the lipid composition is provided in Table 3.2.

Targeted liposomes		
Lipids	**%**	**Molar ratio**
DPPC	62	1.85
PEG (2000)-DSPE	2.5	0.075
Maleimide-PEG(2000)-DSPE	2.5	0.075
Cholesterol	33	1
DiD labeling (stock:200µg/ml)	0.07	0.2

Table 3.2: Lipid composition of targeted liposomes with corresponding percentages and molar ratios.

Following lipid film formation and hydration, performed as described above for NTLs, liposomes were sequentially extruded through 400/100 nm polycarbonate membranes (3×), 200/200 nm membranes (5×), 200/100 nm membranes (10×), 100/100 nm membranes (10×), and 50/100 nm membranes (5×) using a 10-mL thermobarrel Lipex extruder (Northern Lipids, Burnaby, BC, Canada). After extrusion, the liposome suspension was divided into two aliquots for nanobody conjugation, corresponding to 1.85 mL for Q52c and 1.25 mL for R2.

3.3.3 Nanobody reduction and conjugation to liposomes

For the conjugation of Q52c and R2 nanobodies onto the liposome surface, nanobodies (Q52c and R2) were reduced with TCEP (500 mM stock) at a nanobody:TCEP molar ratio of 1:200. A total of 292 µg Q52c and 212 µg R2 were incubated with TCEP for 5 min at room temperature. Following reduction, samples were desalted using Zeba spin desalting columns (7 kDa MWCO, Thermo Scientific) and buffer-exchanged into 0.8% (w/v) NaCl, 10 mM HEPES (pH 7.4) to remove excess TCEP.
Reduced nanobodies were subsequently mixed with liposomes at a molar ratio of 1:50 (Nb:MAL-PEG-DSPE) and incubated overnight at 4 °C under gentle agitation to allow surface conjugation. Unconjugated nanobodies were removed by centrifugal filtration at 2000 × g for 1 h, followed by a second centrifugation at 2000 × g for 40 min using Vivaspin centrifugal filter units (300,000 MWCO, Sartorius). Prior to sample loading, Vivaspin units were pre-washed with 2 mL of 0.8% (w/v) NaCl, 10 mM HEPES (pH 7.4) and centrifuged at 4000 × g for 5 min at 4 °C, according to the manufacturer's instructions.

3.3.4 Purification of nanobody-functionalized liposomes

For purification, a total of four Vivaspin centrifugal filter units were prepared: two for Q52c-conjugated liposomes and two for R2-conjugated liposomes, as each Vivaspin device has a maximum loading capacity of 2 mL. Specifically, 975 µL of Q52c-liposome suspension were combined with 975 µL of 0.8% (w/v) NaCl, 10 mM HEPES (pH 7.4) per Vivaspin unit, corresponding to an initial volume of 1.95 mL.

Similarly, 690 µL of R2-conjugated liposomes were mixed with an equal volume of buffer per Vivaspin unit, corresponding to an initial volume of 1.38 mL. Following centrifugal purification, liposome suspensions were brought back to their original volumes using the same buffer to ensure comparable final concentrations between formulations (Figure 3.2).

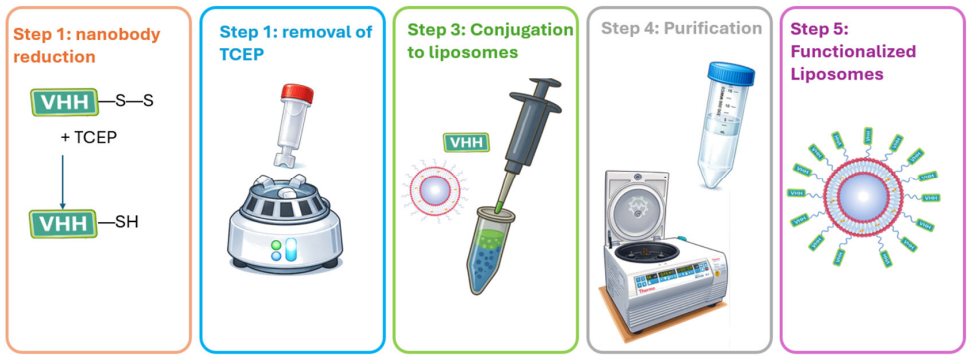


Figure 3.2: Main steps of the direct thiol-maleimide conjugation of nanobodies to liposomes.

3.4 Physicochemical characterization of thin-film hydration liposomes

Following preparation and purification, non-targeted and nanobody-functionalized liposomes were subjected to physicochemical characterization before use in cellular studies. The analyses described below assessed hydrodynamic diameter, size distribution, zeta potential, and lipid concentration, providing a basis for comparing the formulations and interpreting subsequent uptake experiments.

3.4.1 Dynamic light scattering and Zeta potential analysis

The hydrodynamic diameter and polydispersity index (PDI) of non-targeted and nanobody-conjugated liposomes were determined by dynamic light scattering (DLS) using a ZetaSizer Nano S (Malvern Instruments, Malvern, UK) at a fixed scattering angle of 173°. For size measurements, liposome suspensions were diluted 100× in physiological buffers containing 10 mM HEPES and 0.8% (w/v) NaCl (pH 7.4). Measurements were performed at room temperature, and each sample was analyzed in triplicate.

Zeta potential measurements were carried out using a ZetaSizer Nano Z (Malvern Instruments). For these analyses, liposomes were diluted 17× in 10 mM HEPES buffer (pH 7.4) without NaCl. All measurements were performed at room temperature. Mean particle size, PDI, and zeta potential values were obtained using Zetasizer software and are reported as mean ± standard deviation.

3.4.2 Determination of total lipid concentration by inorganic phosphate assay

Total lipid concentration of non-targeted and nanobody-conjugated liposomes was determined using the inorganic phosphate assay according to Rouser et al. A phosphate calibration curve was prepared in triplicate using a 0.5 mM sodium phosphate monobasic standard solution, obtained by 100-fold dilution of a 50 mM stock solution. Serial dilutions corresponding to 0–140 nmol inorganic phosphate per sample were prepared and processed in parallel with liposome samples. Liposome samples (non-targeted, Q52c-conjugated, and R2-conjugated formulations) were analyzed in triplicate. Different sample volumes were used depending on lipid concentration to fall within the linear range of the calibration curve. Assuming an initial lipid concentration of 10 mM, a nominal volume of 10 µL would correspond to approximately 100 nmol lipid; however, due to lipid loss during extrusion and purification, different volumes were required. Samples were placed in a block heater at 180 °C for 45 min to evaporate solvent. After cooling to room temperature, 300 µL of perchloric acid ($HClO_4$) was added to each tube to digest phospholipids and release inorganic phosphate. Tubes were then covered with glass marbles to prevent evaporation and incubated in a block heater at 180 °C for 2 h. Following digestion, samples were allowed to cool to room temperature, after which 1 mL of Milli-Q water, 500 µL of 1.2% (w/v) ammonium molybdate solution, and 500 µL of L-ascorbic acid solution were added sequentially to each tube to allow formation of the phosphomolybdate complex. Samples were subsequently incubated in a boiling water bath for 5 min to promote color development, followed by cooling to room temperature. Absorbance was then measured at 797 nm using a spectrophotometer. A phosphate standard curve was generated in Microsoft Excel, and inorganic phosphate concentrations of the samples were calculated accordingly. Total lipid concentrations were derived based on the phosphate content, assuming complete hydrolysis of phospholipids.

3.5 SDS-PAGE analysis of nanobody-conjugated liposomes

To confirm successful conjugation of Q52c and R2 nanobodies to the liposomal surface, sodium dodecyl sulfate–polyacrylamide gel electrophoresis (SDS–PAGE, Figure 3.3) was performed. For each condition, Q52c- and R2-conjugated liposomes were mixed with 4× Laemmli sample buffer supplemented with DTT (final concentration 400 mM) and diluted with PBS to a final volume of 40 µL. In parallel, free Q52c and R2 nanobodies were processed under the same conditions and used as positive controls. Untargeted liposomes were included as negative controls. In addition, Q52c- and R2-conjugated liposomes were analyzed both before and after purification with Vivaspin centrifugal filter units to assess the removal of unbound nanobody.
All samples were incubated at 95 °C for 10 min to ensure complete protein denaturation. After cooling to room temperature, samples were loaded onto precast Bolt 4–12% Bis-Tris Plus polyacrylamide gels (1.0 mm, 10 wells; Invitrogen, Thermo Scientific). Electrophoresis was performed at a constant voltage of 160 V for 40 min using 1× MES running buffer. Following separation, gels were stained with Coomassie Blue (PageBlue protein staining solution) for 1 h to visualize protein bands and subsequently destained in distilled water for 1 h. Gel images were acquired using a ChemiDoc Imaging System (Bio-Rad, Hercules, CA, USA). The presence of nanobody bands at the expected molecular weight in purified liposome samples, together with the absence of such bands in untargeted liposomes and the reduction of free nanobody signal after purification, was used as qualitative confirmation of successful surface conjugation.

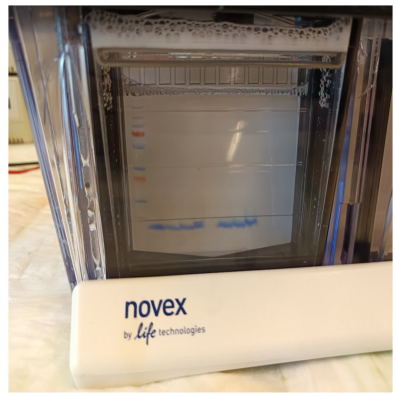


Figure 3.3: Gel electrophoresis system (Novex™, Life Technologies) used for protein separation by SDS-PAGE. The image shows the electrophoresis tank containing precast gel cassettes and running buffer, employed for the analysis of protein profiles in the examined samples.

3.6 Detection of TfR1 expression levels by flow cytometry

Surface expression of TfR1 was evaluated by flow cytometry in HEK293T, MCF7, A549, hBMEC, hCMEC/D3, and TMNK-1 cells. Cells were washed with phosphate-buffered saline (PBS) and detached using ReLeSR at 37 °C for 5 min. After neutralization with complete culture medium, cells were gently resuspended and centrifuged at 300 × g for 5 min at room temperature. The resulting cell pellets were resuspended in culture medium and counted using an automated cell counter. Cells were subsequently adjusted to a concentration of 4×10^5 cells/mL, and 1×10^5 cells were aliquoted per sample in PBS supplemented with 1% fetal calf serum (FCS) to minimize nonspecific binding. Cells were incubated with APC-conjugated anti-human CD71 monoclonal antibody (mouse IgGκ, clone OKT9; eBioscience) at a 1:50 dilution. All samples were prepared in duplicate.

APC-conjugated IgG isotype antibody at the same dilution (1:50) was used as an isotype control to account for nonspecific antibody binding, while unstained cells were included to determine background autofluorescence. Samples were incubated for 30 min at 4 °C in the dark under gentle agitation.

Following incubation, cells were centrifuged at 300 × g for 5 min and washed once with 500 µL PBS supplemented with 1% FCS to remove unbound antibody. After a second centrifugation step, cell pellets were resuspended in 200 µL PBS + 1% FCS for analysis. All samples were transferred to a flat-bottom 96-well plate for flow cytometric analysis using FACSCanto II (BD Biosciences). Instrument settings are summarized in Table 3.3. Forward scatter (FSC) and side scatter (SSC) parameters were used to define the main cell population (P1), followed by identification of APC-positive cells (P2). At least 10,000 events were acquired within the defined gate for each sample. APC fluorescence was detected in the appropriate channel, and both the mean fluorescence intensity (MFI; APC, P1) and the percentage of APC-positive cells (%P2) were determined for each sample.

Parameters	**Setting**
FSC	70 (log)
SSC	200 (log)
APC	440 (log)

Table 3.3: Instrument settings used for flow cytometry analysis.

Voltage settings applied for forward scatter (FSC), side scatter (SSC), and APC fluorescence detection during acquisition on the FACSCanto II flow cytometer. All parameters were recorded using logarithmic (log) amplification.

3.7 Static cellular uptake study

One day prior to the experiment, cells were detached by trypsin, counted, and resuspended at a final concentration of 1×10^5 cells/mL. Subsequently, 500 µL of cell suspension per well was seeded into 24-well plates (Figure 3.4). On the following day, the culture medium was removed and replaced with 500 µL of fresh medium, specific for each cell line:

- DMEM supplemented with 10% FCS for MCF7 and A549 cells
- EBM-2 medium for hCMEC/D3 cells

Subsequently, liposome samples were added to each well at a final concentration of 100 µM total lipids (TL) per well. For each cell line, the following experimental conditions were included:

- Untreated control (cells only)
- Untargeted DiD-labeled liposomes
- Q52c-targeted DiD-labeled liposomes
- R2-targeted DiD-labeled liposomes

Liposomes were incubated with the cells at 37°C and 5% CO2 conditions for 4h. Following incubation, the culture medium containing liposomes was removed, and the cells were washed with phosphate-buffered saline (PBS) to eliminate unbound nanoparticles. Cells were then detached using 100 µL of trypsin per well, and 400 µL of complete culture medium was added to neutralize the trypsin. The resulting cell suspensions were transferred to 1.5 mL microcentrifuge (Eppendorf) tubes and centrifuged at 300 × g for 5 minutes. The supernatant was carefully discarded, and cell pellets were resuspended in 200 µL of PBS supplemented with 1% fetal calf serum (FCS) for subsequent analysis. Flow cytometric analysis was performed as described for the previous experiment. Samples were analyzed using a FACSCanto II (BD Biosciences), applying the same instrument settings reported in Table 3.3.

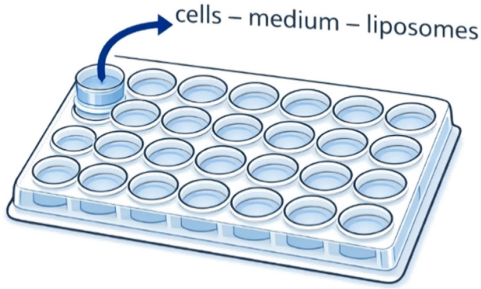


Figure 3.4: Static cellular uptake performed in 24-well plates.

3.8 Dynamic cellular uptake study under perfusion conditions

To better mimic physiological conditions, uptake studies were performed under flow using an Ibidi µ-Slide system (Ibidi, Germany; Figure 3.5), a microfluidic platform specifically designed to reproduce vascular-like shear stress in vitro. The system is based on polymeric channel slides with defined geometries that allow precise calculation and control of shear stress as a function of flow rate, channel dimensions, and medium viscosity. Cells are seeded within a narrow microfluidic channel featuring an optically transparent coverslip bottom, which supports high-resolution imaging and the formation of a homogeneous cell monolayer. After attachment, the slide is connected via Luer adapters to a closed-loop perfusion circuit driven by a computer-controlled pump. This setup enables continuous perfusion of culture medium under a unidirectional, laminar flow regime, closely resembling physiological blood flow conditions.

Importantly, the laminar nature of the flow ensures a well-defined and uniform shear stress distribution across the cell surface, minimizing turbulence and flow-induced variability. The absence of oscillatory components allows the application of steady shear stress, which is particularly relevant for modeling venue or capillary environments. In addition to mechanical stimulation, the continuous flow provides constant nutrient supply, efficient gas exchange, and removal of metabolic waste products, thereby supporting long-term cell culture under dynamic conditions. The system is fully compatible with standard incubators and live-cell imaging platforms, enabling real-time monitoring of cellular responses to shear stress. Furthermore, the modular design allows easy adjustment of experimental parameters such as flow rate, shear stress, and medium composition.

Perfusion experiments were conducted using hCMEC/D3 cells, an established in vitro model of the BBB. Cells were harvested and resuspended at a concentration of 1.6 $\times$ 10^6 cells/mL. A volume of 150 µL of cell suspension was seeded into pre-coated (fibronectin and collagen IV) 0.6 Luer chambers (Ibidi) and incubated at 37°C and 5% CO_2 for 30 minutes to allow cell attachment. Subsequently, 60 µL of complete EBM-2 medium was added to each chamber, and cells were allowed to attach for an additional 2 hours before connection to the perfusion system, which was filled with approximately 14 mL of complete EBM-2 medium.
Cells were cultured under continuous flow conditions at a shear rate of 300 s^{-1} for 3 days at 37°C and 5% CO_2. After 3 days, 10 mL of medium in the perfusion reservoir was replaced with fresh complete EBM-2 medium.

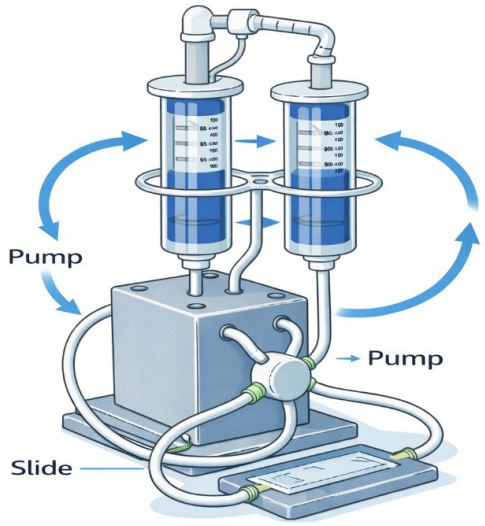


Figure 3.5: Schematic of the Ibidi µ-Slide perfusion system is used to expose cells cultured in a slide-like chamber to continuous unidirectional flow generated by a pump system.

Liposome formulations were then introduced into four different microfluidic systems (Figure 3.6) under flow conditions as follows:

- Control (no liposomes)
- Untargeted DiD-labeled liposomes (0.1 mM final concentration)
- Q52c-targeted DiD-labeled liposomes (0.1 mM final concentration)
- R2-targeted DiD-labeled liposomes (0.1 mM final concentration)

Samples were incubated under flow (300 s^{-1} shear rate) for 4 hours at 37°C and 5% CO_2.
Following incubation, perfusion was stopped and chambers were disconnected. Chambers were washed with 1 mL of medium and subsequently fixed with 1 mL of formalin.

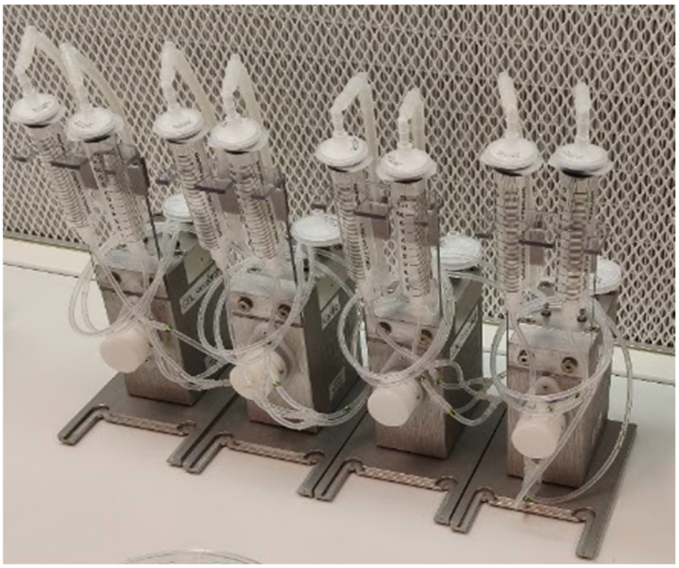


Figure 3.6: Four parallel microfluidic systems used for dynamic uptake experiments under flow conditions, comparing untreated controls with untargeted, Q52c-targeted, and R2-targeted DiD-labeled liposomes.

Samples were stored overnight at 4°C in the dark. The following day, chambers were washed twice with 1 mL of supplemented EBM-2 medium. Cells were stained with a solution containing Hoechst 33342 (1 µg/mL; nuclear staining) and phalloidin-Alexa Fluor 488 (1:50 dilution in DPBS; actin staining) and incubated for 30 min at room temperature. Chambers were then washed once more with 1 mL of supplemented medium. The medium was removed, and samples were mounted using FluoSave mounting medium before fluorescence microscopy analysis.

Images were acquired using a Zeiss Observer Z1 microscope equipped with a Colibri light source containing 365, 470, and 625 nm LEDs, Zeiss filter sets 49, 10, and 50, a Zeiss AxioCam MRm camera, and a Zeiss Fluar 40×/1.30 oil objective (Figure 3.7). These settings were used to visualize Hoechst, phalloidin-Alexa Fluor 488, and Cy5 signals, respectively. Image acquisition was performed using ZEN 2 software with the Z-stack module, while image analysis was carried out using ZEN 3.12 software with the deconvolution and analysis modules.

For each sample, fluorescence Z-stacks were acquired with a spacing of 0.27 µm between consecutive optical sections. Maximum-intensity projections were generated from the Z-stacks for particle quantification. Deconvolution was applied to the acquired image stacks to reduce out-of-focus fluorescence and improve image sharpness, using a strength of 0.9, a blur radius of 15, and a sharpness value of 0.0. For qualitative assessment of liposome localization, deconvolved Z-stacks were used to generate orthogonal projections and three-dimensional reconstructions.

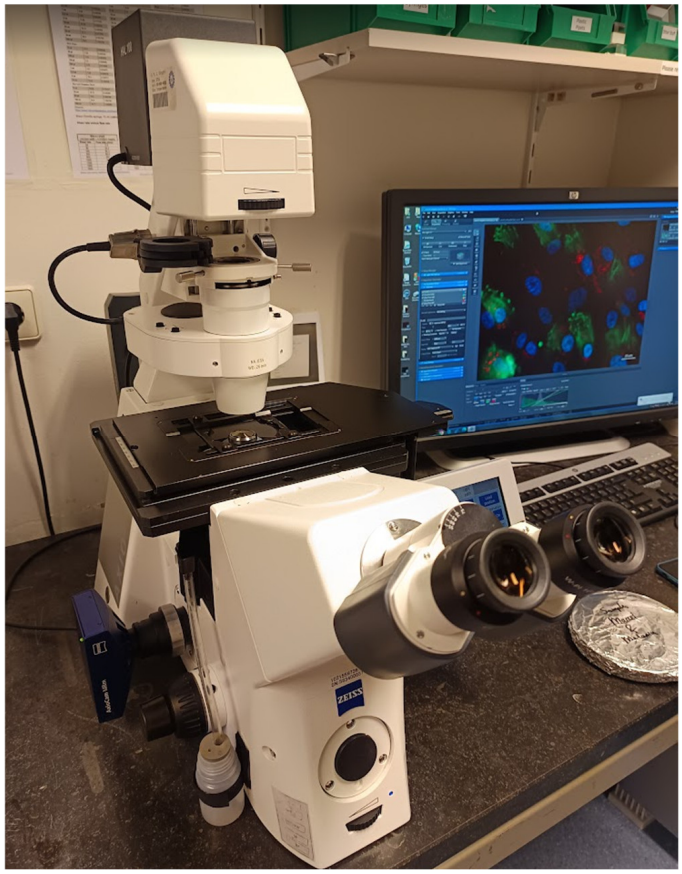


Figure 3.7: Zeiss Observer Z1 fluorescence microscope used for image acquisition.

Orthogonal projections were generated in the X–Y, X–Z, and Y–Z planes, allowing visualization of the fluorescent signal from the top and from two lateral perspectives along the Z-axis. The X–Z and Y–Z views were obtained from the positions indicated in the corresponding X–Y image. Three-dimensional reconstructions were generated from the complete deconvolved Z-stack by volumetric rendering and were visualized at different rotation angles to evaluate the overall spatial distribution of the DiD-labelled liposomes relative to the cellular structures. For quantitative analysis, the resulting images were analysed using the analysis module. Automatic segmentation was performed by applying a global threshold to the DiD signal, allowing the selection, counting, and measurement of fluorescent particle area.

3.9 Preparation and characterization of Super Somes liposomes by supercritical CO_2-assisted technology

Since Super Somes liposomes were not intended for nanobody functionalization or cellular uptake studies, their preparation and characterization are described in a separate section. This part of the work was conceived as a preliminary manufacturing-oriented study aimed at exploring supercritical CO_2-assisted production as a scalable approach for non-functionalized liposomes.

3.9.1 Supercritical CO_2-assisted production of non-functionalized liposomes

Non-functionalized liposomes were produced using a continuous supercritical CO_2-assisted process, referred to as Super Somes. The process was performed using phosphatidylcholine as the lipid component, ethanol as the organic solvent, distilled water as the aqueous phase, and CO_2 as the supercritical fluid. Experiments were carried out using different amounts of phosphatidylcholine, namely 125 mg, 250 mg, and 500 mg. For each production test, phosphatidylcholine was dissolved in 100 mL of ethanol, while 200 mL of distilled water was used as the aqueous phase.
The operating conditions were selected based on previous successful experiments performed by the research group. Briefly, the process was carried out using an injector diameter of 80 µm, a formation chamber pressure of 100 bar, a chamber temperature of 40 °C, a saturator temperature of 40 °C, a resistance temperature of 30 °C, and a separator temperature of 25 °C. The CO_2 flow rate was set at 7.505 g/min, the ethanol flow rate at 3.5 mL/min, and the water flow rate at 7 mL/min, corresponding to a gas-to-lipid ratio of 2.72.
During the process, the ethanol–phospholipid solution, CO_2, and water were continuously fed into the Super Somes system. The selected operating point was located within the miscibility gap of the ethanol–CO_2–water ternary system, a region in which the three components are not fully miscible. This phase separation is relevant for liposome formation, as it promotes atomization of the aqueous phase and the subsequent self-assembly of phospholipids around the generated water droplets, leading to the formation of vesicular structures.

3.9.2 Post-insertion PEGylation

A fraction of the produced Super Somes liposomes was subjected to post-insertion PEGylation using DSPE-mPEG2000, with the aim of obtaining stealth liposomes. The liposomal suspension was preheated to 45 °C under magnetic stirring (Figure 3.8). DSPE-mPEG2000 was then added to the suspension, and the system was maintained under stirring at 100 rpm for 2 h. According to the experimental documentation, PEGylation was performed using DSPE-mPEG2000 at 1.5% w/w, corresponding to 0.14 mg, under the same temperature and stirring conditions.

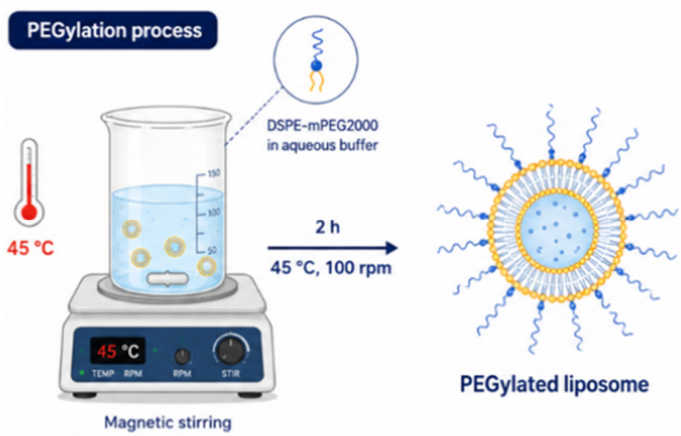


Figure 3.8: Post-insertion PEGylation of liposomes.

After PEGylation, the sample was kept at room temperature for 30 min before storage at 4 °C. This step was performed to promote the insertion of PEGylated lipid chains into the phospholipid bilayer and to limit flip-flop phenomena, which are kinetically disfavored at low temperature.

3.9.3 Dynamic light scattering and Zeta potential analysis

Super Somes liposomes were characterized in terms of mean hydrodynamic diameter, polydispersity index, and Zeta potential by dynamic light scattering. Measurements were performed on both non-PEGylated and PEGylated Super Somes liposomes to evaluate the effect of post-insertion PEGylation on particle size distribution and surface charge. For the preliminary production screening, liposome suspensions obtained using different amounts of phosphatidylcholine were analyzed to identify the formulation with the most suitable nanoscale dimensions and size distribution. All measurements were performed in triplicate. The PEGylated formulation was analyzed 24 h after post-insertion PEGylation to assess changes in mean hydrodynamic diameter, PDI, and Zeta potential after DSPE-mPEG2000 insertion.

3.9.4 Scanning Electron Microscopy (SEM) analysis

The morphology of the liposomal formulations was examined using a field-emission scanning electron microscope (FE-SEM; Supra 35, Carl Zeiss, Germany). For sample preparation, 30 µL of liposomal suspension was deposited onto a clean glass substrate and allowed air-dry at room temperature, forming a thin film.
Before imaging, the dried samples were sputter-coated with a thin gold layer to improve surface conductivity and minimize charging effects during SEM analysis. Gold coating was performed using an Agar Auto Sputter Coater (model 108 A; Stansted, United Kingdom) at a current of 40 mA for 180 s. SEM images were acquired to evaluate liposome morphology, particle dispersion, surface appearance, and the presence of possible aggregates.

3.9.5 Stability evaluation over time

Storage stability of non-PEGylated and PEGylated Super Somes liposomes was evaluated over time. Samples were stored at 4 °C and reanalyzed by dynamic light scattering at predefined time points to monitor possible variations in mean hydrodynamic diameter, polydispersity index, and ζ-potential. Non-PEGylated Super Somes liposomes were analyzed immediately after production and after 15 and 30 days of storage. PEGylated Super Somes liposomes were analyzed 24 h after post-insertion PEGylation and subsequently after 7, 15, and 30 days of storage. This analysis was performed to assess whether post-insertion PEGylation affected the colloidal stability of Super Somes liposomes during storage.

4

Results

In this work, liposome development was pursued through two complementary production approaches. First, non-functionalized liposomes were prepared using supercritical CO_2-assisted technology (Super Somes), with the aim of exploring a solvent-free, scalable method suitable for green mass production. In parallel, nanobody-functionalized liposomes were produced by conventional thin-film hydration, which allowed the preparation of targeted formulations required for in vitro biological evaluation. This strategy enabled the simultaneous investigation of an industrially relevant production and the execution of traditional cell-based assays.

4.1 Characterization of liposomes produced with supercritical CO_2-assisted technology

As a preliminary manufacturing-oriented study, non-functionalized Super Somes liposomes were produced by supercritical CO_2-assisted technology and characterized in terms of mean hydrodynamic diameter, polydispersity index, and Zeta potential. An initial screening was performed to identify the formulation with the most suitable size among the different phosphatidylcholine amounts tested. Among the investigation conditions, the formulation prepared with 125 mg of phosphatidylcholine showed the most favorable size profile (Table 4.1). This formulation exhibited a mean hydrodynamic diameter of approximately 95 ± 22 nm, indicating the formation of nanosized vesicles suitable for further optimization (Figure 4.1). Based on these results, the 125 mg formulation was selected for post-insertion PEGylation. Following PEGylation with DSPE-mPEG2000, the liposomes-maintained nanoscale dimensions, with only a slight increase in mean hydrodynamic diameter from 93 ± 22 nm to 102 ± 22 nm (Figure 4.2; Table 4.1). This moderate increase is consistent with the insertion of PEGylated lipid chains into the liposomal bilayer and suggests that the post-insertion process did not induce relevant aggregation or destabilization of the vesicles (Sornelli et al., 2024).

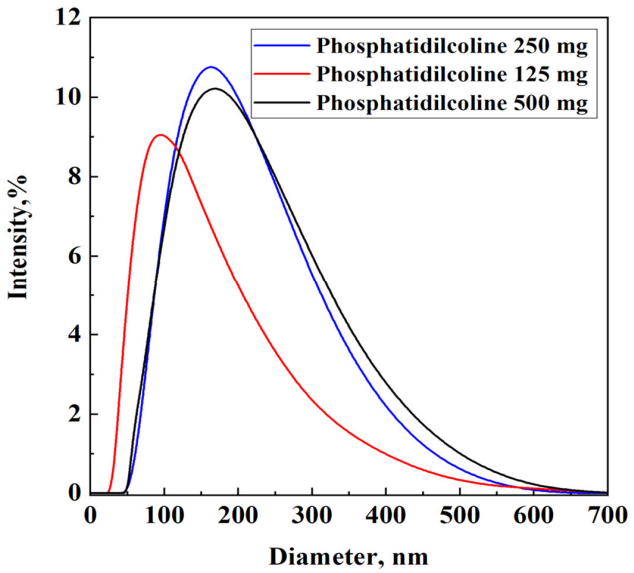


Figure 4.1: Comparison of liposomes produced with different phosphatidylcholine concentrations.

Phosphatidylcholine (mg)	Z-ave (nm)	PDI
125	93±22	0.215
250	132±24	0.242
500	172±28	0.256

Table 4.1: Size and PDI of liposomes produced with different phosphatidylcholine concentrations.

In addition, PEGylation influenced the size distribution of the formulation. The PDI decreased from 0.225 before PEGylation to 0.195 after PEGylation, indicating a narrower size distribution and improved vesicle homogeneity. This suggests that DSPE-mPEG2000 insertion enhanced the homogeneity of the liposomal suspension without compromising its colloidal properties. Surface charge was also modified after PEGylation. Non-PEGylated liposomes showed a ζ-potential of -29.0 ± 7.0 mV, whereas PEGylated liposomes displayed a slightly more negative value of -33.5 ± 9.0 mV (Table 4.2). This shift in ζ-potential further supports the modification of the liposomal surface following DSPE-mPEG2000 insertion.

SAMPLE	Z-ave (nm)	PDI	Zeta Potential (mV)
Pre-PEGylation	93±22	0.225	-29.0±7.0
Post-PEGylation	102±22	0.195	-33.5±9.0

Table 4.2: Comparison of mean hydrodynamic diameter, PDI, and ζ-potential of Super Somes liposomes before and after PEGylation.

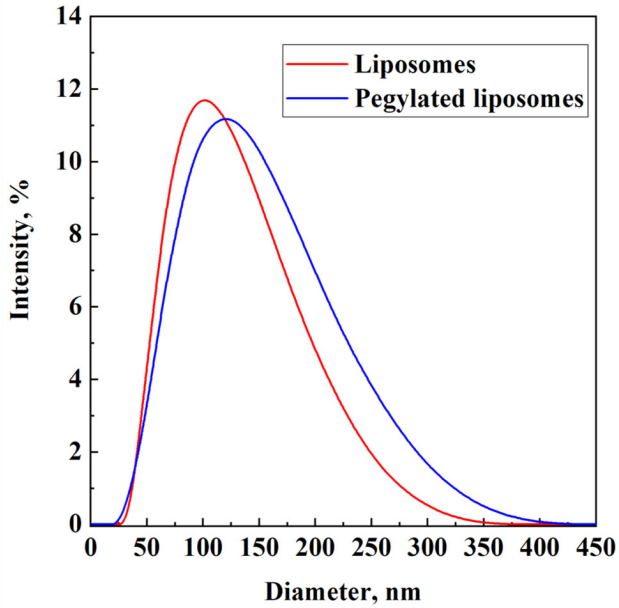


Figure 4.2: Size distribution curves of non-PEGylated and PEGylated Super Somes liposomes.

PEGylated Super Somes liposomes retained suitable nanoscale dimensions and showed improved size homogeneity compared with non-PEGylated liposomes. These results indicate that post-insertion PEGylation was successfully applied and did not negatively affect the main physicochemical properties of the formulation. To complement the physicochemical characterization obtained by DLS, the morphology of PEGylated Super Somes was investigated by scanning electron microscopy (SEM). This analysis was performed to assess vesicle shape, surface appearance, dispersion, and the possible presence of large aggregates following PEGylation. Higher-magnification images confirmed a predominantly spherical morphology, consistent with the expected structure of liposomal vesicles. The particles appeared homogeneous in shape and were generally separated from one another, supporting the good colloidal behavior observed during the physicochemical characterization. These results indicate that post-insertion PEGylation did not compromise the structural integrity of liposomes. The stability of PEGylated liposomes was then monitored over time during storage at 4 °C. As shown in Figure 4.4, after 30 days, the PEGylated formulation is still stable in terms of both size and zeta potential. The data show that supercritical CO_2-assisted technology enabled the production of liposomes with suitable nanoscale properties, while post-insertion PEGylation improved formulation homogeneity and storage stability. These results suggest that supercritical CO_2-assisted technology may be advantageous for future clinical applications, as it enables the production of reproducible, stable, and size-controlled liposomal formulations that are desirable for in vivo delivery.

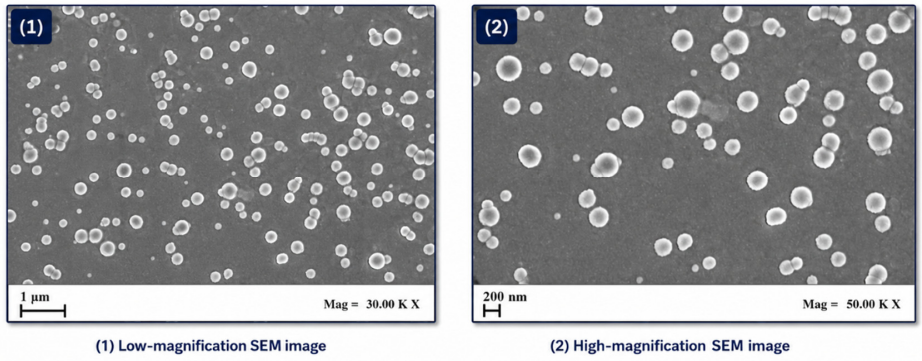


Figure 4.3: SEM morphology of PEGylated Super Somes liposomes. (1) Representative low-magnification image showing well-dispersed nanosized liposomal structures. (2) Higher-magnification image confirming the predominantly spherical morphology of the vesicles and the absence of evident large aggregates. The morphological observations are consistent with the size distribution obtained by DLS analysis.

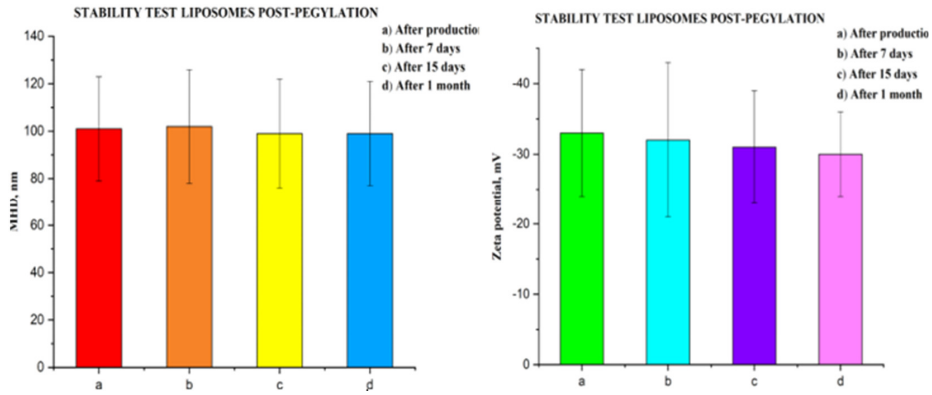


Figure 4.4: Stability over time of PEGylated liposomes during storage at 4 °C.

4.2 Characterization of liposomes prepared by the thin-film hydration method

Dynamic light scattering (DLS) analysis was performed to determine the hydrodynamic diameter and size distribution of the different liposomal formulations. As reported in Table 4.3, all formulations exhibited nanoscale dimensions and low polydispersity index (PDI) values. Untargeted liposomes displayed a mean hydrodynamic diameter of 99.01 nm. Upon surface functionalization, both Q52c- and R2-conjugated liposomes exhibited an increase in particle size, reaching 125.40 nm and 131.30 nm, respectively. This increase is consistent with the successful conjugation of nanobodies onto the liposomal surface. The slightly larger size observed for R2-conjugated liposomes compared to Q52c-functionalized ones may be attributed to differences in nanobody structure, surface density, or orientation, which can influence the hydrodynamic diameter measured by DLS.

All formulations exhibited PDI values below 0.2, indicating a narrow size distribution and suggesting a monodisperse nanoparticle population. Overall, nanobody-functionalized liposomes retained a homogeneous size distribution while displaying moderately increased hydrodynamic diameters compared to untargeted liposomes, confirming that the surface modification did not compromise colloidal stability.

Liposome Type	**Z-Ave (nm)**	**PDI**
Untargeted liposomes	99.01	0.064
R2 Liposomes	131.30	0.168
Q52c Liposomes	125.40	0.110

Table 4.3: Dynamic light scattering (DLS) characterization of liposome formulations. The Z-average diameter (Z-Ave) and polydispersity index (PDI) are reported for untargeted and targeted liposomes.

Zeta potential measurements showed that all liposomal formulations exhibited a slightly negative surface charge (Table 4.4). Untargeted liposomes displayed a zeta potential of -15.0 ± 1.1 mV, while R2- and Q52c-conjugated liposomes showed fewer negative values of -10.3 ± 0.6 mV and -10.6 ± 1.6 mV, respectively.
Following functionalization, a shift toward less negative zeta potential values was observed. This variation is consistent with the presence of nanobodies on the liposomal surface, which can partially mask the intrinsic negative charge of the lipid bilayer (Wöll, 2019).
The relatively low absolute zeta potential values suggest a near-neutral surface, which is characteristic of PEGylated liposomes. The presence of polyethylene glycol (PEG) chains promotes steric stabilization by forming a hydrated barrier around the particles, thereby limiting electrostatic interactions. As a result, colloidal stability in these systems is primarily governed by steric rather than electrostatic repulsion, a behavior commonly reported for PEGylated nanocarriers.

Liposome Type	**Zeta Potential (mV)**
Untargeted liposomes	-15.0±1.1
R2 Liposomes	-10.3±0.6
Q52c Liposomes	-10.6±1.6

Table 4.4: Zeta potential values of liposome formulations. Data is reported as mean ± standard deviation for untargeted and targeted liposomes.

4.3 SDS-PAGE analysis of nanobody-conjugated liposomes

Sodium dodecyl sulfate–polyacrylamide gel electrophoresis (SDS-PAGE) followed by Coomassie Blue staining was performed to qualitatively evaluate and confirm the conjugation of nanobodies onto the liposomal surface. As shown in Figure 4.5, a molecular weight ladder was included, with reference bands at approximately 15, 25, and 35 kDa. Free nanobodies (Q52c and R2) displayed distinct bands at ∼15 kDa, consistent with their expected molecular weight. No protein bands were detected in the untargeted liposome sample, which was used as a negative control, confirming the absence of non-specific protein association or contamination. In contrast, liposomes functionalized with Q52c and R2 nanobodies exhibited bands at higher molecular weights compared to the free nanobodies (∼15 kDa). This shift is consistent with the conjugation of nanobodies to lipid components, which can alter their electrophoretic mobility. Similar observations have been reported in the literature, where conjugated nanobodies migrate at higher molecular weights (∼18–25 kDa or above) than their free counterparts (Mesquita et al., 2022). These results support the successful association of nanobodies with liposomal formulations and confirm that the thiol–maleimide conjugation strategy was suitable for generating nanobody-functionalized liposomes. In addition, Q52c- and R2-functionalized liposomes were evaluated before and after purification. After purification, no unbound nanobodies were detectable.

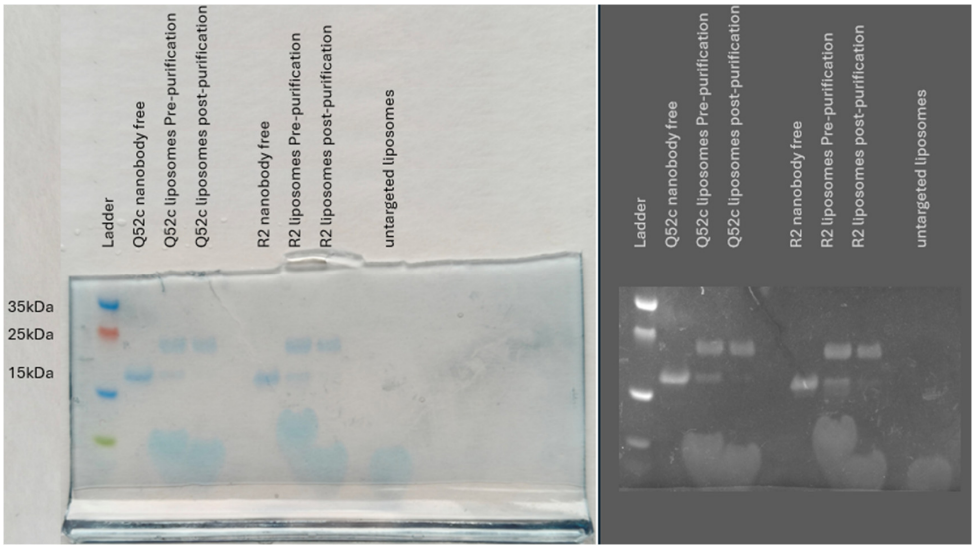


Figure 4.5: Coomassie-stained SDS-PAGE of Q52c, R2 (pre/post-purification) and untargeted liposomes.

4.4 Detection of TfR1 expression levels

Flow cytometry analysis showed that all the investigated cell types expressed TfR1 on their surface, as demonstrated by the high percentage of TfR1-positive cells. Most cell populations showed a percentage of positive cells above 80%, indicating that TfR1 was broadly present in the analyzed models. Lower percentages were observed for hBMEC and TMNK-1 cells, although both cell types still displayed a clear TfR1-positive population (Figure 4.6).

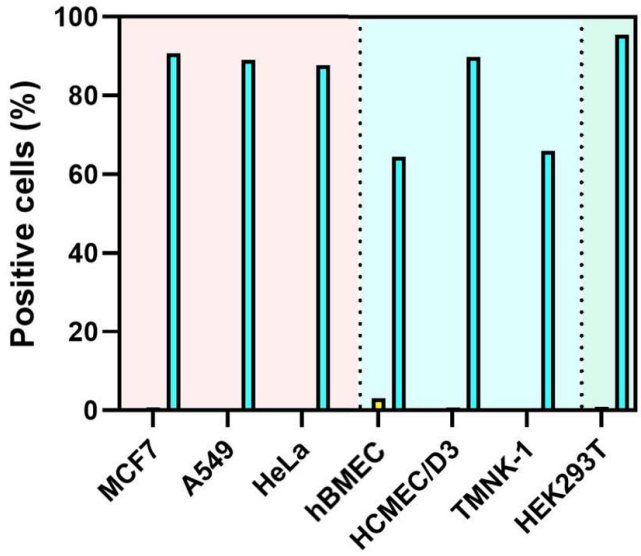


Figure 4.6: Percentage of TfR1 expressing cells in different cell types.

However, a different trend was observed when TfR1 expression was evaluated in terms of mean fluorescence intensity. The MFI analysis revealed marked differences in TfR1 expression levels among the cell lines. Tumor cell lines showed the highest fluorescence intensity, in agreement with literature reports describing TfR1 overexpression in highly proliferative and cancer cells. Among them, MCF7 displayed the highest TfR1 expression, followed by HeLa cells, while A549 showed a lower but still detectable TfR1 expression level. In contrast, non-tumor cell models, including hBMEC, hCMEC/D3, TMNK-1 and HEK293T cells, showed lower MFI values compared with most tumor cell lines. This indicates that, although TfR1 was present in a high percentage in these cells, the receptor expression on the cell surface was lower in these models. (Figure 4.7).

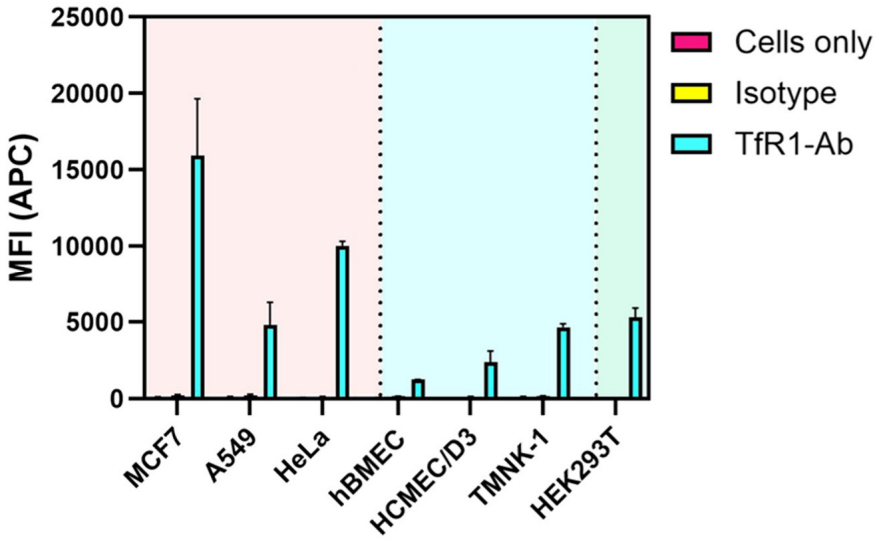


Figure 4.7: TfR1 expression levels in different cell types.

The quantitative flow cytometry results obtained for all the investigated cell lines are summarized in Table 4.5. For each cellular model, the table reports the mean fluorescence intensity (MFI) associated with TfR1 staining, the corresponding standard deviation, the percentage of TfR1-positive cells, and the number of independent experiments performed. These data provide a comparative overview of both the prevalence of TfR1-positive cells within each population and the relative level of receptor expression at the single-cell level.

Cell line	**Cell type**	**TfR1 MFI Ab 1:50**	**SD**	**TfR1 Positive cells (%)**	**SD**	**N. experiments**
MCF7	Tumor	15918.2	3736.1	90.8	5.5	7
HeLa	Tumor	10024.5	306.2	87.8	0.4	3
HEK293T	Human embryonic kidney- derived	5296	60.7	95.7	0.9	3
A549	Tumor	4798.4	1486.6	89	8.2	4
TMNK-1	Hepatic endothelial	4657	224.9	66	5.7	3
hCMEC/D3	Brain endothelial	2375.5	730.4	90	4.3	4
hBMEC	Brain endothelial	1251.5	3.5	64.5	0.4	3

Table 4.5: Quantitative results obtained from flow cytometry.

4.5 Static cellular uptake

As shown in Figure 4.8, after 4 h of incubation at 37 °C, Q52c-functionalized liposomes displayed the highest cellular uptake in all the investigated cell lines compared with both untargeted liposomes and R2-functionalized liposomes. This result indicates that the presence of the Q52c nanobody on the liposome surface enhanced the interaction of the formulation with TfR1-expressing cells. Among the tested cell lines, MCF7 cells showed the strongest uptake of Q52c-functionalized liposomes compared with A549 and hCMEC/D3 cells. This is consistent with the high TfR1 expression previously observed in MCF7 cells. Interestingly, the uptake profile did not completely mirror the TfR1 expression levels measured by flow cytometry. Although A549 cells showed higher TfR1 expression than endothelial hCMEC/D3 cells, the uptake of Q52c-functionalized liposomes was greater in hCMEC/D3 cells than in A549 cells. This suggests that liposome internalization is not determined only by receptor abundance but may also depend on additional cell-specific factors, such as receptor accessibility, membrane dynamics, endocytic activity, or differences in cellular trafficking.

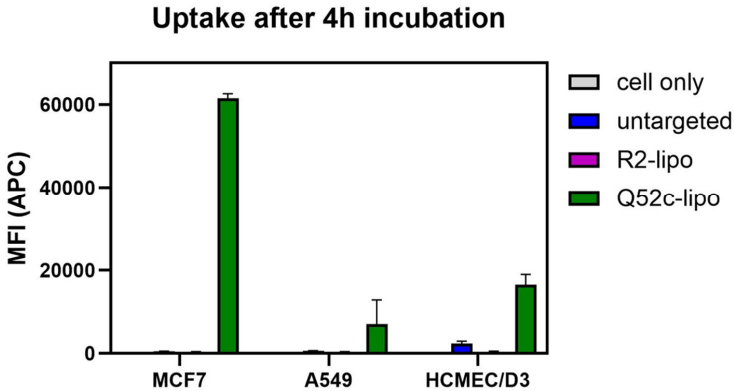


Figure 4.8: Static uptake of liposomes formulations in MCF7, A549 and hCMEC/D3 cells.

To complement the qualitative flow-cytometry results shown in Figure 4.8, the corresponding mean fluorescence intensity (MFI) values are reported in Table 4.6. In addition, Table 4.7 summarizes the fold increase in cellular uptake of Q52c-functionalized liposomes relative to untargeted and R2-functionalized liposomes. As shown in Table 4.6, Q52c-functionalized liposomes produced the highest fluorescence signal in all investigated cell lines, confirming their markedly enhanced cellular association compared with both control formulations. MCF7 cells showed the strongest uptake, with an MFI of 63192, compared with 7040 in A549 cells and 16506 in hCMEC/D3 cells.

This finding is consistent with the high TfR1 expression previously observed in MCF7 cells and supports the ability of Q52c-functionalized liposomes to efficiently target TfR1-positive tumor cells. The fold-change analysis reported in Table 4.7 further highlights the superior performance of the Q52c-functionalized formulation. In MCF7 cells, Q52c-functionalized liposomes showed a 129.5-fold and 147.3-fold higher MFI than untargeted and R2-functionalized liposomes, respectively. Lower, but still substantial, increases were observed in A549 cells, corresponding to 11.3-fold versus untargeted liposomes and 30.7-fold versus R2-functionalized liposomes. In hCMEC/D3 cells, Q52c-functionalized liposomes showed a 7.0-fold increase relative to untargeted liposomes and a 41.5-fold increase relative to R2-functionalized liposomes. Notably, the uptake pattern did not fully reflect the TfR1 expression levels measured by flow cytometry. Although A549 cells displayed higher TfR1 expression than hCMEC/D3 cells, Q52c-functionalized liposomes showed greater uptake in hCMEC/D3 cells. This observation suggests that liposome internalization is not determined exclusively by receptor abundance but may also be influenced by cell-specific factors, including receptor accessibility, membrane composition and dynamics, endocytic activity, and intracellular trafficking pathways. These results demonstrate that Q52c surface functionalization substantially improves liposome uptake across both tumor and endothelial cell models, whereas R2-functionalized liposomes did not provide a comparable enhancement in cellular association.

Cell line	Cell only MFI	Untargeted Liposomes MFI	R2 liposomes MFI	Q52c Liposomes MFI
MCF7	66	488	429	63192
A549	84	621	229	7040
hCMEC/D3	22	2365	398	16506

Table 4.6: Quantitative cellular uptake data expressed as mean fluorescence intensity (MFI) following 4 h incubation at 37 °C with untargeted, R2-functionalized, or Q52c-functionalized liposomes.

Cell line	Q52c/untargeted ratio	Q52c/R2 ratio
MCF7	129.5x	147.3x
A549	11.3x	30.7x
hCMEC/D3	7.0x	41.5x

Table 4.7: Fold increase in MFI of Q52c-functionalized liposomes relative to untargeted and R2-functionalized liposomes.

4.6 Cellular uptake of Q52c-liposomes in hCMEC/D3 cells evaluated under dynamic perfusion conditions

Cellular uptake of the liposomal formulations was evaluated in hCMEC/D3 cells after perfusion in an Ibidi system for 4 h at 37 °C. Following incubation, cells were analysed by fluorescence microscopy. Cell nuclei were stained with Hoechst, shown in blue, while β-actin was labelled with phalloidin, shown in green. DiD-labelled liposomes are visualized in red. As shown in Figure 4.9, untreated cells showed no detectable red fluorescence, confirming the absence of non-specific signal in the liposome-associated fluorescence channel. Similarly, cells treated with untargeted liposomes or R2-liposomes displayed only weak or barely detectable red fluorescence, suggesting limited uptake of these formulations under dynamic flow conditions. In contrast, cells treated with Q52c-liposomes showed a marked increase in red fluorescence signal (Figure 4.10). The signal appeared as numerous punctate fluorescent spots, mainly distributed within the cytoplasmic and perinuclear regions. This punctate pattern is consistent with the accumulation of liposomes in intracellular vesicular structures.

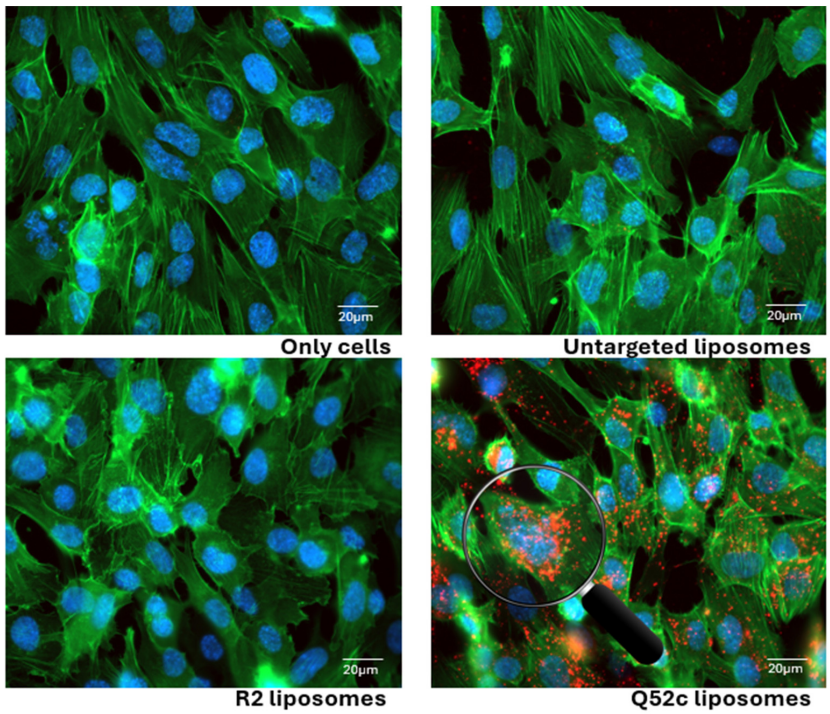


Figure 4.9: Fluorescence microscopy images of Q52c-liposomes in hCMEC/D3 cells compared with control formulations. Green: β-actin; blue: nuclei; red: DiD-labelled Q52c-liposomes. Scale bar: 20.

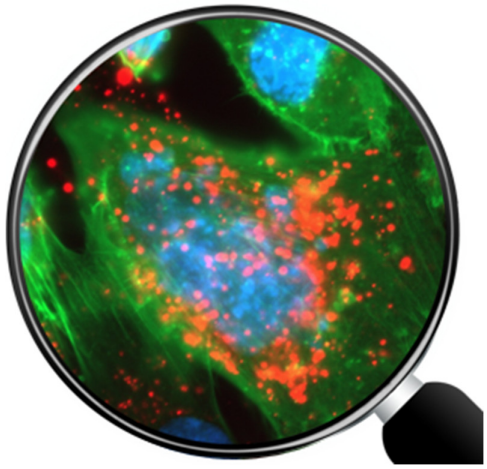


Figure 4.10: Magnified view of a single cell.

To further assess the localization of Q52c-liposomes, fluorescence z-stacks were analyzed following deconvolution. As shown in Figure 4.11, comparison of the widefield and deconvolved images demonstrated that deconvolution reduced out-of-focus fluorescence and improved the visualization of the cellular structures and red liposome-associated puncta. The deconvolved z-stack was subsequently used to generate orthogonal projections. The central X–Y view shows the cells from above, whereas the X–Z and Y–Z views display the same signal along the depth axis. These lateral views allow the red liposome-associated signal to be followed through the thickness of the cells. Based on these observations, Q52c-liposomes appear to be located within the cellular volume rather than being confined to the cell surface.

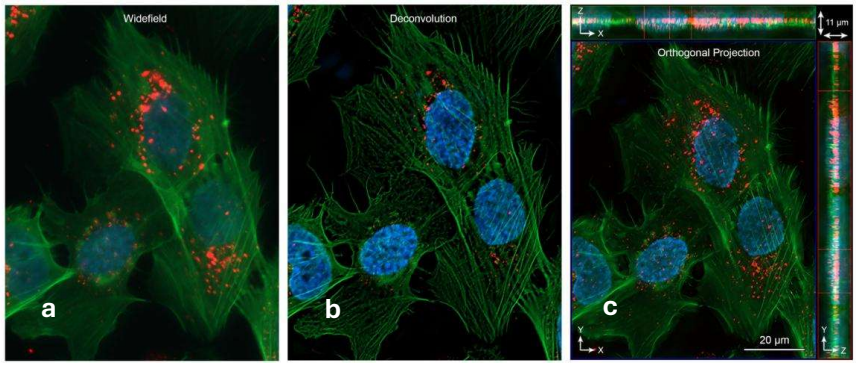


Figure 4.11: Widefield, deconvolved, and orthogonal views of fluorescence z-stacks showing the localization of Q52c-liposomes in hCMEC/D3 cells under dynamic flow conditions. (a) Widefield image. (b) Corresponding deconvolved image. (c) Orthogonal projections of the deconvolved z-stack: the central image represents the X–Y view, while the upper and right panels show the corresponding X–Z and Y–Z views, respectively. Green: β-actin; blue: nuclei; red: DiD-labelled Q52c-liposomes. Scale bar: 20.

In agreement with these observations, the 3D reconstruction, viewed at different angles, showed that the red puncta were distributed within the cellular volume (Figure 4.12). Together, these analyses support the intracellular localization of Q52c-liposomes under dynamic flow conditions.

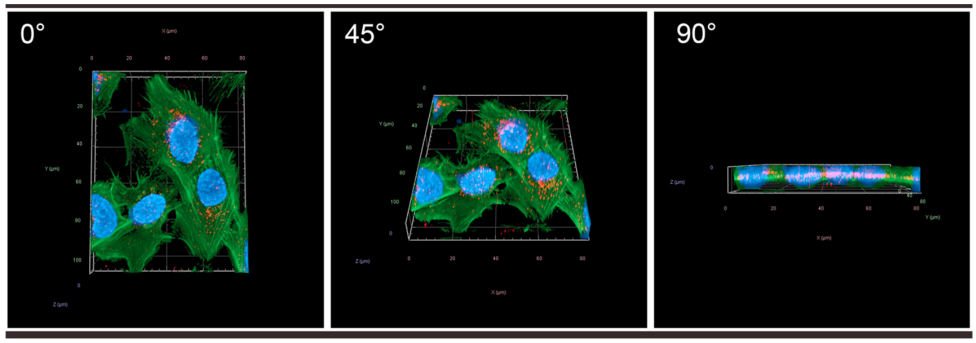


Figure 4.12: Three-dimensional reconstruction of deconvolved fluorescence z-stacks showing the localization of Q52c-liposomes in hCMEC/D3 cells under dynamic flow conditions. The reconstructed cellular volume is shown at 0°, 45°, and 90° rotations. Green: β-actin; blue: nuclei; red: DiD-labelled Q52c-liposomes.

4.7 Perfusion quantification

To account for possible differences in cell number between independent perfusion experiments, the DiD-positive signal was normalized to the number of cells present in each analysed field. Specifically, the total DiD-positive stained area measured in each image was divided by the corresponding number of cells, and the results were expressed as total stained area per cell (μm^2/cell). This normalization allows a more accurate comparison between samples by reducing the influence of cell density on the overall fluorescence signal. Quantification of liposome uptake under dynamic perfusion conditions confirmed the qualitative observations obtained by fluorescence microscopy. The total DiD-positive stained area was measured as an indicator of liposome-associated fluorescence after perfusion. Untargeted liposomes showed only a minimal fluorescent signal, while R2-liposomes displayed a comparable low level of staining, with no significant difference between these two groups. In contrast, TfR1-targeted/Q52c-liposomes showed a marked increase in total DiD-positive area, indicating a significantly higher accumulation of fluorescent liposomes in hCMEC/D3 cells. Statistical analysis confirmed that the difference between Q52c-liposomes and both untargeted liposomes and R2-liposomes was highly significant, with $p < 0.0001$ (Figure 4.13). Conversely, no significant difference was observed between untargeted liposomes and R2-liposomes, supporting the use of R2 as a non-targeting control.

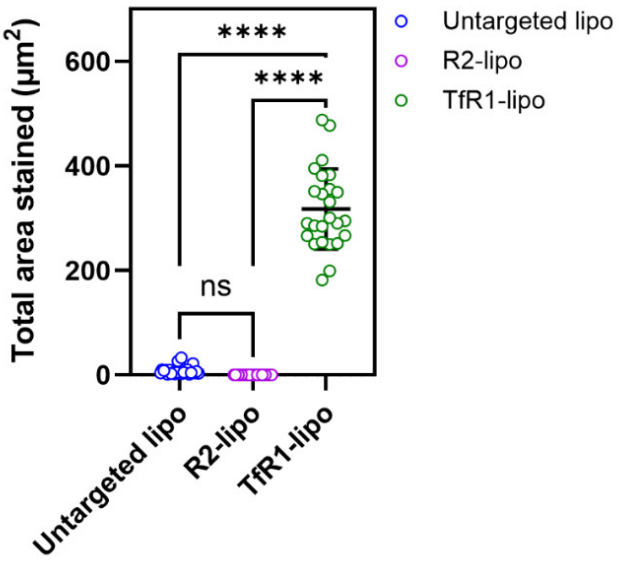


Figure 4.13: Quantification of the total, red-stained area from fluorescence microscopy images.

After normalization, R2-liposomes remained comparable to untargeted liposomes, whereas TfR1-targeted liposomes showed a significantly higher DiD-positive area per cell, supporting enhanced uptake under dynamic perfusion conditions (Figure 4.14).

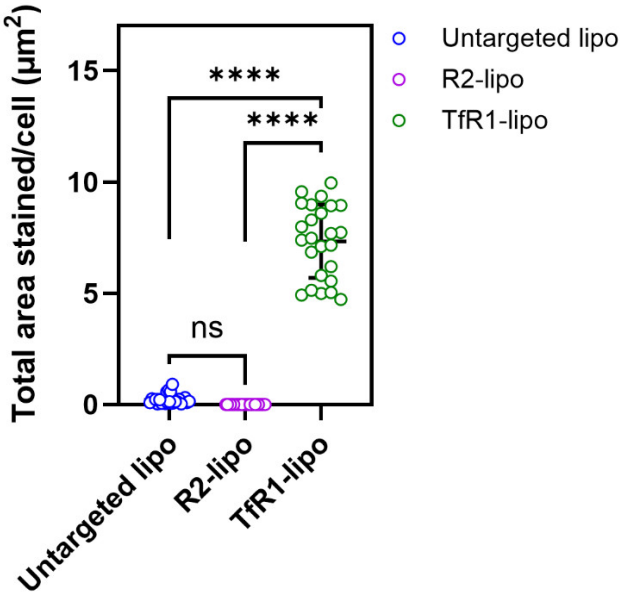


Figure 4.14: Cell-normalized quantification of DiD-positive liposome uptake after perfusion.

5

Discussion

The aim of this doctoral thesis was to develop and evaluate novel nanobody-functionalized liposomes targeting TfR1, with a specific focus on the anti-TfR1 nanobody Q52c. TfR1 represents an attractive molecular target for drug delivery because of its increased expression in several highly proliferative and pathological tissues, as well as its ability to undergo receptor-mediated internalization. However, despite widespread interest in TfR1-targeted delivery, critical knowledge gaps persist. A systematic profiling of TfR1 expression across distinct cellular models remains essential to identify the biological context in which this receptor may represent a suitable and effective target. Furthermore, the cellular uptake of TfR1-targeted nanocarriers is often assessed under static in vitro conditions, which does not fully reflect the dynamic environment encountered in vivo. Addressing these limitations is essential to clarify the actual translational value of TfR1 as a target for nanomedicine-based drug delivery.

By comparing TfR1 expression in a panel of cellular models, this work provided a rational basis for selecting the models used in uptake studies and for assessing the suitability of TfR1 as a drug delivery target (Daniels et al., 2012; Johnsen et al., 2019; Mojarad-Jabali et al., 2022). Flow cytometric analysis also revealed that the percentage of TfR1-positive cells did not always correspond to the mean fluorescence intensity (MFI), confirming that these two parameters provide complementary information. While a high percentage indicates widespread, moderate expression across the population, elevated MFI reflects high receptor density per cell; evaluating both parameters is therefore essential to fully delineate receptor availability. A second central aspect of this work was the formulation of Q52c-functionalized liposomes. While most TfR1-targeted liposomes documented in the literature utilize transferrin, conventional monoclonal antibodies, antibody fragments, or synthetic peptides, single-domain antibodies (nanobodies, VHHs) remain largely underexplored, despite their nanoscale dimensions, robust conformational stability, and capacity for site-directed conjugation.

Notably, this doctoral work provides the first report of liposomes functionalized with the anti-TfR1 nanobody Q52c for active drug delivery. A key strength of the experimental design was the inclusion of both non-targeted liposomes and R2-functionalized liposomes as controls. Non-targeted liposomes allowed the evaluation of baseline, non-specific liposome association with cells, whereas R2-functionalized liposomes served as a nanobody-decorated control. This comparison was important because it allowed Q52c-mediated targeting to be distinguished from possible effects related simply to the presence of a nanobody on the liposomal surface. Static uptake assays provided an initial evaluation of liposome–cell interactions under conventional in vitro conditions. Static assays are widely used in nanomedicine because they are technically accessible, reproducible, and suitable for comparative screening of different formulations. However, these conditions do not reproduce the mechanical forces experienced by circulating nanocarriers in vivo, particularly fluid flow and shear stress. Shear stress can influence nanoparticle–cell interactions by affecting particle transport toward the cell surface, residence time at the cell membrane, ligand–receptor engagement, and subsequent internalization. In contrast, under static conditions, liposomes remain in prolonged contact with the cell monolayer, potentially increasing apparent uptake and overestimating cell–nanocarrier interactions. Therefore, they provide an incomplete assessment of in *vivo* behavior. Importantly, cellular accumulation of Q52c-liposomes did not strictly correlate with total TfR1 expression: despite exhibiting lower receptor levels than lung adenocarcinoma A549 cells, hCMEC/D3 brain endothelial cells internalized higher levels of Q52c-liposomes. This discrepancy highlights that endocytic efficiency is not governed solely by receptor abundance but is co-determined by cell-type-specific membrane dynamics. Brain capillary endothelial cells possess constitutively active endocytic machinery and tightly regulated endosomal sorting/recycling cascades optimized for physiological receptor turnover and transcytosis across the BBB. Conversely, carcinoma models exhibit slower vesicular processing.

These findings suggest that the success of TfR1-targeted delivery depends on the interplay between receptor expression, endocytic capacity, and intracellular trafficking efficiency, rather than on receptor density alone. The evaluation of liposome uptake under dynamic flow conditions using an Ibidi µ-Slide perfusion system represents a further innovative aspect of this work. This platform exposes cells to a continuous unidirectional laminar flow and defined shear stress, mimicking the vascular environment. Under flow, liposomes must interact with the cell surface under more stringent conditions than in static culture, as shear stress reduces particle residence time at the membrane and demands more robust ligand–receptor engagement for successful internalization. This provides the first evidence that Q52c-mediated targeting of TfR1 is effective under physiologically relevant dynamic flow, helping to bridge the gap between conventional static assays and the in vivo vascular environment.

Despite the relevant and original results obtained, however, some limitations should be acknowledged, and future perspectives of this work should be defined. First, the experiments performed in this thesis demonstrated the association and uptake of Q52c-functionalized liposomes in brain endothelial cells, but they do not yet establish whether these systems are able to cross the BBB by transcytosis. For this reason, future studies should evaluate the transport of Q52c-functionalized liposomes in more complex BBB models, such as co-culture systems, Transwell models, microfluidic platforms, or organ-on-chip systems, which would allow endothelial internalization to be distinguished from true transport across the barrier. A second relevant aspect concerns the possible competition with healthy cells expressing high levels of TfR1. Since TfR1 is abundantly expressed in cells physiologically involved in iron metabolism, such as reticulocytes and erythroid precursors, TfR1-targeted liposomes may also interact with these cell populations. Therefore, it will be important to evaluate the interaction of Q52c-functionalized liposomes with reticulocytes under perfusion conditions, using whole-blood systems or isolated cell populations. Moreover, models including both endothelial cells and reticulocytes could help clarify the cellular distribution of TfR1-targeted liposomes and their degree of selectivity toward the endothelial compartment. From a methodological perspective, future work should strengthen technical robustness by expanding the reporting of independent biological replicates ($n \geq 3$) and detailed statistical workflows. Experimentally, this involves implementing quantitative assays to determine conjugation efficiency and conducting receptor-blocking experiments to confirm TfR1 specificity.

Future studies should investigate the encapsulation of a therapeutic active compound to determine not only the uptake efficiency of the nanocarrier, but also its actual ability to deliver a pharmacological cargo and produce a biological or therapeutic effect. Furthermore, it will be essential to assess protein corona formation under more realistic biological conditions. Exposure of liposomes to human plasma may lead to the adsorption of plasma proteins onto their surface, potentially modifying their size, charge, colloidal stability, and receptor-recognition ability. In particular, the protein corona could partially mask the Q52c ligand or alter its interaction with TfR1, thereby influencing cellular uptake and biodistribution. Moreover, after validation in more complex in vitro models, in vivo studies will be required to confirm the biodistribution, targeting selectivity, safety, and delivery efficiency of Q52c-functionalized liposomes. These studies will be essential to evaluate the real translational potential of the platform developed in this thesis. In parallel, this thesis explored the feasibility of supercritical CO_2-assisted process to produce non-functionalized liposomes. Although preliminary, the results obtained are highly promising and demonstrate the intrinsic manufacturing advantages of this approach over traditional thin-film hydration; nevertheless, further investigations are required to fully establish its translational viability.

6

Conclusions

Q52c-functionalized liposomes displayed strong TfR1-targeting activity. Under both static and flow conditions, targeted liposomes showed enhanced cellular uptake in TfR1-expressing cells compared with non-targeted and R2-functionalized controls. These original and innovative results, as compared to previous works (see f.i. Adepu and Ramakrishna, 2021; Andra et al., 2022; Chelliah et al., 2025; Ding et al., 2025; Egwu et al., 2024; Gatto et al., 2024; Zhang et al., 2025), support the use of Q52c as a promising targeting ligand for TfR1-directed liposomes and suggest that nanobody-mediated receptor recognition can improve liposome-cell interactions even under physiologically relevant conditions. This work provides a methodological contribution to the development of more predictive in vitro models for targeted nanomedicine. However, further studies are needed to determine whether the enhanced cellular uptake observed in vitro can translate into efficient BBB transport and effective therapeutic cargo delivery.

In addition, the preliminary investigation of supercritical CO_2-assisted process highlighted the potential of this approach as a green and efficient manufacturing platform for future liposomal formulations. Although conventional thin-film hydration was selected in this study because it was more suitable for small-batch laboratory production, nanobody functionalization, and cost-effective formulation development, supercritical CO_2-assisted production offers key advantages in terms of process control, reproducibility, scalability, reduced use of organic solvents, and mild operating conditions.

The claims regarding scalability, batch reproducibility, clinical potential, and the reduction of off-target adverse effects should, however, be regarded as prospective, since this study was exploratory in nature and neither drug-loaded formulations nor *in vivo* biodistribution and safety profiles were evaluated.

Therefore, future studies should explore the surface functionalization supercritical CO_2 produced liposomes with targeting ligands, including anti-TfR1 nanobodies, and systematically evaluate their colloidal stability, drug-loading capacity, receptor-mediated uptake, and *in vivo* pharmacokinetic behavior. In this perspective this technique may contribute to bridging the gap between laboratory-scale formulation development and clinically translatable liposomal nanomedicines. (Muro, 2012; Pearce and O'Reilly, 2019).

Aknowlegments

I would like to express my sincere gratitude to my supervisor, Prof. Pietro Campiglia, for his trust and for giving me the opportunity to pursue this enriching research journey. I am deeply grateful to him for his constant encouragement and for believing in me and my ideas at every stage of this path.

.

My heartfelt thanks go to my co-supervisor, Prof. Lucia Baldino, for her availability, kindness, and support.I am deeply grateful for warmly welcoming me into her research group. Her encouragement, valuable suggestions, and constructive feedback have been instrumental in my scientific and professional growth.

I would like to express my sincere gratitude to Prof. Ernesto Reverchon for allowing me to carry out my research activities in his laboratories and for sharing his invaluable teachings. I am deeply thankful to him for embodying such an inspiring example of determination and intellectual independence: he showed me that even as an independent thinker who follows their own path, one can always find the strength and resilience to move forward with unwavering conviction.

I would also like to thank Prof. Alessia Bertamino for her valuable support and encouragement.

A special thanks goes to Prof. Marcel Fens, from Utrecht University. I do not have enough words to thank you for welcoming me to the Netherlands with extraordinary generosity, warmth, and availability, making me feel right at home. Thank you from the bottom of my heart for guiding me step by step through my PhD project, for helping me with every single thing, and for constantly encouraging and pushing me to give my best. You have been much more than a supervisor: with your infinite patience, your invaluable advice, and your constant presence, you have made this period in Utrecht an unforgettable chapter of my life, leaving a deep mark on my professional and personal growth.

A sincere and deep thanks also goes to Prof. Massimiliano Caiazzo, from Utrecht University, for welcoming me into his research group and for his constant availability. I would like to thank him from the bottom of my heart for his invaluable advice and for supporting me with competence and continuous encouragement throughout my year spent in the Netherlands.

My heartfelt thanks go to the technicians who supported and guided me in Utrecht: Antoinette, Mies, Roel, Kim, Arjen and Bonnie for teaching me so much and for always assisting me with great kindness, patience, and professionalism.

I would like to extend my heartfelt thanks to Barbara Mesquita and Katerina Xenaki from Utrecht University for their dedication and support in the laboratory. Thank you for your invaluable guidance and for the patience with which you answered my every question, helping me clear up all my doubts and uncertainties.

Furthermore, I extend my sincere thanks to Prof. Enrico Mastrobattista, Head of the Department of Pharmaceutical Sciences at Utrecht University, for hosting me during my visiting period, and for facilitating the connections that gave me the opportunity to meet and collaborate with Prof. Marcel Fens and Prof. Massimiliano Caiazzo

To my parents, my deepest roots and safest harbor: thank you for nurturing my steps from the very beginning and for believing in my dreams. Your quiet, patient, and unconditional love has been the guiding light through every shadow ; without you, I would never have found the wings to reach this high, nor the warmth of a home to return to.

I would like to express my heartfelt gratitude to my brother, Davide, for his constant closeness and support during my stay in Utrecht. His invaluable advice, encouragement, and reassuring presence have been a guiding light and a comfort to me. A special thanks goes to him for making the months away from home lighter and for all the carefree weekends, laughter, and shared moments that I will hold in my heart forever.

To my love Carlos, precious anchor of this journey and of my daily life: my deepest and most heartfelt thanks for always being by my side, for soothing my fears, and for celebrating every small victory with your sweet smile. Without your constant presence beside me, without the gentle way you reminded me of my strength when mine was failing, I could never have faced this steep path. You painted a sky inside me and lit every star; you stayed to hold my hand when all around there was only darkness. You are and will forever be my bright place

A special thanks goes to Carmen, for an authentic friendship that knows neither distance nor boundaries. Your constant support and precious encouragement have been an inexhaustible source of strength, guiding me throughout this entire PhD journey. You managed to make me feel all your warmth and presence even from afar, during the months I spent in the Netherlands. Thank you from the bottom of my heart for never letting your light fade, even through the most difficult moments.

A special thanks goes to Magda, for a friendship born during our university days that time has never faded. Even though the rhythms of life allow us to see each other less than we would like, our bond has remained unchanged and deep. You were by my side to celebrate my graduation, and today you are still here with me on this milestone day for my PhD. Thank you from the bottom of my heart for always being there, for supporting me, for encouraging me, and for sharing every milestone, big and small, with me.

Ringraziamenti

Desidero esprimere la mia sincera gratitudine al mio supervisore, il Prof. Pietro Campiglia, per la sua fiducia e per avermi dato l'opportunità di intraprendere questo arricchente percorso di ricerca. Gli sono profondamente grata per avermi costantemente sostenuta, e per aver creduto in me e nelle mie idee in ogni fase di questo cammino.
.
Il mio sentito ringraziamento va alla mia co-supervisore, la Prof.ssa Lucia Baldino, per la sua disponibilità, gentilezza e supporto. Le sono profondamente grata per avermi accolta calorosamente nel suo gruppo di ricerca. I suoi incoraggiamenti, i preziosi suggerimenti e i feedback costruttivi sono stati fondamentali per la mia crescita scientifica e professionale.

Vorrei esprimere la mia sincera gratitudine al Prof. Ernesto Reverchon per avermi permesso di svolgere le mie attività di ricerca nei suoi laboratori e per aver condiviso i suoi preziosi insegnamenti. Gli sono profondamente grata per aver rappresentato un esempio così stimolante di determinazione e indipendenza intellettuale: mi ha mostrato che, anche come pensatore autonomo che segue la propria strada, si può sempre trovare la forza e la resilienza per andare avanti con incrollabile convinzione.

Vorrei inoltre ringraziare la Prof.ssa Alessia Bertamino per il suo prezioso supporto e incoraggiamento.

Un ringraziamento speciale va al Prof. Marcel Fens, dell'Università di Utrecht. Non ho parole sufficienti per ringraziarti per avermi accolta in Olanda con una generosità, un calore e una disponibilità straordinari, facendomi sentire subito a casa. Grazie di cuore per avermi guidata passo dopo passo nel mio progetto di dottorato, per avermi aiutata in ogni singola cosa e per avermi costantemente incoraggiata e spronata a dare il massimo. Sei stato molto più di un supervisore: con la tua pazienza infinita, i tuoi preziosi consigli e la tua presenza costante, hai reso questo periodo a Utrecht un capitolo indimenticabile della mia vita, lasciando un segno profondo nella mia crescita professionale e personale.

Un ringraziamento sincero e profondo è rivolto anche al Prof. Massimiliano Caiazzo, dell'Università di Utrecht, per avermi accolta nel suo gruppo di ricerca e per la costante disponibilità dimostrata. Desidero ringraziarlo di cuore per i suoi preziosi consigli e per avermi sostenuta con competenza e continuo incoraggiamento durante tutto l'anno trascorso in Olanda.

I miei più sentiti ringraziamenti vanno ai tecnici che mi hanno supportata e guidata a Utrecht: Antoinette, Mies, Roel, Kim ,Arjen and Bonnie per avermi insegnato così tanto e per avermi sempre assistita con grande gentilezza, pazienza e professionalità.

Desidero ringraziare di cuore Barbara Mesquita e Katerina Xenaki, dell'Università di Utrecht, per avermi affiancato con tanta dedizione in laboratorio. Grazie per i vostri preziosi consigli e per la pazienza con cui avete risposto a ogni mia domanda aiutandomi a fugare ogni mio dubbio e incertezza .

Desidero inoltre rivolgere un sincero ringraziamento al Prof. Enrico Mastrobattista, Direttore del Dipartimento di Scienze Farmaceutiche dell'Università di Utrecht, per avermi ospitata durante il mio periodo di ricerca e per aver favorito le connessioni che mi hanno dato l'opportunità di conoscere e collaborare con il Prof. Marcel Fens e il Prof. Massimiliano Caiazzo.

Ai miei genitori, le mie radici più profonde e il mio porto più sicuro: grazie per aver accompagnato i miei passi fin dall'inizio e per aver creduto nei miei sogni. Il vostro amore silenzioso, paziente e incondizionato è stato la luce guida attraverso ogni ombra; senza di voi, non avrei mai trovato le ali per arrivare così in alto, né il calore di una casa a cui fare ritorno.

Vorrei esprimere la mia sentita gratitudine a mio fratello, Davide, per la sua costante vicinanza e il suo supporto durante il mio soggiorno a Utrecht. I suoi preziosi consigli, il suo incoraggiamento e la sua presenza rassicurante sono stati una guida e un conforto per me. Un grazie speciale va a lui per aver reso più leggeri i mesi lontani da casa e per tutti i fine settimana spensierati, le risate e i momenti condivisi insieme che conserverò sempre nel cuore.

Al mio amato Carlos, ancora preziosa di questo viaggio e della mia vita quotidiana: il mio ringraziamento più profondo e sentito per essere sempre stato al mio fianco, per aver placato le mie paure e per aver celebrato ogni mia piccola vittoria con il tuo dolce sorriso. Senza la tua presenza costante accanto a me, senza il modo delicato con cui mi hai ricordato la mia forza quando la mia veniva meno, non avrei mai potuto affrontare questo impervio percorso. Hai dipinto un cielo dentro di me e ha acceso ogni stella; sei rimasto a stringermi la mano quando intorno c'era soltanto il buio. Sei e sarai per sempre il mio posto luminoso.

Un ringraziamento speciale va a Carmen, per un'amicizia autentica che non conosce distanze né confini. Il tuo sostegno costante e il tuo incoraggiamento prezioso sono stati una fonte inesauribile di forza, capace di guidarmi lungo tutto il percorso di questo dottorato. Sei riuscita a farmi sentire tutto il tuo calore e la tua presenza anche da lontano, durante i mesi trascorsi in Olanda. Grazie di cuore per non aver mai fatto mancare la tua luce, anche nei momenti più difficili.

Un ringraziamento speciale va a Magda, per un'amicizia nata ai tempi dell'università e che il tempo non ha mai scalfito. Anche se i ritmi della vita ci consentono di vederci meno di quanto vorremmo, il nostro legame è rimasto immutato e profondo. Sei stata al mio fianco a festeggiare la mia laurea, e oggi sei ancora qui con me in questo giorno così importante per il mio dottorato. Grazie di cuore per esserci sempre, a sostenermi, a incoraggiarmi e a condividere ogni mio piccolo grande traguardo.

Bibliography

P. Aisen, C. Enns, and M. Wessling-Resnick. Chemistry and biology of eukaryotic iron metabolism. *The International Journal of Biochemistry & Cell Biology*, 33 (10):940–959, 2001. doi: 10.1016/s1357-2725(01)00063-2.

M. Ali, R. Y. Kim, A. C. Brown, J. R. Mayall, R. Karim, J. W. Pinkerton, G. Liu, K. L. Martin, M. R. Starkey, A. L. Pillar, C. Donovan, P. S. Pathinayake, O. Carroll, D. Trinder, H. L. Tay, Y. Badi, N. Z. Kermani, Y. K. Guo, R. Aryal, et al. Crucial role for lung iron level and regulation in the pathogenesis and severity of asthma. *European Respiratory Journal*, 55(4):1901340, 2020. doi: 10.1183/13993003.01340-2019.

J. Allen, K. R. Backstrom, J. A. Cooper, M. C. Cooper, T. C. Detwiler, D. W. Essex, R. P. Fritz, R. T. Means, P. B. Meier, S. R. Pearlman, B. Roitman-Johnson, and P. A. Seligman. Measurement of soluble transferrin receptor in serum of healthy adults. *Clinical Chemistry*, 44(1):35–39, 1998. doi: 10.1093/clinchem/44.1.35.

N. M. AlSawaftah, N. S. Awad, V. Paul, P. S. Kawak, M. H. Al-Sayah, and G. A. Husseini. Transferrin-modified liposomes triggered with ultrasound to treat hela cells. *Scientific Reports*, 11(1):11589, 2021. doi: 10.1038/s41598-021-90349-6.

I. Altintas, R. Heukers, R. van der Meel, P. M. P. van Bergen en Henegouwen, and C. F. van Nostrum. Nanobody–functionalized polymeric micelles for tumor-targeted drug delivery. *Journal of Controlled Release*, 165(2):110–118, 2013. doi: 10.1016/j.jconrel.2012.11.005.

M. Amin, M. Mansourian, P. C. Burgers, B. Amin, M. R. Jaafari, and T. L. M. Ten Hagen. Increased targeting area in tumors by dual-ligand modification of liposomes with rgd and tat peptides. *Pharmaceutics*, 14(2):458, 2022. doi: 10.3390/pharmaceutics14020458.

F. S. Anarjan. Active targeting drug delivery nanocarriers: Ligands. *Nano-Structures & Nano-Objects*, 19:100370, 2019. doi: 10.1016/j.nanoso.2019.100370.

V. V. S. N. L. Andra, S. V. N. Pammi, L. V. K. P. Bhatraju, and L. K. Ruddaraju. A comprehensive review on novel liposomal methodologies, commercial formulations, clinical trials and patents. *BioNanoScience*, 12(1):274–291, 2022. doi: 10.1007/s12668-022-00941-x.

R. Anttila, J. D. Cook, and M. A. Siimes. Body iron stores decrease in boys during pubertal development: The transferrin receptor-ferritin ratio as an indicator of iron status. *Pediatric Research*, 41(2):224–228, 1997. doi: 10.1203/00006450-199702000-00012.

A. Arguello, C. S. Mahon, and M. E. K. Calvert. Molecular architecture determines brain delivery of a transferrin receptor-targeted lysosomal enzyme. *Journal of Experimental Medicine*, 219(3):e20211057, 2022. doi: 10.1084/jem.20211057.

M. R. Aronson, S. H. Medina, and M. J. Mitchell. Peptide functionalized liposomes for receptor targeted cancer therapy. *APL Bioengineering*, 5(1):011501, 2021. doi: 10.1063/5.0029860.

Y. H. Bae and K. Park. Targeted drug delivery: What's the hurdle? *Journal of Controlled Release*, 153(3):198–205, 2011. doi: 10.1016/j.jconrel.2011.05.001.

D. Banerjee, P. R. Flanagan, J. Cluett, and L. S. Valberg. Transferrin receptors in the human gastrointestinal tract. *Gastroenterology*, 91(4):861–869, 1986. doi: 10.1016/0016-5085(86)90687-6.

A. D. Bangham. Membrane models with phospholipids. *Progress in Biophysics and Molecular Biology*, 18:29–95, 1968. doi: 10.1016/0079-6107(68)90019-9.

Y. Barenholz. Doxil®—the first fda-approved nano-drug: Lessons learned. *Journal of Controlled Release*, 160(2):117–134, 2012. doi: 10.1016/j.jconrel.2012.03.020.

T. Barrientos, I. Laothamatas, T. R. Koves, E. J. Soderblom, M. Bryan, M. A. Moseley, D. M. Muoio, and N. C. Andrews. Metabolic catastrophe in mice lacking transferrin receptor in muscle. *EBioMedicine*, 2(11):1705–1717, 2015. doi: 10.1016/j.ebiom.2015.09.041.

P. Bataille Backer and S. K. Adesina. Synthesis and characterization of transferrin receptor-targeted peptide combination sn-38 and rucaparib conjugate for the treatment of glioblastoma. *Pharmaceutics*, 17(6):732, 2025. doi: 10.3390/pharmaceutics17060732.

A. Bates and C. A. Power. David vs. goliath: The role of nanobodies in overcoming the hurdles of monoclonal antibody therapy. *Antibodies*, 8(2):28, 2019. doi: 10.3390/antib8020028.

R. D. Baynes, Y. J. Shih, and J. D. Cook. Mechanism of production of the serum transferrin receptor. In C. Hershko, editor, *Progress in Iron Research*, pages 51–58. Springer US, 1994. doi: 10.1007/978-1-4615-2554-7_7.

Y. Beguin. Soluble transferrin receptor for the evaluation of erythropoiesis and iron status. *Clinica Chimica Acta*, 329(1–2):9–22, 2003. doi: 10.1016/S0009-8981(03)00005-6.

Y. Beguin, R. Oris, and G. Fillet. Dynamics of erythropoietic recovery after bone marrow transplantation: Role of marrow proliferative capacity and erythropoietin production in autologous versus allogeneic transplants. *Bone Marrow Transplantation*, 11(4):285–292, 1993.

L. Belfiore, D. N. Saunders, M. Ranson, K. J. Thurecht, G. Storm, and K. L. Vine. Towards clinical translation of ligand-targeted liposomes. *Journal of Controlled Release*, 277:1–13, 2018. doi: 10.1016/j.jconrel.2018.02.040.

G. Bergamaschi, K. Markopoulos, R. Albertini, M. Di Stefano, I. de Vincenzi, and M. Ponz de Leon. Transferrin receptor expression in the human placenta. *Placenta*, 11(5):463–472, 1990. doi: 10.1016/S0143-4004(05)80183-0.

C. Berthou, J. P. Iliou, and D. Barba. Iron, neuro-bioavailability and depression. *Frontiers in Psychiatry*, 12:724707, 2021. doi: 10.3389/fpsyt.2021.724707.

N. Bertrand, J. Wu, X. Xu, N. Kamaly, and O. C. Farokhzad. Cancer nanotechnology: The impact of passive and active targeting in the era of modern cancer biology. *Advanced Drug Delivery Reviews*, 66:2–25, 2014. doi: 10.1016/j.addr.2013.11.009.

N. Bien-Ly, Y. J. Yu, D. Bumbaca, J. ElSohly, N. D. Prevost, S. Ho, Y. Zhang, C. S. McKenzie, and R. J. Watts. Transferrin receptor (tfr) trafficking determines brain uptake of tfr antibody affinity variants. *Journal of Experimental Medicine*, 211(2):233–244, 2014. doi: 10.1084/jem.20131660.

M. B. Bierings, H. G. van Eijk, G. de Jong, and J. P. van Dijk. Transferrin receptor expression and the regulation of placental iron uptake. *Placenta*, 12(4):333–341, 1991. doi: 10.1016/0143-4004(91)90076-7.

J. Bjerner, L. M. Amlie, L. S. Rusten, and E. Jakobsen. Serum levels of soluble transferrin receptor correlate with severity of disease but not with iron stores in patients with malignant lymphomas. *Tumour Biology*, 23(3):146–153, 2002. doi: 10.1159/000064031.

G. Bonvicini, S. Singh, L. Sandersjöö, D. Sehlin, S. Syvänen, and K. G. Andersson. The effects of dose, valency, and affinity on tfr-mediated brain delivery in vivo. *Fluids and Barriers of the CNS*, 22(1):36, 2025. doi: 10.1186/s12987-025-00643-y.

P. Bourassa, W. Alata, C. Tremblay, S. Paris-Robidas, and F. Calon. Transferrin receptor-mediated uptake at the blood–brain barrier is not impaired by

alzheimer's disease neuropathology. *Molecular Pharmaceutics*, 16(2):583–594, 2019. doi: 10.1021/acs.molpharmaceut.8b00870.

N. Boyle, A. Hunter, D. O'Malley, H. O'Brien, P. J. Twomey, M. P. Keane, A. Byrne, and C. McCarthy. Elevated ferritin as a marker of disease stability: Insights into iron dysregulation in idiopathic pulmonary fibrosis [abstract]. *American Journal of Respiratory and Critical Care Medicine*, 211:A17, 2025. doi: 10.1164/ajrccm.2025.211.Abstracts.A17.

M. Broekgaarden, R. van Vught, S. Oliveira, R. C. Roovers, P. M. P. van Bergen en Henegouwen, R. J. Pieters, T. M. Van Gulik, E. Breukink, and M. Heger. Site-specific conjugation of single domain antibodies to liposomes enhances photosensitizer uptake and photodynamic therapy efficacy. *Nanoscale*, 8(12):6490–6494, 2016. doi: 10.1039/c6nr00014b.

S. Cai, Z. Yuan, Y. Chen, M. Gong, J. Lai, P. Yan, and Z. Mei. Transferrin and borneol-enhanced liposomes for targeted rapamycin delivery in tbi. *International Journal of Nanomedicine*, 20:4503–4518, 2025. doi: 10.2147/IJN.S489165.

P. V. Candelaria, L. S. Leoh, M. L. Penichet, and T. R. Daniels-Wells. Antibodies targeting the transferrin receptor 1 (tfr1) as direct anti-cancer agents. *Frontiers in Immunology*, 12:607692, 2021. doi: 10.3389/fimmu.2021.607692.

X. Cao, X. Zhang, H. Wang, Z. Chen, Y. Wu, and Y. Li. Transferrin receptor 1 is associated with progression and poor prognosis in breast cancer. *Frontiers in Oncology*, 12:839308, 2022. doi: 10.3389/fonc.2022.839308.

X. Chang, M. Ma, L. Chen, Z. Song, Z. Zhao, W. Shen, H. Jiang, Y. Wu, M. Fan, and H. Wu. Identification and characterization of elevated expression of transferrin and its receptor tfr1 in mouse models of depression. *Brain Sciences*, 12(10): 1267, 2022. doi: 10.3390/brainsci12101267.

R. Chelliah, M. Rubab, S. Vijayalakshmi, M. Karuvelan, K. Barathikannan, and D. H. Oh. Liposomes for drug delivery: Classification, therapeutic applications, and limitations. *Next Nanotechnology*, 8:100209, 2025. doi: 10.1016/j.nxnano.2025.100209.

D. Chen, X. Liu, X. Lu, and J. Tian. Nanoparticle drug delivery systems for synergistic delivery of tumor therapy. *Frontiers in Pharmacology*, 14:1111991, 2023. doi: 10.3389/fphar.2023.1111991.

Y. Cheng, O. Zak, P. Aisen, S. C. Harrison, and T. Walz. Structure of the human transferrin receptor–transferrin complex. *Cell*, 116(4):565–576, 2004. doi: 10.1016/S0092-8674(04)00130-8.

S. R. Chirasani, D. S. Markovic, M. Synowitz, S. A. Eichler, P. Wisniewski, B. Kaminska, and H. Kettenmann. Transferrin-receptor-mediated iron accumulation controls proliferation and glutamate release in glioma cells. *Journal of Molecular Medicine*, 87(2):153–167, 2009. doi: 10.1007/s00109-008-0414-3.

M. Corte-Rodríguez, E. Blanco-González, J. Bettmer, and M. Montes-Bayón. Quantitative analysis of transferrin receptor 1 (tfr1) in individual breast cancer cells by means of labeled antibodies and elemental (icp-ms) detection. *Analytical Chemistry*, 91(24):15532–15538, 2019. doi: 10.1021/acs.analchem.9b03438.

R. R. Crichton. *Inorganic biochemistry of iron metabolism: From molecular mechanisms to clinical consequences*. John Wiley & Sons, 2nd edition, 2001. doi: 10.1002/9781118925645.

D. J. A. Crommelin, P. van Hoogevest, and G. Storm. The role of liposomes in clinical nanomedicine development. what now? now what? *Journal of Controlled Release*, 318:256–263, 2020. doi: 10.1016/j.jconrel.2019.12.023.

C. Cui, X. Cheng, L. Yan, H. Ding, X. Guan, W. Zhang, X. Tian, and C. Hao. Downregulation of tfr1 promotes progression of colorectal cancer via the jak/stat pathway. *Cancer Management and Research*, 11:6323–6341, 2019. doi: 10.2147/CMAR.S198911.

F. Danhier, O. Feron, and V. Préat. To exploit the tumor microenvironment: Passive and active tumor targeting of nanocarriers for anti-cancer drug delivery. *Journal of Controlled Release*, 148(2):135–146, 2010. doi: 10.1016/j.jconrel.2010.08.027.

T. R. Daniels, E. Bernabeu, J. A. Rodríguez, S. Patel, M. Kozman, D. A. Chiappetta, E. Holler, J. Y. Ljubimova, G. Helguera, and M. L. Penichet. The transferrin receptor and the targeted delivery of therapeutic agents against cancer. *Biochimica et Biophysica Acta (BBA) - General Subjects*, 1820(3):291–317, 2012. doi: 10.1016/j.bbagen.2011.07.016.

A. Dautry-Varsat. Receptor-mediated endocytosis: The intracellular journey of transferrin and its receptor. *Biochimie*, 68(3):375–381, 1986. doi: 10.1016/s0300-9084(86)80004-9.

M. E. Davis, Z. G. Chen, and D. M. Shin. Nanoparticle therapeutics: An emerging treatment modality for cancer. *Nature Reviews Drug Discovery*, 7(9):771–782, 2008. doi: 10.1038/nrd2614.

G. de Jong, J. P. van Dijk, and H. G. van Eijk. The biology of transferrin. *Clinica Chimica Acta*, 190(1–2):1–46, 1990. doi: 10.1016/0009-8981(90)90278-Z.

A. De la Rosa, N. G. Metzendorf, J. Efverström, A. Godec, D. Sehlin, J. Morrison, and G. Hultqvist. Lowering the affinity of single-chain monovalent bbb shuttle scfc-scfv8d3 prolongs its half-life and increases brain concentration. *Neurotherapeutics*, 21(5):e00492, 2024. doi: 10.1016/j.neurot.2024.e00492.

Z. Deng, D. H. Manz, S. V. Torti, and F. M. Torti. Iron-responsive element-binding protein 2 plays an essential role in regulating prostate cancer cell growth. *Oncotarget*, 8(47):82231–82243, 2017. doi: 10.18632/oncotarget.18369.

S. Dev and J. L. Babitt. Overview of iron metabolism in health and disease. *Hemodialysis International*, 21(Suppl 1):S6–S20, 2017. doi: 10.1111/hdi.12542.

Y. Ding, Y. Kong, L. Jia, Q. Geng, Q. Jin, Y. Liu, G. Xu, S. Guo, J. Xu, and S. Zhao. Screening and functional characterization of nanobodies targeting the transferrin receptor. *Protein Expression and Purification*, 231:106702, 2025. doi: 10.1016/j.pep.2025.106702.

B. Dos Santos Rodrigues, S. Lakkadwala, T. Kanekiyo, and J. Singh. Dual-modified liposome for targeted and enhanced gene delivery into mice brain. *Journal of Pharmacology and Experimental Therapeutics*, 374(2):354–365, 2020. doi: 10.1124/jpet.119.264127.

C. Dufès, M. Al Robaian, and S. Somani. Transferrin and transferrin receptors in drug delivery. *Therapeutic Delivery*, 4(5):629–640, 2013. doi: 10.4155/tde.13.21.

C. O. Egwu, C. Aloke, K. T. Onwe, C. I. Umoke, J. Nwafor, R. A. Eyo, J. A. Chukwu, G. O. Ufebe, J. Ladokun, D. T. Audu, A. O. Agwu, D. C. Obasi, and C. O. Okoro. Nanomaterials in drug delivery: Strengths and opportunities in medicine. *Molecules*, 29(11):2584, 2024. doi: 10.3390/molecules29112584.

R. S. Eisenstein. Iron regulatory proteins and the molecular control of mammalian iron metabolism. *Annual Review of Nutrition*, 20(1):627–662, 2000. doi: 10.1146/annurev.nutr.20.1.627.

D. R. Elias, A. Poloukhtine, V. Popik, and A. Tsourkas. Effect of ligand density, receptor density, and nanoparticle size on cell targeting. *Nanomedicine: Nanotechnology, Biology and Medicine*, 9(2):194–201, 2012. doi: 10.1016/j.nano.2012.05.015.

T. J. Esparza, Y. J. Yu, and C. Pérez-García. A ph-sensitive transferrin receptor nanobody enables efficient blood–brain barrier transcytosis in vivo. *Fluids and Barriers of the CNS*, 20(1):62, 2023. doi: 10.1186/s12987-023-00462-z.

R. Eugster, M. Orsi, G. Buttitta, N. Serafini, M. Tiboni, L. Casettari, J. L. Reymond, S. Aleandri, and P. Luciani. Leveraging machine learning to streamline the

development of liposomal drug delivery systems. *Journal of Controlled Release*, 376:1025–1038, 2024. doi: 10.1016/j.jconrel.2024.10.065.

Y. Fang, J. Xue, S. Gao, A. Lu, D. Yang, H. Jiang, Y. He, and K. Shi. Cleavable pegylation: A strategy for overcoming the "peg dilemma" in stimulative pharmaceutical nanocarriers. *Journal of Controlled Release*, 306:1–12, 2018. doi: 10.1016/j.jconrel.2019.05.041.

R. Faresjö, H. Lindberg, S. Ståhl, J. Löfblom, S. Syvänen, and D. Sehlin. Transferrin receptor binding bbb-shuttle facilitates brain delivery of anti-aβ-affibodies. *Pharmaceutical Research*, 39(7):1509–1521, 2022. doi: 10.1007/s11095-022-03282-2.

W. P. Faulk, B. L. Hsi, and P. J. Stevens. Transferrin and transferrin receptors in carcinoma of the breast. *The Lancet*, 316(8191):390–392, 1980. doi: 10.1016/S0140-6736(80)90440-7.

C. Fillebeen, E. Charlebois, J. Wagner, A. Katsarou, J. Mui, H. Vali, D. Garcia-Santos, P. Ponka, J. Presley, and K. Pantopoulos. Transferrin receptor 1 controls systemic iron homeostasis by fine-tuning hepcidin expression to hepatocellular iron load. *Blood*, 133(4):344–355, 2019. doi: 10.1182/blood-2018-05-850404.

C. H. Flowers, B. S. Skikne, A. M. Covell, and J. D. Cook. The clinical measurement of serum transferrin receptor. *Journal of Laboratory and Clinical Medicine*, 114(4):368–377, 1989.

F. Fontana, M. Raimondi, M. Marzagalli, M. Sommariva, and P. Limonta. Intratumoral heterogeneity and iron metabolism: The emerging role of transferrin receptor 1 in cancer progression. *Cancers*, 15(5):1234, 2023. doi: 10.3390/cancers15051234.

B. Gabold, F. Adams, and S. Brameyer. Transferrin-modified chitosan nanoparticles for targeted nose-to-brain delivery of proteins. *Drug Delivery and Translational Research*, 13(3):822–838, 2023. doi: 10.1007/s13346-022-01245-z.

B. Galy, M. Conrad, and M. Muckenthaler. Mechanisms controlling cellular and systemic iron homeostasis. *Nature Reviews Molecular Cell Biology*, 25(2):133–155, 2024. doi: 10.1038/s41580-023-00648-1.

K. C. Gatter, G. Brown, I. S. Trowbridge, R. E. Woolston, and D. Y. Mason. Transferrin receptors in human tissues: Their distribution and possible clinical relevance. *Journal of Clinical Pathology*, 36(5):539–545, 1983. doi: 10.1136/jcp.36.5.539.

M. S. Gatto, M. P. Johnson, and W. Najahi-Missaoui. Targeted liposomal drug delivery: Overview of the current applications and challenges. *Life*, 14(6):672, 2024. doi: 10.3390/life14060672.

S. Giordani, V. Marassi, A. Zattoni, B. Roda, and P. Reschiglian. Liposomes characterization for market approval as pharmaceutical products: Analytical methods, guidelines and standardized protocols. *Journal of Pharmaceutical and Biomedical Analysis*, 236:115751, 2023. doi: 10.1016/j.jpba.2023.115751.

K. Gkouvatsos, G. Papanikolaou, and K. Pantopoulos. Regulation of iron transport and the role of transferrin. *Biochimica et Biophysica Acta (BBA) - General Subjects*, 1820(3):188–202, 2012. doi: 10.1016/j.bbagen.2011.10.013.

P. T. Gomme, K. B. McCann, and J. Bertolini. Transferrin: Structure, function and potential therapeutic actions. *Drug Discovery Today*, 10(4):267–273, 2005. doi: 10.1016/S1359-6446(04)03333-1.

S. Gosk, C. Vermehren, G. Storm, and T. Moos. Targeting anti-transferrin receptor antibody (ox26) and ox26-conjugated liposomes to brain capillary endothelial cells using in situ perfusion. *Journal of Cerebral Blood Flow & Metabolism*, 24(11): 1193–1204, 2004. doi: 10.1097/01.WCB.0000135592.28823.47.

S. Goswami, W. Wang, T. Arakawa, and S. Ohtake. Developments and challenges for mab-based therapeutics. *Antibodies*, 2(3):452–500, 2013. doi: 10.3390/antib2030452.

G. Gregoriadis. Molecular compartmentalization in the treatment of genetic disorders. *Nature*, 244(5412):170–172, 1973. doi: 10.1038/244170a0.

Q. Guo, L. Li, S. Hou, Z. Yuan, C. Li, W. Zhang, L. Zheng, and X. Li. The role of iron in cancer progression. *Frontiers in Oncology*, 11:778492, 2021. doi: 10.3389/fonc.2021.778492.

S. Guo, T. Guan, and R. Tai. A nuclei bombing nano-system improves sting-activated cancer immunotherapy. *Nano Today*, 63:102749, 2025. doi: 10.1016/j.nantod.2025.102749.

Y. Gupta, A. Jain, and S. K. Jain. Transferrin-conjugated solid lipid nanoparticles for enhanced delivery of doxorubicin to brain. *Journal of Pharmacy and Pharmacology*, 59(7):935–940, 2007. doi: 10.1211/jpp.59.7.0005.

H. O. Habashy, D. G. Powe, C. M. Staka, E. A. Rakha, I. O. Ellis, and A. R. Green. Transferrin receptor (cd71) is a marker of poor prognosis in breast cancer and can predict response to tamoxifen. *Breast Cancer Research and Treatment*, 119(2):283–293, 2010. doi: 10.1007/s10549-009-0345-x.

J. A. Habeshaw, A. G. Stansfeld, and T. A. Lister. Correlation of transferrin receptor expression with histological class and outcome in non-hodgkin lymphoma. *The Lancet*, 321(8323):498–501, 1983. doi: 10.1016/S0140-6736(83)92191-8.

W. A. Hall, A. Godal, S. Juell, and O. Fodstad. In vitro efficacy of transferrin–toxin conjugates against glioblastoma multiforme. *Journal of Neurosurgery*, 76(5): 838–844, 1992. doi: 10.3171/jns.1992.76.5.0838.

C. Hamers-Casterman, T. Atarhouch, S. Muyldermans, G. Robinson, C. Hamers, E. B. Songa, N. Bendahman, and R. Hamers. Naturally occurring antibodies devoid of light chains. *Nature*, 363(6428):446–448, 1993. doi: 10.1038/363446a0.

L. Han, R. Huang, S. Liu, S. Huang, and C. Jiang. Peptide-conjugated pamam for targeted doxorubicin delivery to transferrin receptor overexpressed tumors. *Molecular Pharmaceutics*, 7(6):2156–2165, 2010. doi: 10.1021/mp100185f.

C. E. Herbison, K. Thorstensen, A. C. G. Chua, R. M. Graham, P. Leedman, J. K. Olynyk, and D. Trinder. The role of transferrin receptor 1 and 2 in transferrin-bound iron uptake in human hepatoma cells. *American Journal of Physiology - Cell Physiology*, 297(6):C1567–C1575, 2009. doi: 10.1152/ajpcell.00649.2008.

S. Hong, P. R. Leroueil, I. J. Majoros, B. G. Orr, J. R. Baker, and M. M. Banaszak Holl. The binding avidity of a nanoparticle-based multivalent targeting platform. *Chemistry & Biology*, 13(1):107–115, 2006. doi: 10.1016/j.chembiol.2005.10.014.

R. D. Horniblow, M. Bedford, R. Hollingworth, S. Evans, E. Sutton, N. Lal, A. D. Beggs, T. H. Iqbal, and C. Tselepis. Braf mutations are associated with increased iron regulatory protein-2 expression in colorectal tumourigenesis. *Cancer Science*, 108(6):1135–1143, 2017. doi: 10.1111/cas.13234.

Y. Hu, C. Liu, and S. Muyldermans. Nanobody-based delivery systems for diagnosis and therapy. *Frontiers in Immunology*, 8:1442, 2017. doi: 10.3389/fimmu.2017.01442.

N. Hubert, G. Lescoat, R. Sciot, R. Moirand, P. Jego, P. Leroyer, and P. Brissot. Regulation of ferritin and transferrin receptor expression by iron in human hepatocyte cultures. *Journal of Hepatology*, 18(3):301–312, 1993. doi: 10.1016/s0168-8278(05)80274-0.

H. A. Huebers and C. A. Finch. The physiology of transferrin and transferrin receptors. *Physiological Reviews*, 67(2):520–582, 1987. doi: 10.1152/physrev.1987.67.2.520.

H. A. Huebers, Y. Beguin, P. Pootrakul, D. Einspahr, and C. A. Finch. Intact transferrin receptors in human plasma and their relation to erythropoiesis. *Blood*, 75(1):102–107, 1990. doi: 10.1182/blood.V75.1.102.102.

B. J. Iacopetta, E. H. Morgan, and G. C. T. Yeoh. Receptor-mediated uptake and endocytosis of transferrin by developing erythroid cells in culture. *British Journal of Haematology*, 52(4):529–539, 1982. doi: 10.1111/j.1365-2141.1982.tb04744.x.

M. Imam, J. Ji, Z. Zhang, and S. Yan. Targeting the initiator to activate both ferroptosis and cuproptosis for breast cancer treatment: Progress and possibility for clinical application. *Frontiers in Pharmacology*, 15:1493188, 2025. doi: 10.3389/fphar.2024.1493188.

M. L. Immordino, F. Dosio, and L. Cattel. Stealth liposomes: Review of the basic science, rationale, and clinical applications, existing and potential. *International Journal of Nanomedicine*, 1(3):297–315, 2006.

S. Y. Jeong, S. H. Hwang, and R. H. Seong. Transferrin receptor regulates pancreatic cancer growth by modulating mitochondrial respiration and ros generation. *Biochemical and Biophysical Research Communications*, 471(3):373–379, 2016. doi: 10.1016/j.bbrc.2016.02.023.

A. Jhaveri, P. Deshpande, B. Pattni, and V. Torchilin. Transferrin-targeted, resveratrol-loaded liposomes for the treatment of glioblastoma. *Journal of Controlled Release*, 277:89–101, 2018. doi: 10.1016/j.jconrel.2018.03.007.

K. B. Johnsen and T. Moos. Revisiting nanoparticle technology for blood–brain barrier transport: Unfolding at the endothelial gate improves the fate of transferrin receptor–targeted liposomes. *Journal of Controlled Release*, 222:32–46, 2016. doi: 10.1016/j.jconrel.2015.12.005.

K. B. Johnsen, A. Burkhart, and F. Melander. Targeting transferrin receptors at the blood-brain barrier improves the uptake of immunoliposomes and subsequent cargo transport into the brain parenchyma. *Scientific Reports*, 7(1):10396, 2017. doi: 10.1038/s41598-017-11220-1.

K. B. Johnsen, M. Bak, and P. J. Kempen. Antibody affinity and valency impact brain uptake of transferrin receptor-targeted gold nanoparticles. *Theranostics*, 8(12):3416–3436, 2018. doi: 10.7150/thno.25228.

K. B. Johnsen, A. Burkhart, L. B. Thomsen, T. L. Andresen, and T. Moos. Targeting the transferrin receptor for brain drug delivery. *Progress in Neurobiology*, 181:101665, 2019. doi: 10.1016/j.pneurobio.2019.101665.

I. R. D. Johnson, E. J. Parkinson-Lawrence, T. Shandala, R. Weigert, L. M. Butler, and D. A. Brooks. Altered endosome biogenesis in prostate cancer has biomarker potential. *Molecular Cancer Research*, 12(12):1851–1862, 2014. doi: 10.1158/1541-7786.MCR-14-0074.

S. Kang, W. Duan, S. Zhang, D. Chen, J. Feng, and N. Qi. Muscone/ri7217 co-modified upward messenger dtx liposomes enhanced permeability of blood-brain barrier and targeting glioma. *Theranostics*, 10(9):4308–4322, 2020. doi: 10.7150/thno.41322.

T. Kang, Z. Han, L. Zhu, and B. Cao. Tfr1 knockdown alleviates iron overload and mitochondrial dysfunction during neural differentiation of alzheimer's disease-derived induced pluripotent stem cells by interacting with gsk3b. *Journal of Translational Medicine*, 22(1):101, 2024. doi: 10.1186/s40001-024-01677-y.

Y. Kang, S. Kim, H. Lee, J. Park, and Y. Kim. Association between soluble transferrin receptor levels and chronic diseases: Links with diabetes mellitus and chronic kidney disease. *Nutrients*, 14(17):3456, 2022. doi: 10.3390/nu14173456.

R. Karim, C. Palazzo, B. Evrard, and G. Piel. Nanocarriers for the treatment of glioblastoma multiforme: Current state-of-the-art. *Journal of Controlled Release*, 227:23–37, 2016. doi: 10.1016/j.jconrel.2016.02.026.

T. Kaur, J. Upadhyay, S. Pukale, A. Mathur, and M. N. Ansari. Investigation of trends in the research on transferrin receptor-mediated drug delivery via a bibliometric and thematic analysis. *Pharmaceutics*, 14(12):2574, 2022. doi: 10.3390/pharmaceutics14122574.

H. Kawabata. Transferrin and transferrin receptors update. *Free Radical Biology and Medicine*, 133:46–54, 2019. doi: 10.1016/j.freeradbiomed.2018.06.037.

P. Kawak, N. M. AlSawaftah, W. G. Pitt, and G. A. Husseini. Transferrin-targeted liposomes in glioblastoma therapy: A review. *International Journal of Molecular Sciences*, 24(17):13262, 2023. doi: 10.3390/ijms241713262.

H. N. Keer, J. M. Kozlowski, Y. C. Tsai, C. Lee, R. N. McEwan, and J. T. Grayhack. Elevated transferrin receptor content in human prostate cancer cell lines assessed in vitro and in vivo. *The Journal of Urology*, 143(2):381–385, 1990. doi: 10.1016/S0022-5347(17)39970-6.

A. Khan, P. Singh, and A. Srivastava. Iron: Key player in cancer and cell cycle? *Journal of Trace Elements in Medicine and Biology*, 62:126582, 2020. doi: 10.1016/j.jtemb.2020.126582.

H. Kim, L. B. Villareal, and Z. Liu. Transferrin receptor-mediated iron uptake promotes colon tumorigenesis. *Advanced Science*, 10(12):2207693, 2023. doi: 10.1002/advs.202207693.

I. Kindrat, V. Tryndyak, and A. de Conti. Microrna-152-mediated dysregulation of hepatic transferrin receptor 1 in liver carcinogenesis. *Oncotarget*, 7(2):1276–1287, 2016. doi: 10.18632/oncotarget.6004.

Y. Kohgo, T. Nishisato, H. Kondo, N. Tsushima, Y. Niitsu, and I. Urushizaki. Circulating transferrin receptor in human serum. *British Journal of Haematology*, 64(2):277–281, 1986. doi: 10.1111/j.1365-2141.1986.tb04422.x.

I. Kondo, H. Ino, and S. Nonoyama. Expression of transferrin receptor in human brain tumors. *Acta Neuropathologica*, 80(3):276–280, 1990. doi: 10.1007/bf00308919.

T. Koneru, E. McCord, S. Pawar, K. Tatiparti, S. Sau, and A. K. Iyer. Transferrin: Biology and use in receptor-targeted nanotherapy of gliomas. *ACS Omega*, 6(13): 8727–8733, 2021. doi: 10.1021/acsomega.0c05848.

S. A. A. Kooijmans, J. J. J. M. Gitz-Francois, R. M. Schiffelers, and P. Vader. Recombinant phosphatidylserine-binding nanobodies for targeting of extracellular vesicles to tumor cells: A plug-and-play approach. *Nanoscale*, 10(5):2413–2426, 2018. doi: 10.1039/c7nr06966a.

S. Kukulj, M. Jaganjac, and M. Boranic. Altered iron metabolism, inflammation, transferrin receptors, and ferritin expression in non-small-cell lung cancer. *Medical Oncology*, 27(2):268–277, 2010. doi: 10.1007/s12032-009-9203-2.

P. Kumari, B. Ghosh, and S. Biswas. Nanocarriers for cancer-targeted drug delivery. *Journal of Drug Targeting*, 24(3):179–191, 2016. doi: 10.3109/1061186X.2015.1051047.

S. R. Kuvibidila, R. P. Warrier, L. Yu, D. L. Ode, and R. Gardner. Serum soluble transferrin receptor in patients with prostate cancer and benign prostatic hyperplasia. *American Journal of Clinical and Experimental Urology*, 6(3):132–139, 2018.

F. C. Lam, S. W. Morton, and J. Wyckoff. Enhanced efficacy of combined temozolomide and bromodomain inhibitor therapy for gliomas using targeted nanoparticles. *Nature Communications*, 9(1):1991, 2018. doi: 10.1038/s41467-018-04315-4.

T. Lamtha, L. Tabtimmai, K. Bangphoomi, D. Kiriwan, A. A. Malik, W. Chaicumpa, P. M. P. van Bergen en Henegouwen, and K. Choowongkomon.

Generation of a nanobody against her2 tyrosine kinase using phage display library screening for her2-positive breast cancer therapy development. *Protein Engineering, Design and Selection*, 34:gzab030, 2021. doi: 10.1093/protein/gzab030.

C. M. Lawrence, S. Ray, M. Babyonyshev, R. Galluser, D. W. Borhani, and S. C. Harrison. Crystal structure of the ectodomain of human transferrin receptor. *Science*, 286(5440):779–782, 1999. doi: 10.1126/science.286.5440.779.

J. H. Lee, J. A. Engler, J. F. Collawn, and B. A. Moore. Receptor mediated uptake of peptides that bind the human transferrin receptor. *European Journal of Biochemistry*, 268(7):2004–2012, 2001. doi: 10.1046/j.1432-1327.2001.02073.x.

S. Levi, M. Ripamonti, A. S. Moro, and A. Cozzi. Iron imbalance in neurodegeneration. *Molecular Psychiatry*, 29(1):104–116, 2024. doi: 10.1038/s41380-023-02399-z.

J. E. Levy, O. Jin, Y. Fujiwara, F. Kuo, and N. C. Andrews. Disruption of the mouse transferrin receptor gene (tfrc) leads to embryonic lethality and severe defects in iron transport. *Proceedings of the National Academy of Sciences*, 96(2): 798–803, 1999. doi: 10.1073/pnas.96.2.798.

J. Li, Y. Yang, and L. Huang. Calcium phosphate nanoparticles with an asymmetric lipid bilayer coating for sirna delivery to the tumor. *Journal of Controlled Release*, 152(1):49–56, 2011. doi: 10.1016/j.jconrel.2011.01.027.

J. Li, Z. Zhang, B. Zhang, X. Yan, and K. Fan. Transferrin receptor 1 targeted nanomedicine for brain tumor therapy. *Biomaterials Science*, 11(10):3394–3413, 2023. doi: 10.1039/d2bm02152h.

X. Li, L. Ding, Y. Xu, Y. Wang, and Q. Ping. Targeted delivery of doxorubicin using stealth liposomes modified with transferrin. *International Journal of Pharmaceutics*, 373(1–2):116–123, 2009. doi: 10.1016/j.ijpharm.2009.01.023.

M. Liang, C. Gao, and Y. Wang. Enhanced blood–brain barrier penetration and glioma therapy mediated by t7 peptide-modified low-density lipoprotein particles. *Drug Delivery*, 25(1):1652–1663, 2018. doi: 10.1080/10717544.2018.1494223.

Q. Liu, M. Wang, Y. Hu, H. Xing, X. Chen, Y. Zhang, and P. Zhu. Significance of cd71 expression by flow cytometry in diagnosis of acute leukemia. *Leukemia & Lymphoma*, 55(4):892–898, 2014. doi: 10.3109/10428194.2013.819100.

Y. Liu, L. Scrivano, and J. Peterson. Egfr-targeted nanobody functionalized polymeric micelles loaded with mthpc for selective photodynamic therapy. *Molecular Pharmaceutics*, 17(4):1276–1292, 2020. doi: 10.1021/acs.molpharmaceut.9b01280.

Z. Liu, Y. Yang, and Y. Zhou. Carnosic acid-loaded transferrin-modified liposomes for hepatocellular carcinoma therapy. *Drug Delivery*, 28(1):1421–1431, 2021. doi: 10.1080/10717544.2021.1943058.

M. Lombard, A. B. Bomford, R. J. Polson, A. J. Bellingham, and R. Williams. Differential expression of transferrin receptor in duodenal mucosa in iron overload. *Gastroenterology*, 98(4):976–984, 1990. doi: 10.1016/0016-5085(90)90022-s.

D. Lombardo and M. A. Kiselev. Methods of liposomes preparation: Formation and control factors of versatile nanocarriers for biomedical and nanomedicine application. *Pharmaceutics*, 14(3):543, 2022. doi: 10.3390/pharmaceutics14030543.

R. T. MacGillivray, E. Mendez, J. G. Shewale, S. K. Sinha, J. Lineback-Zins, and K. Brew. The primary structure of human serum transferrin. *The Journal of Biological Chemistry*, 258(6):3543–3553, 1983. doi: 10.1016/S0021-9258(18)32695-1.

O. Maksymova, H. Zhang, and F. Li. Nanobody-based therapeutics for cancer: Emerging insights into targeting the tumor microenvironment. *Molecular Cancer*, 24(1):14, 2025. doi: 10.1186/s12943-025-02270-5.

L. Martínez-Jothar, N. Beztsinna, C. F. Van Nostrum, W. E. Hennink, and S. Oliveira. Selective cytotoxicity to her2 positive breast cancer cells by saporin-loaded nanobody-targeted polymeric nanoparticles in combination with photochemical internalization. *Molecular Pharmaceutics*, 16(4):1633–1647, 2019. doi: 10.1021/acs.molpharmaceut.8b01318.

E. Mastrobattista, G. A. Koning, and G. Storm. Immunoliposomes for the targeted delivery of antitumor drugs. *Advanced Drug Delivery Reviews*, 40(1–2):103–127, 1999. doi: 10.1016/S0169-409X(99)00043-5.

Y. Matsumura and H. Maeda. A new concept for macromolecular therapeutics in cancer chemotherapy: Mechanism of tumoritropic accumulation of proteins and the antitumor agent smancs. *Cancer Research*, 46(12 Pt 1):6387–6392, 1986.

K. M. Mayle, A. M. Le, and D. T. Kamei. The intracellular trafficking pathway of transferrin. *Biochimica et Biophysica Acta (BBA) - General Subjects*, 1820(3):264–281, 2012. doi: 10.1016/j.bbagen.2011.09.009.

L. J. Medeiros, L. J. Picker, S. J. Horning, and R. A. Warnke. Transferrin receptor expression by non-hodgkin's lymphomas: Correlation with morphologic grade and survival. *Cancer*, 61(9):1844–1851, 1988. doi: 10.1002/1097-0142(19880501)61:9<1844::aid-cncr2820610921>3.0.co;2-4.

R. Mehta, D. Suvarna, C. P. Mustafa, and S. Sadasivan. Role of soluble transferrin receptors study in hepatocellular carcinoma with underlying cirrhosis. *Indian Journal of Cancer*, 42(4):215, 2005. doi: 10.4103/ijca_2005424_215.

F. Meng, S. Asghar, and S. Gao. Transferrin decorated methoxy poly(ethylene glycol)-poly(lactic-co-glycolic acid) nanoparticles for the targeted delivery of curcumin. *Biomaterials*, 32(31):790–799, 2011. doi: 10.1016/j.biomaterials.2011.07.074.

B. S. Mesquita, M. H. A. M. Fens, and A. Di Maggio. The impact of nanobody density on the targeting efficiency of pegylated liposomes. *International Journal of Molecular Sciences*, 23(23):14974, 2022. doi: 10.3390/ijms232314974.

L. Messori and F. Kratz. Transferrin: From inorganic biochemistry to medicine. *Metal-Based Drugs*, 1(2–3):161–167, 1994. doi: 10.1155/MBD.1994.161.

G. Metzgeroth, B. Schultheis, C. Kuhn, A. Dorn-Beineke, P. La Rosée, R. Hehlmann, and J. Hastka. The soluble transferrin receptor reflects tumor load in chronic lymphocytic leukemia. *Clinical Chemistry and Laboratory Medicine*, 45(10):1313–1318, 2007. doi: 10.1515/CCLM.2007.287.

E. G. Meyron-Holtz, M. C. Ghosh, and K. Iwai. Genetic ablations of iron regulatory proteins 1 and 2 reveal why iron regulatory protein 2 dominates iron homeostasis. *The EMBO Journal*, 23(2):386–395, 2004. doi: 10.1038/sj.emboj.7600041.

L. Mi, J. Yuan, and Y. Jiang. Constructed transferrin receptor-targeted liposome for the delivery of fluvoxamine to improve prognosis in a traumatic brain injury mouse model. *Drug Delivery*, 32(1):2486840, 2025. doi: 10.1080/10717544.2025.2486840.

L. D. Miller. An iron regulatory gene signature predicts outcomes in breast cancer. *Cancer Research*, 71(21):6728–6737, 2011. doi: 10.1158/0008-5472.CAN-11-1870.

H. Mizuuchi, N. Katsumata, T. Ogura, and S. Takano. Immunohistochemical study of transferrin receptor expression in normal and neoplastic cervical and endometrial tissues. *Gynecologic Oncology*, 31(2):219–229, 1988. doi: 10.1016/0090-8258(88)90029-4.

S. Mojarad-Jabali, S. Mahdinloo, M. Farshbaf, M. Sarfraz, Y. Fatahi, F. Atyabi, and H. Valizadeh. Transferrin receptor-mediated liposomal drug delivery: Recent trends in targeted therapy of cancer. *Expert Opinion on Drug Delivery*, 19(6):685–705, 2022. doi: 10.1080/17425247.2022.2083106.

T. Moos, J. M. Gudbergsson, and K. B. Johnsen. Transport of transferrin receptor-targeted antibodies through the blood–brain barrier for drug delivery to the

brain. In G. Di Rocco, editor, *Drug Delivery to the Brain*, pages 373–396. Springer, 2022. doi: 10.1007/978-3-030-88773-5_17.

I. C. Moura, Y. Lepelletier, and B. Arnulf. A neutralizing monoclonal antibody (mab a24) directed against the transferrin receptor induces apoptosis of tumor t lymphocytes from atl patients. *Blood*, 103(5):1838–1845, 2004. doi: 10.1182/blood-2003-07-2440.

M. U. Muckenthaler, S. Rivella, M. W. Hentze, and B. Galy. A red carpet for iron metabolism. *Cell*, 168(3):344–361, 2017. doi: 10.1016/j.cell.2016.12.034.

S. Muro. Challenges in design and characterization of ligand-targeted drug delivery systems. *Journal of Controlled Release*, 164(2):125–137, 2012. doi: 10.1016/j.jconrel.2012.05.052.

S. Muyldermans. Nanobodies: Natural single-domain antibodies. *Annual Review of Biochemistry*, 82:775–797, 2013. doi: 10.1146/annurev-biochem-063011-092449.

U. Nandi, I. Onyesom, and D. Douroumis. Transferrin conjugated stealth liposomes for sirolimus active targeting in breast cancer. *Journal of Drug Delivery Science and Technology*, 66:102900, 2021. doi: 10.1016/j.jddst.2021.102900.

J. Niewoehner, B. Bohrmann, and L. Collin. Increased brain penetration and potency of a therapeutic antibody using a monovalent molecular shuttle. *Neuron*, 81(1):49–60, 2014. doi: 10.1016/j.neuron.2013.10.061.

S. Oh, B. J. Kim, and N. P. Singh. Synthesis and anti-cancer activity of covalent conjugates of artemisinin and a transferrin-receptor targeting peptide. *Cancer Letters*, 274(1):33–39, 2009. doi: 10.1016/j.canlet.2008.08.031.

M. Olsman, V. Sereti, and M. Mühlenpfordt. Focused ultrasound and microbubble treatment increases delivery of transferrin receptor-targeting liposomes to the brain. *Ultrasound in Medicine & Biology*, 47(5):1343–1355, 2021. doi: 10.1016/j.ultrasmedbio.2021.01.014.

M. Osmola, B. Gierej, and K. Mleczko-Sanecka. Anemia, iron deficiency, and iron regulators in pancreatic ductal adenocarcinoma patients: A comprehensive analysis. *Current Oncology*, 30(8):7722–7739, 2023. doi: 10.3390/curroncol30080560.

W. M. Pardridge. The isolated brain microvessel: A versatile experimental model of the blood–brain barrier. *Frontiers in Physiology*, 11:398, 2020. doi: 10.3389/fphys.2020.00398.

S. Paris-Robidas, D. Brouard, V. Emond, M. Parent, and F. Calon. Internalization of targeted quantum dots by brain capillary endothelial cells in vivo. *Journal of Cerebral Blood Flow & Metabolism*, 36(4):731–742, 2016. doi: 10.1177/0271678X15608201.

A. K. Pearce and R. K. O'Reilly. Insights into active targeting of nanoparticles in drug delivery: Advances in clinical studies and design considerations for cancer nanomedicine. *Bioconjugate Chemistry*, 30(9):2300–2311, 2019. doi: 10.1021/acs.bioconjchem.9b00456.

S. Petralla, L. Saveleva, and K. M. Kanninen. Increased expression of transferrin receptor 1 in the brain cortex of 5xfad mouse model of alzheimer's disease is associated with activation of hif-1 signaling pathway. *Molecular Neurobiology*, 61 (10):6383–6394, 2024. doi: 10.1007/s12035-024-03990-3.

M. Piantino, F. Louis, and Y. Shigemoto-Mogami. Brain microvascular endothelial cells derived from human induced pluripotent stem cells as in vitro model for assessing blood-brain barrier transferrin receptor-mediated transcytosis. *Materials Today Bio*, 14:100232, 2022. doi: 10.1016/j.mtbio.2022.100232.

S. Pizzamiglio, S. Bottelli, L. Roz, L. De Cecco, E. Tagliabue, and P. Verderio. Expression of iron-related proteins differentiate non-cancerous and cancerous breast tumors. *International Journal of Molecular Sciences*, 18(2):410, 2017. doi: 10.3390/ijms18020410.

P. Ponkshe, S. Feng, and C. Tan. Inhalable liposomes for treating lung diseases: Clinical development and challenges. *Biomedical Materials*, 16(5):052002, 2021. doi: 10.1088/1748-605X/ac0c0c.

E. Pothin, D. Lesuisse, and P. Lafaye. Brain delivery of single-domain antibodies: A focus on vhh and vnar. *Pharmaceutics*, 12(10):937, 2020. doi: 10.3390/pharmaceutics12100937.

J. V. Princiotto and E. J. Zapolski. Functional heterogeneity and ph-dependent dissociation properties of human transferrin. *Biochimica et Biophysica Acta (BBA) - General Subjects*, 428(3):766–771, 1976. doi: 10.1016/0304-4165(76)90206-6.

M. Prutki, M. Poljak-Blazi, M. Jakopovic, D. Tomas, I. Stipancic, and N. Zarkovic. Altered iron metabolism, transferrin receptor 1 and ferritin in patients with colon cancer. *Cancer Letters*, 238(2):188–196, 2006. doi: 10.1016/j.canlet.2005.07.001.

A. Płoszynska, K. Ruckemann-Dziurdzinska, and A. Jozwik. Cytometric evaluation of transferrin receptor 1 (cd71) in childhood acute lymphoblastic leukemia. *Folia Histochemica et Cytobiologica*, 50(2):304–311, 2012. doi: 10.5603/fhc.2012.0040.

Z. M. Qian, H. Li, H. Sun, and K. Ho. Targeted drug delivery via the transferrin receptor-mediated endocytosis pathway. *Pharmacological Reviews*, 54(4):561–587, 2002. doi: 10.1124/pr.54.4.561.

S. Recalcati, E. Gammella, P. Buratti, and G. Cairo. Molecular regulation of cellular iron balance. *IUBMB Life*, 69(6):389–398, 2017. doi: 10.1002/iub.1628.

L. Recht, C. O. Torres, T. W. Smith, V. Raso, and T. W. Griffin. Transferrin receptor in normal and neoplastic brain tissue: Implications for brain-tumor immunotherapy. *Journal of Neurosurgery*, 72(6):941–945, 1990. doi: 10.3171/jns.1990.72.6.0941.

D. R. Richardson. Iron chelators as therapeutic agents for the treatment of cancer. *Critical Reviews in Oncology/Hematology*, 42(3):267–281, 2002. doi: 10.1016/s1040-8428(01)00218-9.

A. Robb and M. Wessling-Resnick. Regulation of transferrin receptor 2 protein levels by transferrin. *Blood*, 104(13):4294–4299, 2004. doi: 10.1182/blood-2004-06-2481.

A. M. Rosager, M. D. Sørensen, and R. H. Dahlrot. Transferrin receptor-1 and ferritin heavy and light chains in astrocytic brain tumours: Expression and prognostic value. *PLoS ONE*, 12(8):e0182954, 2017. doi: 10.1371/journal.pone.0182954.

Q. Ru, Y. Li, and L. Chen. Iron homeostasis and ferroptosis in human diseases: Mechanisms and therapeutic prospects. *Signal Transduction and Targeted Therapy*, 9(1):271, 2024. doi: 10.1038/s41392-024-01969-z.

L. Rué, C. Lopez-Lopez, and J. J. Garcia-Vallejo. Human and cynomolgus cross-reactive transferrin receptor nanobodies for blood–brain barrier delivery. *Pharmaceutics*, 15(6):1748, 2023. doi: 10.3390/pharmaceutics15061748.

Z. Rychtarcikova, S. Lettlova, and V. Tomkova. Tumour initiating cells of breast and prostate origin show alterations in the expression of genes related to iron metabolism. *Oncotarget*, 8(4):6376–6398, 2016. doi: 10.18632/oncotarget.14093.

E. Ryschich, G. Huszty, H. P. Knaebel, M. Hartel, M. W. Büchler, and J. Schmidt. Transferrin receptor is a marker of malignant phenotype in human pancreatic cancer and in neuroendocrine carcinoma of the pancreas. *European Journal of Cancer*, 40(9):1418–1422, 2004. doi: 10.1016/j.ejca.2004.01.036.

S. R'zik, Y. Beguin, and G. A. Boffa. Regulation of transferrin receptor expression in rat reticulocytes: Effects of iron overload and deficiency. *Haematologica*, 86(3): 303–311, 2001.

F. Sabir, M. Qindeel, and M. Zeeshan. Onco-receptors targeting in lung cancer via application of surface-modified and hybrid nanoparticles: A cross-disciplinary review. *Processes*, 9(4):621, 2021. doi: 10.3390/pr9040621.

I. Sakpakdeejaroen, S. Somani, and P. Laskar. Plumbagin-loaded, transferrin-conjugated liposomes for the treatment of melanoma. *Materials Science and Engineering: C*, 105:110023, 2019. doi: 10.1016/j.msec.2019.110023.

I. E. Santo, R. Campardelli, E. C. Albuquerque, S. Vieira de Melo, G. Della Porta, and E. Reverchon. Liposomes preparation using a supercritical fluid assisted continuous process. *Chemical Engineering Journal*, 249:153–159, 2014. doi: 10.1016/j.cej.2014.03.099.

P. Sapra and T. M. Allen. Ligand-targeted liposomal anticancer drugs. *Progress in Lipid Research*, 44(4):211–241, 2005. doi: 10.1016/j.plipres.2005.04.001.

J. B. Schenkman, I. Jansson, and K. M. Robie-Suh. The many roles of cytochrome b5 in hepatic microsomes. *Life Sciences*, 29(5):437–448, 1981. doi: 10.1016/0024-3205(81)90209-6.

A. M. Scott, J. D. Wolchok, and L. J. Old. Antibody therapy of cancer. *Nature Reviews Cancer*, 12(4):278–287, 2012. doi: 10.1038/nrc3236.

J. Senior. Fate and behaviour of liposomes in vivo: A review of controlling factors. *Critical Reviews in Therapeutic Drug Carrier Systems*, 3(2):123–193, 1987.

D. R. Sheff, E. A. Daro, M. Hull, and I. Mellman. The receptor recycling pathway contains two distinct populations of early endosomes with different sorting functions. *Journal of Cell Biology*, 156(5):797–808, 2002. doi: 10.1083/jcb.200110037.

Y. Shen, X. Li, D. Dong, B. Zhang, Y. Xue, and P. Shang. Transferrin receptor 1 in cancer: A new sight for cancer therapy. *American Journal of Cancer Research*, 8 (6):916–931, 2018.

S. Shimosaki, S. Nakahata, and T. Ichikawa. Development of a complete human igg monoclonal antibody to transferrin receptor 1 targeted for adult t-cell leukemia/lymphoma. *Biochemical and Biophysical Research Communications*, 485 (1):144–151, 2017. doi: 10.1016/j.bbrc.2017.02.039.

M. Singh, K. Mugler, and D. Hailoo. Differential expression of transferrin receptor (tfr) in a spectrum of normal to malignant breast tissues: Implications for in situ

and invasive carcinoma. *Applied Immunohistochemistry & Molecular Morphology*, 19(5):417–423, 2011. doi: 10.1097/PAI.0b013e318209716e.

T. Smilevska, K. Stamatopoulos, and M. Samara. Transferrin receptor-1 and 2 expression in chronic lymphocytic leukemia. *Leukemia Research*, 30(2):183–189, 2006. doi: 10.1016/j.leukres.2005.06.006.

F. Sornelli, M. Scognamiglio, V. De Leo, L. Baldino, and E. Reverchon. Supercritical assisted liposome formation for the encapsulation of hydrophobic and hydrophilic compounds. *Molecules*, 29(4):788, 2024. doi: 10.3390/molecules29040788.

M. M. Speeckaert, R. Speeckaert, and J. R. Delanghe. Biological and clinical aspects of soluble transferrin receptor. *Critical Reviews in Clinical Laboratory Sciences*, 47(5–6):213–228, 2010. doi: 10.3109/10408363.2010.550461.

S. K. Sriraman, G. Salzano, and V. P. Torchilin. Transferrin-targeted polymeric micelles for co-delivery of curcumin and doxorubicin in cervical cancer. *European Journal of Pharmaceutics and Biopharmaceutics*, 105:81–91, 2016. doi: 10.1016/j.ejpb.2016.05.021.

A. N. Steere, S. L. Byrne, N. D. Chasteen, and A. B. Mason. Kinetics of iron release from transferrin bound to the transferrin receptor at endosomal ph. *Biochimica et Biophysica Acta (BBA) - General Subjects*, 1820(3):326–333, 2012. doi: 10.1016/j.bbagen.2011.06.003.

S. Strickland, M. Jorns, L. Fourroux, L. Heyd, and D. Pappas. Cancer cell targeting via selective transferrin receptor labeling using protein-derived carbon dots. *ACS Omega*, 9(2):2707–2718, 2024. doi: 10.1021/acsomega.3c07744.

N. Sukhbaatar and T. Weichhart. Iron regulation: Macrophages in control. *Pharmaceuticals*, 11(4):137, 2018. doi: 10.3390/ph11040137.

J. Tang, Q. Wang, and Q. Yu. A stabilized retro-inverso peptide ligand of transferrin receptor for enhanced liposome-based hepatocellular carcinoma-targeted drug delivery. *Acta Biomaterialia*, 83:379–389, 2019. doi: 10.1016/j.actbio.2018.11.002.

C. Testi, A. Boffi, and L. C. Montemiglio. Structural analysis of the transferrin receptor multifaceted ligand(s) interface. *Biophysical Chemistry*, 254:106242, 2019. doi: 10.1016/j.bpc.2019.106242.

CytomX Therapeutics. Preclinical development of a probody drug conjugate (pdc) targeting cd71 for the treatment of multiple cancers [poster presentation], 2017. URL `https://cytomx.com/preclinical-development-of-a-probody-drug-conjugate-pdc-targeting-cd71-for-the-treatment-of-multiple-cancers-aacr-2016/`. CytomX Therapeutics.

S. Tian, B. Wang, and Y. Ding. The role of iron transporters and regulators in alzheimer's disease and parkinson's disease: Pathophysiological insights and therapeutic prospects. *Biomedicine & Pharmacotherapy*, 179:117419, 2024. doi: 10.1016/j.biopha.2024.117419.

S. V. Torti and F. M. Torti. Iron and cancer: More ore to be mined. *Nature Reviews Cancer*, 13(5):342–355, 2013. doi: 10.1038/nrc3495.

S. Tortorella and T. C. Karagiannis. The significance of transferrin receptors in oncology: The development of functional nano-based drug delivery systems. *Current Drug Delivery*, 11(4):427–433, 2014. doi: 10.2174/1567201810666140106115436.

P. Trucillo, R. Campardelli, and E. Reverchon. Liposomes: From bangham to supercritical fluids. *Processes*, 8(8):1022, 2020. doi: 10.3390/pr8081022.

A. Vaisman-Mentesh, M. Gutierrez-Gonzalez, B. J. DeKosky, and Y. Wine. The molecular mechanisms that underlie the immune biology of anti-drug antibody formation following treatment with monoclonal antibodies. *Frontiers in Immunology*, 11:1951, 2020. doi: 10.3389/fimmu.2020.01951.

F. M. van Bockxmeer and E. H. Morgan. Transferrin receptors during erythroid cell development. *Biochimica et Biophysica Acta (BBA) - Biomembranes*, 584(1): 464–473, 1979. doi: 10.1016/0304-4165(79)90114-7.

A. S. A. van Brussel, A. Adams, S. Oliveira, M. Vermeer, M. B. J. Wallert, M. A. Hermsen, and P. J. van Diest. Hypoxia-targeting fluorescent nanobodies for optical molecular imaging of pre-invasive breast cancer. *Molecular Imaging and Biology*, 18(4):535–544, 2016. doi: 10.1007/s11307-015-0909-6.

R. Van der Meel, S. Oliveira, and I. Altintas. Tumor-targeted nanobullets: Anti-egfr nanobody-liposomes loaded with anti-igf-1r kinase inhibitor for cancer treatment. *Journal of Controlled Release*, 159(2):281–289, 2012. doi: 10.1016/j.jconrel.2011.12.027.

I. Van Rooy, E. Mastrobattista, G. Storm, W. E. Hennink, and R. M. Schiffelers. Comparison of five different targeting ligands to enhance accumulation of liposomes into the brain. *Journal of Controlled Release*, 150(1):30–36, 2011. doi: 10.1016/j.jconrel.2010.11.014.

Sahu. Vikas, Mehata. H., and A. K. Dual-receptor-targeted nanomedicines: Emerging trends and advances in lung cancer therapeutics. *Nanomedicine*, 17(19): 1375–1395, 2022. doi: 10.2217/nnm-2021-0470.

R. Villalobos-Manzo, E. Ríos-Castro, and J. M. Hernández-Hernández. Identification of transferrin receptor 1 (tfr1) overexpressed in lung cancer cells, and internalization of magnetic au-cofe2o4 core-shell nanoparticles functionalized with its ligand in a cellular model of small cell lung cancer (sclc). *Pharmaceutics*, 14(8): 1715, 2022. doi: 10.3390/pharmaceutics14081715.

M. A. Virtanen, L. U. Viinikka, and M. K. G. Virtanen. Higher concentrations of serum transferrin receptor in children than in adults. *The American Journal of Clinical Nutrition*, 69(2):256–260, 1999. doi: 10.1093/ajcn/69.2.256.

A. C. S. Vogt, T. Arsiwala, M. Mohsen, M. Vogel, V. Manolova, and M. F. Bachmann. On iron metabolism and its regulation. *International Journal of Molecular Sciences*, 22(9):4591, 2021. doi: 10.3390/ijms22094591.

B. L. Voth, D. T. Nagasawa, and P. E. Pelargos. Transferrin receptors and glioblastoma multiforme: Current findings and potential for treatment. *Journal of Clinical Neuroscience*, 22(7):1071–1076, 2015. doi: 10.1016/j.jocn.2015.02.002.

G. Wang, A. Kumar, W. Ding, P. Korangath, T. Bera, J. Wei, P. Pai, K. Gabrielson, I. Pastan, and S. Sukumar. Intraductal administration of transferrin receptor-targeted immunotoxin clears ductal carcinoma in situ in mouse models of breast cancer—a preclinical study. *Proceedings of the National Academy of Sciences*, 119 (17):e2200200119, 2022a. doi: 10.1073/pnas.2200200119.

Y. Wang, L. F. Gu, X. Zhao, C. Hu, and Q. Chen. Tfr1 expression in induced sputum is associated with asthma severity. *PeerJ*, 10:e13474, 2022b. doi: 10.7717/peerj.13474.

F. Weber, B. Bohrmann, and J. Niewoehner. Brain shuttle antibody for efficient delivery across the blood–brain barrier. *Scientific Reports*, 8(1):578, 2018. doi: 10.1038/s41598-018-34744-7.

J. F. Whitney, J. M. Clark, T. W. Griffin, S. Gautam, and K. O. Leslie. Transferrin receptor expression in nonsmall cell lung cancer: Histopathologic and clinical correlates. *Cancer*, 76(1):20–25, 1995. doi: 10.1002/1097-0142(19950701)76:1<20::aid-cncr2820760104>3.0.co;2-5.

A. Winikajtis-Burzyńska, M. Brzosko, and H. Przepiera-Będzak. Elevated serum levels of soluble transferrin receptor are associated with an increased risk of cardiovascular, pulmonary, and hematological manifestations and a decreased risk of neuropsychiatric manifestations in systemic lupus erythematosus patients. *International Journal of Molecular Sciences*, 24(24):17340, 2023. doi: 10.3390/ijms242417340.

N. C. Winn, K. M. Volk, and A. H. Hasty. Regulation of tissue iron homeostasis: The macrophage "ferrostat". *JCI Insight*, 5(4):e132964, 2020. doi: 10.1172/jci.insight.132964.

Y. Wouters, T. Jaspers, B. De Strooper, and M. Dewilde. Identification and in vivo characterization of a brain-penetrating nanobody. *Fluids and Barriers of the CNS*, 17(1):62, 2020. doi: 10.1186/s12987-020-00226-z.

Y. Wouters, T. Jaspers, L. Rué, L. Serneels, B. De Strooper, and M. Dewilde. Vhhs as tools for therapeutic protein delivery to the central nervous system. *Fluids and Barriers of the CNS*, 19(1):79, 2022. doi: 10.1186/s12987-022-00374-4.

J. Y. Wu, M. J. Borowitz, and E. G. Weir. The usefulness of cd71 expression by flow cytometry for differentiating indolent from aggressive cd10+ b-cell lymphomas. *American Journal of Clinical Pathology*, 126(1):39–46, 2006. doi: 10.1309/X8LB-RRBB-C43P-L9HC.

Y. Wu, J. Xu, and J. Chen. Blocking transferrin receptor inhibits the growth of lung adenocarcinoma cells in vitro. *Thoracic Cancer*, 9(2):253–261, 2018. doi: 10.1111/1759-7714.12569.

Y. L. Wu, R. A. Soo, G. Locatelli, and R. Rosell. Does c-met remain a rational target for therapy in patients with egfr tki-resistant non-small cell lung cancer? *Cancer Treatment Reviews*, 61:70–81, 2017. doi: 10.1016/j.ctrv.2017.10.003.

S. Wöll. Biophysical characterization of nanobody-functionalized liposomes. *European Journal of Pharmaceutics and Biopharmaceutics*, 137:98–107, 2019. doi: 10.1016/j.ejpb.2019.02.012.

B. Xiang and D. Y. Cao. Preparation of drug liposomes by thin-film hydration and homogenization. In W. L. Lu & X. R. Qi, editor, *Liposome-Based Drug Delivery Systems*, pages 17–33. Springer Berlin Heidelberg, 2021. doi: 10.1007/978-3-662-49320-5_2.

S. Yan, J. Na, X. Liu, and P. Wu. Different targeting ligands-mediated drug delivery systems for tumor therapy. *Pharmaceutics*, 16(2):248, 2024. doi: 10.3390/pharmaceutics16020248.

W. Yan, S. S. Y. Leung, and K. K. W. To. Updates on the use of liposomes for active tumor targeting in cancer therapy. *Nanomedicine*, 15(3):303–318, 2020. doi: 10.2217/nnm-2019-0308.

C. Yang, J. Li, and Y. Guo. Role of tfrc as a novel prognostic biomarker and in immunotherapy for pancreatic carcinoma. *Frontiers in Molecular Biosciences*, 9:756895, 2022. doi: 10.3389/fmolb.2022.756895.

D. C. Yang, F. Wang, R. X. Guan, Z. B. Jin, and Y. Zhou. Expression of transferrin receptor and ferritin in human brain tumors. *Chinese Journal of Oncology*, 23(4): 312–314, 2001.

Y. Yang, Z. Liu, and Y. Zhou. Erianin-loaded transferrin-modified liposomes for hepatocellular carcinoma treatment. *Journal of Liposome Research*, 31(4):365–374, 2021. doi: 10.1080/08982104.2020.1835948.

M. Yokoyama. Drug targeting with nano-sized carrier systems. *Journal of Artificial Organs*, 8(2):77–84, 2005. doi: 10.1007/s10047-005-0288-0.

J. Yoo, C. Park, G. Yi, D. Lee, and H. Koo. Active targeting strategies using biological ligands for nanoparticle drug delivery systems. *Cancers*, 11(5):640, 2019. doi: 10.3390/cancers11050640.

B. Yu, R. J. Lee, and L. J. Lee. Microfluidic methods for production of liposomes. *Methods in Enzymology*, 465:129–141, 2009. doi: 10.1016/S0076-6879(09)65007-2.

Y. J. Yu, Y. Zhang, and M. Kenrick. Boosting brain uptake of a therapeutic antibody by reducing its affinity for the transferrin receptor. *Science Translational Medicine*, 3(84):84ra44, 2011. doi: 10.1126/scitranslmed.3002230.

Y. J. Yu, J. K. Atwal, and Y. Zhang. Therapeutic bispecific antibodies cross the blood–brain barrier in nonhuman primates. *Science Translational Medicine*, 5 (187):187ra72, 2013. doi: 10.1126/scitranslmed.3005685.

E. Yuba. Development of functional liposomes by modification of stimuli-responsive materials and their biomedical applications. *Journal of Materials Chemistry B*, 8 (6):1093–1107, 2020. doi: 10.1039/c9tb02470k.

M. M. Zakin, B. Baron, and F. Guillou. Regulation of the tissue-specific expression of transferrin gene. *Biochimica et Biophysica Acta (BBA) - Gene Structure and Expression*, 1132(2):147–154, 1992. doi: 10.1016/0167-4781(92)90022-L.

L. Zapala, K. Kluzek, M. Foksinski, and R. Olinski. Increased iron uptake and altered expression of iron-related genes in prostate cancer. *International Journal of Molecular Sciences*, 22(23):12983, 2021. doi: 10.3390/ijms222312983.

X. Zeng, Y. Sun, and H. Xiao. Glioma cell membrane and transferrin dual-functionalized liposomes for targeted delivery of elemene and cabazitaxel. *Journal of Nanobiotechnology*, 19(1):378, 2021. doi: 10.1186/s12951-021-01124-x.

D. Zhang, J. Duque-Jimenez, and F. Facchinetti. Transferrin receptor targeting chimeras for membrane protein degradation. *Nature*, 638(8051):787–795, 2025. doi: 10.1038/s41586-024-07947-3.

L. Zhang, F. X. Gu, and J. M. Chan. Nanoparticles in medicine: Therapeutic applications and developments. *Clinical Pharmacology & Therapeutics*, 83(5): 761–769, 2008. doi: 10.1038/sj.clpt.6100400.

Y. Zhang, Y. Xue, and Y. Jia. Associations between serum soluble transferrin receptor and the prevalence of cancers: Evidence from nhanes 2015-2018. *Frontiers in Oncology*, 12:1039930, 2022. doi: 10.3389/fonc.2022.1039930.

X. Zhao and D. R. Richardson. The role of the ndrg1 in the pathogenesis and treatment of breast cancer. *Biochimica et Biophysica Acta (BBA) - Reviews on Cancer*, 1878(6):188871, 2023. doi: 10.1016/j.bbcan.2023.188871.

X. Zhao, J. He, and Y. Chen. Transferrin receptor-targeted aptamer–drug conjugate overcomes blood–brain barrier for potent glioblastoma therapy. *Bioconjugate Chemistry*, 36(5):102749, 2025. doi: 10.1021/acs.bioconjchem.5c00137.

Y. Z. Zhao, Q. Lin, and H. L. Wong. Brain-targeted delivery of transferrin-conjugated lipid nanoparticles loaded with curcumin for alzheimer's therapy. *Journal of Controlled Release*, 152(1):143–150, 2011. doi: 10.1016/j.jconrel.2011.02.016.

S. Zhu, C. Liu, and C. Zhao. Increased serum soluble transferrin receptor levels were associated with high prevalence of cardiovascular diseases: Insights from nhanes 2017–2018. *Frontiers in Cell and Developmental Biology*, 10:874846, 2022. doi: 10.3389/fcell.2022.874846.

T. Zong, L. Mei, and H. Gao. Synergistic dual-ligand doxorubicin liposomes improve targeting and therapeutic efficacy of brain glioma in animals. *Molecular Pharmaceutics*, 11(7):2346–2357, 2014. doi: 10.1021/mp500057n.



Dipartimento di Farmacia
Via Giovanni Paolo II, 132, 84084 Fisciano, Salerno